MULTIPLICATIVE CONTRAST SOURCE INVERSION METHOD IN ELECTRICAL PROPERTIES TOMOGRAPHY BASED ON JACOBI MATRIX INVERSION

Florens Jan HELFFERICH

MULTIPLICATIVE CONTRAST SOURCE INVERSION METHOD IN ELECTRICAL PROPERTIES TOMOGRAPHY BASED ON JACOBI MATRIX INVERSION

MSc Thesis

by

Florens Jan HELFFERICH

to obtain the degree of Master of Science
at the Delft University of Technology,
to be defended publicly on
Friday April 5th, 2024 at 14:30

Student Number: 4607155
Thesis Committee: Dr. Ir. Rob F. Remis, Delft University of Technology
Dr. Ir. Bert-Jan Kooij, Delft University of Technology

An electronic version of this MSc thesis is available at
http://repository.tudelft.nl/.

ABSTRACT

The tissue electrical properties of conductivity and permittivity affect the interactions of electromagnetic fields in the body. These properties vary throughout the different tissues as the tissue structure and composition varies. In this thesis, medical imaging and diagnosis is used as primary example to motivate exploration of a novel regularization application to MRI-based electrical properties tomography (EPT) method.

Total variation (TV) regularization has been shown to perform noise reduction in the iterative Contrast Source Inversion EPT (CSI-EPT) method. An alternative Jacobi iteration regularization to the known conjugate gradient formulation is elaborated and applied to an E-polarized MRI fields scenario such that this thesis presents the Jacobi step regularized CSI-EPT.

The alternative regularization method outperforms the known regularization method in the reconstruction qualities of noise-suppression and edge-preservation in the simulated MRI experiments using a virtual body model. Further advancements are also described, such as multiple inner-iterations Jacobi regularization and an anatomical prior initialization of the contrast function. Important future research topics are the incorporation and evaluation of the Jacobi step regularization into more advanced CSI-EPT versions, which are the three-dimensional and transceive phase based algorithms to correct realistic MRI data.

SAMENVATTING

De elektrische eigenschappen geleiding en permittiviteit van weefsel bepalen de interacties van elektromagnetische velden in het lichaam. Deze eigenschappen variëren per weefsel door de verschillende structuren en stoffen van het weefsel en zijn de focus van de elektrische eigenschappen tomografie (EPT) technieken. In de thesis wordt medische beeldvorming en diagnose aangehaald als primair voorbeeld voor het onderzoeken en toepassen van een nieuwe regularisatie methode op EPT in de context van de tweedimensionale E-gepolariseerde MRI velden.

Totale variatie (TV) regularisatie is een bekende methode voor onderdrukking van ruis in de EPT-reconstructies van het iteratieve algoritme contrast bronnen inversie EPT (CSI-EPT). De Jacobi iteratie regularisatie voor CSI-EPT is toegepast en vergeleken als alternatief voor de reeds bekende gradiëntdaling regularisatie methode.

De resulterende Jacobi stap CSI-EPT methode heeft betere ruisonderdrukking en behoud van overgangen in de reconstructies van de virtuele MRI-experimenten vergeleken met de gradiëntdaling methode. Andere contributies zijn ook beschreven in de thesis, zoals meerdere Jacobi iteraties per CSI-EPT stap en een contrast functie initialisatie op basis van voorkennis van de anatomische structuren. Belangrijke onderzoek vooruitzichten zijn het uitwerken van de driedimensionale Jacobi stap regularisatie en toepassing van de regularisatie in EPT-algoritmes die de zendontvanger fase van realistische MRI-data corrigeert.

PREFACE

Early in 2023 I had been presented with a choice for an extra project and potential MSc thesis subject. I chose to study MR-EPT and experiment with CSI-EPT myself under supervision of Rob to learn about a new technology instead of going into depth about a technology that I was already familiar with. After a few months studying the CSI-EPT method I was ready to be introduced to the alternative TV formulation of Peter van den Berg and start documenting my own findings.

Reading about the various MR-EPT methods and the specific Contrast Source Inversion EPT techniques has opened my eyes further to the challenges in biomedical engineering. The physics and engineering of (medical) imaging will always feel positively magical to me, no matter the level of understanding that I achieve. For those experiences I would like to thank Rob Remis for giving me the opportunity to study the subject and for the pleasant way that he has supervised my work and this thesis. It was always motivating to meet with you and I had a great time collaborating and learning from you during the creation of the journal paper.

Furthermore, I would like to thank Peter Stijnman and Reijer Leijsen for their swift communication about the TPC method and about CSI-EPT in general.

Thank you Bert-Jan Kooij for being a part of my MSc Thesis committee.

A great thank you to all my study mates and friends; and in particular thank you for the long "experience" days and evenings with Marien and Sheng. Additional thanks to Dehlia and my brother Kristiaan for the inspiring words and working ethic at the occasional study sessions. Finally, thank you to my house mates, friends and mom and dad for all the fun times and support throughout the making of this thesis.

Florens Jan Helfferich
Delft, March 26, 2024

CONTENTS

1

INTRODUCTION

Despite stable or increasing incidence in cancer rates in America and Europe, the mortality rate in both regions of the world is in decline by 33% from 1990 to 2023 [1] and an estimated decline of "6.5% among men and 4.3% among women in the EU total cancer mortality rates between 2018 and 2024" [2]. The studies, respectively, note 3.8 million averted deaths in the United States since 1990 and predict 6.2 million averted deaths in Europe for a similar period. Siegel et al. [1] thus highlights that the progress of advances in treatment are increasingly reflected by these declining cancer mortality rates[1], while [3] notes 5-year survival rates are suggested to increase due to better treatment and earlier detection of cancers.

Supporting that continued decline is the ongoing research in accurate diagnosis and prognosis of patients tumors. Treatment regarding benign and cancerous tumors is different, whereas benign tumors mostly require more monitoring than medical intervention, cancer treatment involves a multitude of medical interventions such as prolonged monitoring, surgery, chemotherapy and more. Hence it is pertinent to differentiate between these types of tumorous tissue.

Simultaneously, advancements in the medical imaging field provide ways to guide such therapies or create new therapies also due to an advent in quantifiable biomarkers. In this thesis, medical imaging and diagnosis of the malignancy of tumours is used as primary example to motivate exploration of novel regularization for a specific MRI-based electrical properties tomography (EPT) method. The electrical properties (EP) of conductivity and relative permittivity are material properties that affect the behaviour of electromagnetic (EM) fields. These properties vary throughout the different biological tissue types and are mostly determined by tissue structure and composition[4], [5]. Differentiation of benign and cancerous tumors is shown in literature [6]–[10]. Hence EP-based diagnostics, and by proxy the EPT methods, are thus seen as potent in enhancing diagnosis accuracy.

Other applications of the EP profiles obtained from EPT include radiofrequency hyperthermia and the Specific Absorption Rate (SAR) determination; electroencephalogram (EEG) and cardiac related applications (electrocardiogram and pacemakers); tissue

[1] Absolute mortality rates have risen in this period, however, the age standardized mortality rates (ASR) has declined, which are the percentages cited here. ASR percentages take into account population growth and aging effects.

healing with EM pulses, impedance pneumography and plethysmography [11], [12].

There are multiple ways to measure the EP values, however, this report is on a specific EP reconstruction method using magnetic resonance imaging (MRI): magnetic resonance electrical properties tomography (MR-EPT). Using an MRI system is beneficial compared to other measurement and reconstruction methods for multiple reasons. Besides the good signal reception from soft tissues, MR-EPT does not require mounting of electrodes onto the body like Electric impedance tomography (EIT) or its magnetic resonance variant MR-EIT[13]. Furthermore, MR-EPT requires only the control of the (radiofrequent) EM field and no additional acoustic or electrical modes compared to other EPT techniques[13].

Within MR-EPT a distinction can be made between two approaches to reconstruction of the electrical properties profile. The differential methods generally apply Helmholtz equations to directly and quickly perform the reconstruction from the magnetic field data of MRI at a local region of interest. However, these methods are noise prone and are therefore outperformed by integral methods that are more robust against noise influences [13]. The integral methods take into account EM fields from throughout the region of interest in order to find the EP values that can support those fields in an iterative manner. Both the global and the iterative aspects of integral methods make them computationally expensive compared to the differential methods.

Additionally, the problem of noise is ever-pervasive, even for integral methods, which is when regularization is introduced. By utilizing the prior knowledge that EPs are invariant throughout one tissue type the final reconstruction is constrained by the regularization factor into a reconstruction that resembles such anatomical structure. Total variation (TV) regularization has been shown to perform noise reduction in the specific Contrast Source Inversion EPT (CSI-EPT) method [14]. An alternative TV regularization to that known formulation is described in [15] and this thesis proposes the novel Jacobi step regularization in the application of CSI-EPT along the lines of that description.

1.1. RESEARCH QUESTION

The application of CSI for MR-EPT can differ depending on the assumed available MRI field data resulting in different possible CSI implementations. In order to formulate the research objective while defining the scope of this thesis project the following research question is posed:

What are the characteristics in terms of performance and options of the Jacobi step multiplicative regularization for CSI-EPT and the more advanced transceive phase CSI-EPT?

The following sub-questions are defined to help answer the research question:

- SQ1: What is the alternative formulation of multiplicative TV regularization and how is it implementable in CSI-EPT?
- SQ2: What is the reconstruction performance of the described implementation for CSI-EPT?

- SQ3: What are the options to process transceive phase field data in multiplicative regularized CSI-EPT?

1.2. CONTRIBUTIONS

Upon completion of the thesis project the following contributions have been made, for which the numbering corresponds to the research sub-questions.

- C1: The Jacobi matrix inversion method is a low complexity partial differential equation solution to the alternative regularization formulation for CSI-EPT.
- C2a: The resulting Jacobi-step CSI-EPT outperforms the known Conjugate Gradient based multiplicative regularization.
- C2b: Multiple iterations Jacobi step CSI-EPT was explored, yet did not significantly improve reconstruction quality.
- C2c: A new type of contrast initialization was devised and compatibility with this initialization method for the Jacobi step CSI-EPT was shown.
- C3: Analysis of the transceive phase CSI-EPT cost function shows increased potential of encountering local minima.

Additionally, the contributions C1 and C2a have been summarized and communicated to the scientific community in the article titled "*Improved Multiplicative Regularization for CSI-EPT*" published in the IEEE Journal of Electromagnetics, RF and Microwaves in Medicine and Biology. A copy of this article is attached in Appendix C.

1.3. OUTLINE OF THE THESIS

The outline of the thesis is as follows. Chapter 2 provides background information on the EM field quantities in MRI and the basic contrast source inversion EPT method as the focus of this thesis. Chapter 3 elaborates in a broad and theoretical sense the various considerations involved in modeling and performing CSI-EPT and discusses in detail the alternative Total Variation regularization. The chosen approaches and implementation of EM field simulation and reconstruction algorithms are presented in Chapter 4 which were used to create the numerical simulation results that are presented in Chapter 5. Finally, a summary and discussion of the thesis are provided in the concluding Chapter 6.

2

BACKGROUND

2.1. MAGNETIC RESONANCE EPT

This section serves to explain the interactions of Magnetic Resonance Imaging (MRI) and the electromagnetic (EM) fields that arise from the presence of material such as typically a patient body in the MRI scanner. This includes summarizing the electromagnetic fields in an MRI system and explaining how knowledge of the fields enables retrieval of the electrical properties (EP) quantitatively.

The Maxwell's equations describe the interactions of magnetic and electric fields in the presence of material in a position $\mathbf{r} \in D$, where D denotes the domain of the body inside the MRI. These equations are given by:

$$\begin{aligned} -\nabla \times \hat{\mathbf{H}}(\mathbf{r}) + \eta(\mathbf{r})\hat{\mathbf{E}}(\mathbf{r}) &= -\hat{\mathbf{J}}^{ext}(\mathbf{r}) \\ \nabla \times \hat{\mathbf{E}}(\mathbf{r}) + j\omega\mu(\mathbf{r})\hat{\mathbf{H}}(\mathbf{r}) &= \mathbf{0} \end{aligned} \tag{2.1}$$

where the circumflex denotes time-harmonic fields for the magnetic field strength $\hat{\mathbf{H}}$, the electric field $\hat{\mathbf{E}}$ and the external current density $\hat{\mathbf{J}}^{ext}$; and wherein η, ω and μ are the per-unit-length admittance, angular frequency and magnetic permeability, respectively. Finally the letter j is used to denote the imaginary unit. The admittance contains the EP terms of conductivity σ and permittivity ε which are of interest to EPT as:

$$\eta(\mathbf{r}) = \sigma(\mathbf{r}) + j\omega\varepsilon(\mathbf{r}) \tag{2.2}$$

Note that pixel or voxel intensities of an MRI image are the consequence of magnetic field quantities inside the scanner and therefore allows retrieval of the admittance and EP values with knowledge of the other quantities in the Maxwell's equations. The upcoming sections describe the magnetic fields inside the MRI scanner (Section 2.1.1) and the three types of mathematical formulations forming the starting point to retrieving the EPs from these magnetic field quantities (Section 2.1.2).

2.1.1. MEASURED QUANTITIES FROM MRI

Before discussing the EPT formulations, an explanation of the field quantities measured in MRI is given. At the end, emphasis is placed on a practical complex scalar description for the relevant transmit and receive fields.

The MRI data involves the bulk transverse magnetization (magnitude) in an object and is measured as the induced voltage on a coil in response to the changing magnetic flux through its surface. This transverse magnetization is the result of a radio-frequent magnetic field, i.e. the RF excitation pulse, acting on the existing longitudinal magnetization due to the main magnetic field referred to as the $\mathbf{B}_0$ field. In order to change the orientation of the magnetization from longitudinal to transversal the RF excitation field $\mathbf{B}_1$ is applied with the Larmor frequency ω which corresponds to the angular frequency of hydrogen atoms in precession around the axis of the external field $\mathbf{B}_0$ ($\approx$ 128MHz for 3T main magnetic field strength).

It is common to refer to two different RF fields during an MRI readout procedure. The first is the transmit field or excitation field, which is responsible for changing the bulk magnetization direction from the longitudinal axis into the transverse plane, and the second is the receive field that is seen as the source of the retrieved MRI data. The following paragraphs connect these field concepts to the measurable MRI quantities relevant to MR-EPT.

Assuming the main magnetic field is directed in the negative longitudinal direction, i.e. $\mathbf{B}_0 = -B_0\mathbf{i}_z$ with $B_0 > 0$, then the total transverse RF field at location $\mathbf{r}$ in the MRI bore and at time t can be represented as a sum of vectors

$$\mathbf{B}_1(\mathbf{r},t) = \mathbf{B}_1^+(\mathbf{r},t) + \mathbf{B}_1^-(\mathbf{r},t) \tag{2.3}$$

where the $\mathbf{B}_1^+$ and $\mathbf{B}_1^-$ vectors now represent the transmit and receive fields respectively. To elaborate on this further, the total transverse field is decomposed in its x- and y-axis components, also referred to as the laboratory frame:

$$\mathbf{B}_1(\mathbf{r},t) = B_{1x}(\mathbf{r},t)\mathbf{i}_x + B_{1y}(\mathbf{r},t)\mathbf{i}_y \tag{2.4}$$

The representation of these x- and y-components is time periodic with the Larmor frequency due to the proportional to the transmission current $I\cos(\omega t)$ in the MRI coils and an amplitude A. Furthermore, attenuation occurs by position and frequency dependent factors (C_x, C_y) as well as a phase-shift by position and frequency dependent factors pertaining to conduction and displacement currents (α, β) [16].

$$\begin{aligned} B_{1x} &= C_x I A\cos(\omega t + \phi + \alpha) \\ B_{1y} &= C_y I A\cos(\omega t + \phi + \beta) \end{aligned} \tag{2.5}$$

In order to arrive at relevant magnetic field quantities, phasor notation and the Argand complex representation of the transverse plane are applied. The phasor notation is employed as

$$B(\mathbf{r},t) = \mathrm{Re}\left[\hat{B}(\mathbf{r},j\omega)\exp(j\omega t)\right], \tag{2.6}$$

with j denoting the imaginary unit and for brevity the dependence of the complex phasor coefficient on location and frequency is further omitted yet implied by the circumflex denotation, unless otherwise stated. The derivation starts by rewriting the cosines as complex exponentials and aggregating terms into the complex phasor coefficients $\hat{B}_{1x}$

and $\hat{B}_{1y}$:

$$\begin{aligned} B_{1x} &= C_x I A \left[\exp(j(\omega t+\phi+\alpha)) + \exp(j(-\omega t-\phi-\alpha))\right]/2 \\ &= \left[\hat{B}_{1x}\exp(j\omega t) + \hat{B}^*_{1x}\exp(-j\omega t)\right]/2 \\ B_{1y} &= C_y I A \left[\exp(j(\omega t+\phi+\alpha)) + \exp(j(-\omega t-\phi-\alpha))\right]/2 \\ &= \left[\hat{B}_{1y}\exp(j\omega t) + \hat{B}^*_{1y}\exp(-j\omega t)\right]/2 \end{aligned} \tag{2.7}$$

wherein the asterisk denotes complex conjugation. Note the complex conjugation is merely a result of the introduction of the complex exponentials.

Next, the transverse plane is expressed using the Argand representation wherein the real component of a complex quantity describes vector components along the x-axis, while the imaginary component describes vector components along the y-axis. The resulting complex Argand quantity is denoted with caligraphic letters. This is applied to equation 2.4 and in the subsequent line the result from equation 2.7 is applied.

$$\begin{aligned} \mathscr{B}_1(\mathbf{r},t) &= B_{1x}(\mathbf{r},t) + jB_{1y}(\mathbf{r},t) \\ &= \frac{\left[\hat{B}_{1x}+j\hat{B}_{1y}\right]}{2}\exp(j\omega t) + \frac{\left[\hat{B}^*_{1x}+j\hat{B}^*_{1y}\right]}{2}\exp(-j\omega t) \end{aligned} \tag{2.8}$$

Observe the separation of the positive and negative time convention exponentials. The first term on the right hand side expresses a complex function $(a+jb)\exp(j\omega t)$ where an a quantity exists on the rotating x-axis $\tilde{\mathbf{i}}^+_x$ and a b quantity on the rotating y-axis $\tilde{\mathbf{i}}^+_y$ [16], which is leading the rotating x-axis by $\frac{\pi}{2}$ radians. The latter is also observed in the equation above where $j\exp(j(\omega t) = \exp(j(\omega t+\frac{\pi}{2}))$. Hence, this first term in equation 2.8 describes the positively rotating magnetic field $\tilde{\mathscr{B}}^+_1$ (the tilde denoting the use of a rotating frame of reference) in terms of the laboratory frame phasor coefficients $\frac{\hat{B}_{1x}}{2}$ and $\frac{\hat{B}_{1y}}{2}$ analogous to the $a+jb$ quantity. A similar analysis for the field in the negatively rotating frame of reference can be made and describes $\tilde{\mathscr{B}}^-_1$.

$$\tilde{\mathscr{B}}^+_1(\mathbf{r},j\omega) = \frac{\left[\hat{B}_{1x}+j\hat{B}_{1y}\right]}{2} \quad \text{and} \quad \tilde{\mathscr{B}}^-_1(\mathbf{r},j\omega) = \frac{\left[\hat{B}_{1x}-j\hat{B}_{1y}\right]^*}{2} \tag{2.9}$$

Now the transition back from complex transverse plane to the vector representation is made using the positively rotating x- and y-axis unit vectors $\tilde{\mathbf{i}}^+_x$ and $\tilde{\mathbf{i}}^+_y$.

$$\tilde{\mathbf{B}}^+_1 = \mathrm{Re}(\tilde{\mathscr{B}}^+_1)\tilde{\mathbf{i}}^+_x + \mathrm{Im}(\tilde{\mathscr{B}}^+_1)\tilde{\mathbf{i}}^+_y \tag{2.10}$$

And finally, by projecting the positively rotating frame onto the laboratory frame and remembering the orientation of the longitudinal field as pointing into the negative z-axis, a left handed polarized field is retrieved while a right-handed polarized field is retrieved from the negatively rotating field:

$$\begin{aligned} \mathbf{B}^+_1(\mathbf{r},t) &= \mathrm{Re}(\tilde{\mathscr{B}}^+_1)\left[\cos(\omega t)\mathbf{i}_x + \sin(\omega t)\mathbf{i}_y\right] + \mathrm{Im}(\tilde{\mathscr{B}}^+_1)\left[-\sin(\omega t)\mathbf{i}_x + \cos(\omega t)\mathbf{i}_y\right] \\ \mathbf{B}^-_1(\mathbf{r},t) &= \mathrm{Re}(\tilde{\mathscr{B}}^-_1)\left[\cos(\omega t)\mathbf{i}_x - \sin(\omega t)\mathbf{i}_y\right] + \mathrm{Im}(\tilde{\mathscr{B}}^-_1)\left[\sin(\omega t)\mathbf{i}_x + \cos(\omega t)\mathbf{i}_y\right] \end{aligned} \tag{2.11}$$

The steps of excitation and decomposition of the rotating magnetization are summarized in Figure 2.1.

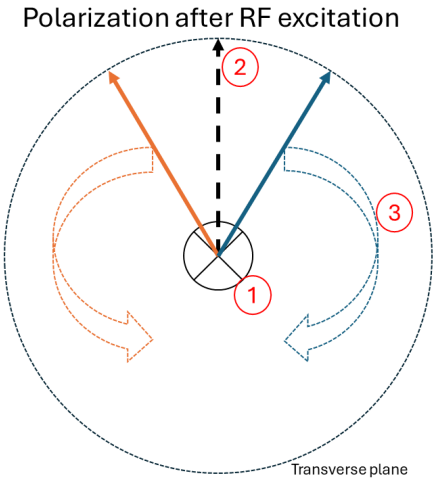

Figure 2.1: Excitation and the LH and RH polarized fields. 1) The initial bulk magnetization directed in the negative longitudinal axis (into the paper), 2) RF excitation puts the magnetization in the transverse plane and 3) the resulting rotating magnetic fields can be decomposed in left-handed (orange) and right-handed (blue) polarized fields.

This polarization terminology is commonly used to refer to the left-handed field $\mathbf{B}_1^+$ as the transmit field and the right-handed field $\mathbf{B}_1^-$ as the receive field. To finalize the connection with actual MRI imaging, it is noted that the transmit and receive field distinction is used to express the receive coil induced voltage signal from a voxel at position $\mathbf{r}$. The following signal model corresponds to small flip angle conditions, yet this is merely for simplification [16], [17]:

$$V(\mathbf{r}) \approx -2j\omega C(\mathbf{r})\gamma\tau M_0 \tilde{\mathcal{B}}_1^+ \tilde{\mathcal{B}}_1^{-*} \tag{2.12}$$

with C containing attenuation factors in the tissue like the proton density ϱ but also relaxation effects [17], γ the gyromagnetic ratio, τ the RF excitation pulse duration and the amplitude and phase terms come from the polar form of the transmit field as $\tilde{\mathcal{B}}_1^+ = \left|\tilde{\mathcal{B}}_1^+\right| \exp\left(j\phi^+\right)$. The receive field is additionally weighted by the proton density, yet this is tractable from transmit and receive field symmetry, object symmetry and imaging setup [13].

Note the recurrence of the complex coefficients from equations 2.9 for which is emphasized that they are complex valued descriptions of the transmit and receive fields, i.e. $\hat{B}_1^+$ and $\hat{B}_1^-$ respectively. To make this explicit the positively and negatively rotating vectors are introduced [13]

$$\mathbf{i}^+ = \tfrac{1}{2}(\mathbf{i}_x + j\mathbf{i}_y) \qquad \text{and} \qquad \mathbf{i}^- = \tfrac{1}{2}(\mathbf{i}_x - j\mathbf{i}_y) \tag{2.13}$$

and subsequently used on the vector containing the complex x- and y-axis phasor coefficients of the total RF field, i.e. $\hat{\mathbf{B}}_1 = \hat{B}_{1x}\mathbf{i}_x + \hat{B}_{1y}\mathbf{i}_y$. For future reference the same LH and RH field expressions from equations 2.9 are thus retrieved as:

$$\hat{B}_1^+ = \mathbf{i}^+ \cdot \hat{\mathbf{B}}_1 = \frac{\hat{B}_{1x} + j\hat{B}_{1y}}{2} \quad \text{and} \quad \hat{B}_1^{-*} = \mathbf{i}^- \cdot \hat{\mathbf{B}}_1 = \frac{\hat{B}_{1x} - j\hat{B}_{1y}}{2} \tag{2.14}$$

2.1.2. MR-EPT FUNDAMENTALS

There exist three MR-EPT fundamental mathematical formulations as described by Leijsen et al. [13], that form the starting point(s) for EP reconstruction methods. In this section the biophysical origins of the EP values are briefly introduced. Thereafter the Maxwell's equations as seen in equations 2.1 are reformulated to describe the EPs in terms of the primary measurement data for MR-EPT: the transmit field $\hat{B}_1^+$.

BIOPHYSICAL TISSUE PROPERTIES IN MRI

Before discussing the physical quantities, it is worth noting the biophysical origins of the electrical properties of tissue. MRI systems operate at a limited frequency range (approximately $10^7 - 10^8 Hz$) and this range also characterizes the retrieved EP values from MR-EPT, due to the frequency dependency of EP of various biological tissues. Depending on the specific tissue, conductivity is increased by about one order of magnitude compared to low frequency EM influences [5] and corresponds with the "ionic conductivities commensurate with the nature and extent of their ionic content and ionic mobility" as mentioned by [4]. However, relative permittivity shows a decreasing trend with increasing frequency [4], [5]. The MRI frequency range is in the "β dispersion" ($\sim 10^8 Hz$), where relative permittivity is caused mainly by polarization of cellular membranes [4].

There are techniques to quantify the magnetic permeability μ using MRI as well, these are called Quantitative Susceptibility Mapping (QSM) techniques [18] via $\mu_r \mu_0 = (1 + \chi_{sus}(\mathbf{r}))\mu_0$ with χ_{sus} the bulk magnetic susceptibility in a sample at position $\mathbf{r}$. However the presented fundamental equations assume the local susceptibility is negligible thus $\mu = \mu_0$.

MAXWELL'S EQUATIONS FOR MR-EPT

Using the Maxwell's equations (see eq. 2.1) expressions for the complex valued transmit field ($\hat{B}_1^+$) can be found in terms of known EM fields. Such derivation starts with setting the current density term $\hat{\mathbf{j}}^{ext}$ to zero because only outside the object is a current source present, which produces the EM fields necessary for MRI. Furthermore, the constitutive relation $\hat{\mathbf{B}}_1 = \mu_0 \hat{\mathbf{H}}$ is used to find a modified Maxwell's equations inside the object:

$$\begin{aligned} -\nabla \times \hat{\mathbf{B}}_1(\mathbf{r}) + \mu_0 \eta(\mathbf{r}) \hat{\mathbf{E}}(\mathbf{r}) &= \mathbf{0} \quad \mathbf{r} \in D \\ \nabla \times \hat{\mathbf{E}}(\mathbf{r}) + j\omega \hat{\mathbf{B}}_1(\mathbf{r}) &= \mathbf{0}. \end{aligned} \tag{2.15}$$

These expressions form the basis of many MR-EPT methods. Detailed derivations of the three different formulations, in differential and integral form, are presented in the extensive EPT review by Leijsen et al. [13]. Section 2.2.1 presents the integral formulation of the EM fields that is paramount to the basics of CSI-EPT. A small review of differential EPT methods is given next.

DIFFERENTIAL EPT

MR-EPT approaches that fall in the differential category make use of the first and second-order differential formulations for the transmit field. To arrive at these equations the

Maxwell's equations are rewritten as such for the first-order differential Maxwell's equations

$$\hat{B}_1^+ = \frac{1}{\omega}(\partial^+ \hat{E}_z - \partial_z \hat{E}_1^+) \quad \text{and} \quad \hat{B}_1^- = -\frac{1}{\omega}(\partial^- \hat{E}_z - \partial_z \hat{E}_1^-), \tag{2.16}$$

and for the second-order differential Helmholtz' equations

$$\nabla^2 \hat{B}_1^+ + \mathbf{i}^+ \cdot \left[\frac{\nabla \eta}{\eta} \times (\nabla \times \hat{\mathbf{B}}_1) \right] + k^2 \hat{B}_1^+ = 0. \tag{2.17}$$

The latter formulation takes into account the inhomogeneity of the object as seen in the middle gradient term. For simplicity this term can be omitted, essentially assuming homogeneity of the imaged object.

The differential formulations are sensitive to noise in the MR image and thus suffer from low signal-to-noise ratio (SNR) imaging [13], [19]. A good exemplary differential approach is the Helmholtz-based EPT (H-EPT) for its simplicity and polar opposite nature compared to CSI-EPT. Helmholtz-based EPT assumes homogeneity of the object admittance structure and so simply expresses equation 2.17 as

$$\frac{\nabla^2 \hat{B}_1^+(\mathbf{r})}{\hat{B}_1^+(\mathbf{r})} = -k^2(\mathbf{r}). \tag{2.18}$$

Using the connection between the wave number k and admittance at position $\mathbf{r}$, the electric properties are retrieved using

$$\sigma(\mathbf{r}) = \frac{1}{\omega\mu_0} \mathrm{Im}\left[\frac{\nabla^2 \hat{B}_1^+}{\hat{B}_1^+} \right] \quad \text{and} \quad \varepsilon(\mathbf{r}) = -\frac{1}{\omega^2\mu_0} \mathrm{Re}\left[\frac{\nabla^2 \hat{B}_1^+}{\hat{B}_1^+} \right]. \tag{2.19}$$

The advanced phase-based version named Simplified H-EPT [20] is also still being researched, e.g. [19], [21].

Any noise in the measurement data is amplified by the second-order differential operator and so results in artifacts in the reconstruction. The integral category contains approaches that use the scattering formalism in the reconstruction of the EP structure of the tissue. Due to the implicit summation of the integrals working as a low-pass filtering effect, the integral approaches are more robust against noise than the differential approaches.

2.2. SCALAR FIELD CONTRAST SOURCE INVERSION

The Contrast Source Inversion approach for EPT is a noise robust approach and useful for reconstructing inhomogeneous structures with the addition of regularization measures which improves the noise robustness and edge preservation characteristic [22]. CSI is in the integral EPT category in which most methods are generally posed as a hybrid inverse problem. Other integral EPT methods are Variational Born Iterative Method [23], Global Maxwell Tomography [24] and First-Order Induced Current EPT [25]. Hybrid inverse problems couple quantities from one physical domain with high resolution to that of another domain with high contrast [26]. Examples are electrical currents injected at the object domain boundary to use as the local sources to EM measurements

at the receivers like in MR-EIT or CDI (from electrical to EM) [27], [28]. In the case of CSI-EPT one set of electric fields generates sources for the receive set of magnetic fields to be measured (from EM to EM). It is noted here that the data acquisition domain S thus coincides with the object domain D, where the sources are, due to the imaging physics of MRI.

In order to explore CSI-EPT and the effects of regularization, the purpose of this section is to explain the Scattering Formalism and the basic CSI-EPT theory.

2.2.1. SCATTERING FORMALISM

The scattering formalism achieves integral equations for the transmit and receive fields from the Maxwell's equations. The mathematical formulation starts by describing the involved EM fields as a superposition of the incident fields and the scattered fields due to the presence of an object: $\{\hat{\mathbf{E}},\hat{\mathbf{H}}\} = \{\hat{\mathbf{E}}^{inc},\hat{\mathbf{H}}^{inc}\} + \{\hat{\mathbf{E}}^{sca},\hat{\mathbf{H}}^{sca}\}$. The fields incident from the source domain S abide the governing equations:

$$\hat{\mathbf{E}}^{inc} = (k_0^2 + \nabla\nabla\cdot)\hat{\mathbf{A}}^{ext} \quad \text{and} \quad \hat{\mathbf{H}}^{inc} = \eta_0 \nabla \times \hat{\mathbf{A}}^{ext} \tag{2.20}$$

wherein the wave number of the background medium is $k_0 = \omega/c_0$, c_0 is the electromagnetic wave speed in free-space and η_0 is the free-space admittance $\eta_0 = j\omega\varepsilon_0$. The vector potential $\hat{\mathbf{A}}^{ext}$ is the volume integral over S of the product of the Greens function $G(\mathbf{r})$ and the source external current density $\hat{\mathbf{J}}^{ext}(\mathbf{r})$ (i.e. the MRI coil current density):

$$\hat{\mathbf{A}}^{ext}(\mathbf{r}) = \frac{1}{\eta_0}\int_{\mathbf{r}'\in S} G(\mathbf{r}-\mathbf{r}')\hat{\mathbf{J}}^{ext}(\mathbf{r}')dV \tag{2.21}$$

$$G(\mathbf{r}) = \frac{\exp\left(-jk_0|\mathbf{r}|\right)}{4\pi|\mathbf{r}|} \tag{2.22}$$

The Green's tensors in $\mathsf{G}_D\{\mathbf{w}\}$ and $\mathsf{G}_S^+\{\mathbf{w}\}$ represent the EM fields propagating through the domain as the fields were effected by the contrast source. This Green's tensor choice considers a homogeneous background medium and not the presence of the MRI coils [29]. Specific Green's function is dependent on whether the reconstruction is performed in three or two dimensions and whether coil loading is considered.
Similarly, the governing equations for $\{\hat{\mathbf{E}}^{sca},\hat{\mathbf{H}}^{sca}\}$ and scattering vector potential $\hat{\mathbf{A}}^{sca}$ define the scattered fields, except the volume integral is over the object domain D and with induced scattering current density distribution $\hat{\mathbf{J}}^{sca}(\mathbf{r}) = (\eta(\mathbf{r}) - \eta_0)\hat{\mathbf{E}}(\mathbf{r})$ in

$$\hat{\mathbf{A}}^{sca}(\mathbf{r}) = \frac{1}{\eta_0}\int_{\mathbf{r}'\in D} G(\mathbf{r}-\mathbf{r}')\hat{\mathbf{J}}^{sca}(\mathbf{r}')dV. \tag{2.23}$$

Finally, the transmit field $\hat{B}^+$ can be obtained from the vector potentials using the first of the governing equations inside Faraday's law from the modified Maxwell's equations 2.15:

$$\nabla \times \left(k_0^2 + \nabla\nabla\cdot\right)\hat{\mathbf{A}}^u + j\omega\hat{\mathbf{B}}_1^u = \mathbf{0}, \tag{2.24}$$

wherein the superscript u denotes either the scattered or incident field. The term $\nabla \times (\nabla\nabla\cdot\hat{\mathbf{A}}^u)$ equals zero, thereby by solving for the magnetic field vector $\hat{\mathbf{B}}_1^u$. Now the inner

product with the $\mathbf{i}^+$ vector obtains an expression for the transmit field terms for both the incident and scattered fields:

$$\begin{aligned} \hat{B}_1^{+;tot} &= \hat{B}^{+;inc} + \hat{B}_1^{+;sca} \\ \hat{B}_1^{+;inc} &= \frac{\omega}{c_0^2}\tilde{\nabla}\cdot\hat{\mathbf{A}}^{ext} \\ \hat{B}^{+;sca} &= \frac{\omega}{c_0^2}\tilde{\nabla}\cdot\hat{\mathbf{A}}^{sca} \end{aligned} \tag{2.25}$$

wherein $\tilde{\nabla} = \mathbf{i}_z\partial^+ - \mathbf{i}^+\partial_z$.

2.2.2. CSI THEORY

Contrast Source Inversion was first introduced by Kleinman and van den Berg [30]. The algorithm is designed for iterative reconstruction of the complex index of refraction in an inhomogenous object. In this thesis the use of CSI for EPT is detailed in the context of MRI, where the contrast function χ is proxy to the index of refraction, which we are after as it contains the EP values. The contrast function at the three-dimensional position $\mathbf{r} \in D$ is

$$\chi(\mathbf{r}) = \frac{\eta(\mathbf{r}) - \eta_0}{\eta_0} = \varepsilon_r(\mathbf{r}) - 1 - j\frac{\sigma(\mathbf{r})}{\varepsilon_0\omega} \tag{2.26}$$

where domain D is the object domain, e.g. the patient body inside the MRI. This is the same domain as used in the scattering formalism. It is assumed that loading of the coils due to the presence of the object does not occur [29].

The object contrast is seen as a source for the scattering EM fields and the relation between this contrast source and contrast function is

$$\hat{\mathbf{w}}(\mathbf{r}) = \chi(\mathbf{r})\hat{\mathbf{E}}(\mathbf{r}), \tag{2.27}$$

with $\hat{\mathbf{E}}$ the total electric field.

CSI is a two-step updating algorithm, in each step either the contrast function or contrast sources are iteratively updated while the other is fixed. Given the prevalence in the method, the circumflex notation of the contrast sources is dropped; despite the time-harmonic dependence.

The term $\eta_0^{-1}\hat{\mathbf{J}}^{sca}$ from the scattered vector potential (eq. 2.23) is expressed in terms of this contrast source:

$$\mathbf{w}(\mathbf{r}) = \frac{\eta(\mathbf{r}) - \eta_0}{\eta_0}\hat{\mathbf{E}}(\mathbf{r}) = \frac{1}{\eta_0}\hat{\mathbf{J}}^{sca}(\mathbf{r}), \tag{2.28}$$

which allows the definition of the object and data operators using the scattered vector potential $\hat{\mathbf{A}}^{sca}$. The object operator describes the scattered electric field quantity at position $\mathbf{r}$ due to the presence of the contrast sources $\mathbf{w}$:

$$\mathsf{G}_D\{\mathbf{w}\}(\mathbf{r}) = \hat{\mathbf{E}}^{sca}(\mathbf{r}) = (k_0^2 + \nabla\nabla\cdot)\int_{\mathbf{r}'\in D} G(\mathbf{r}-\mathbf{r}')\mathbf{w}(\mathbf{r}')dV \tag{2.29}$$

Similarly, the data operator $\mathsf{G}_S^+\{\mathbf{w}\}(\mathbf{r})$ is defined as the scattered transmit field that is dependent on the contrast sources:

$$\mathsf{G}_S^+\{\mathbf{w}\}(\mathbf{r}) = \hat{B}_1^{+;sca}(\mathbf{r}) = \frac{\omega}{c_0^2}\tilde{\nabla}\cdot\int_{\mathbf{r}'\in D} G(\mathbf{r}-\mathbf{r}')\mathbf{w}(\mathbf{r}')dV \tag{2.30}$$

DEFINING THE COST FUNCTION

In the next step the required incident EM field quantities are either estimated from a reference scan or are simulated [13]. Recalling the superposition of the EM fields in Section 2.2.1, the sum of electric fields given a contrast function and sources is shown as $\hat{\mathbf{E}}^{inc} + \mathsf{G}_D\{\mathbf{w}\}(\mathbf{r}) = \hat{\mathbf{E}}$. Multiplying the sum with the contrast function gives the object residual $\rho_d(\mathbf{r})$ pertaining to a given contrast function:

$$\rho_d(\mathbf{r}) = \chi(\mathbf{r})\left(\hat{\mathbf{E}}^{inc} + \hat{\mathbf{E}}^{sca} - \hat{\mathbf{E}}\right) = \chi(\mathbf{r})\hat{\mathbf{E}}^{inc} + \chi(\mathbf{r})\mathsf{G}_D\{\mathbf{w}\}(\mathbf{r}) - \mathbf{w}(\mathbf{r}), \tag{2.31}$$

A low object residual value implies there is agreement in the contrast function and the total electric field. Simultaneously, the data residual $\rho_s(\mathbf{r})$ provides the connection between the MRI acquired transmit field data and the contrast function:

$$\rho_s(\mathbf{r}) = \hat{B}_1^{+;sca}(\mathbf{r}) - \mathsf{G}_S^+\{\mathbf{w}\}(\mathbf{r}) \tag{2.32}$$

Finally, the goal is to minimize these residual terms such that the reconstructed contrast function and sources correspond to the known incident electric field and the scattered transmit field data. First, the residuals from throughout the imaging domain are collected and normalized to form the object cost F_D and data cost F_S

$$F_D(\mathbf{w},\chi) = \frac{\left\|\rho_d\right\|_D^2}{\left\|\chi\hat{\mathbf{E}}^{inc}\right\|_D^2} \quad \text{and} \quad F_S(\mathbf{w}) = \frac{\left\|\rho_s\right\|_D^2}{\left\|\hat{B}_1^{+;sca}\right\|_D^2}, \tag{2.33}$$

where the L^2-norm of a function $f(\mathbf{r})$ is defined as $\left\|f\right\|_D^2 = \int_{\mathbf{r}\in D} |f(\mathbf{r})|^2 dV$.

CSI-EPT can also accept multiple EM measurement data sets, which are also referred to as the N different EM excitations. Consequently, the total cost function for CSI-EPT is

$$F(\mathbf{w},\chi) = \frac{\sum_{q=1}^N \left\|\rho_{d,q}\right\|_D^2}{\sum_{q=1}^N \left\|\chi\hat{\mathbf{E}}_q^{inc}\right\|_D^2} + \frac{\sum_{q=1}^N \left\|\rho_{s,q}\right\|_D^2}{\sum_{q=1}^N \left\|\hat{B}_{1,q}^{+;sca}\right\|_D^2} \tag{2.34}$$

ITERATIVE MINIMIZATION

The minimization is done with a two-step updating process. Each iteration n requires first to update the contrast source $\mathbf{w}^{(n-1)}$ while fixing the contrast function at $\chi^{(n-1)}$. This step is done using a gradient step of the total cost function $\mathbf{v}$ and a step size α. Hence the contrast sources update is:

$$\mathbf{w}^{(n)} = \mathbf{w}^{(n-1)} + \alpha^{(n)}\mathbf{v}^{(n)}. \tag{2.35}$$

With the new contrast sources, forward calculation of the electric field is done according to

$$\tilde{\mathbf{E}} = \hat{\mathbf{E}}^{inc} + \mathsf{G}_D\{\mathbf{w}^{(n)}\} \tag{2.36}$$

wherein the tilde denotes estimation of a field due to the use of an iteratively updated contrast source. Similarly, equation 2.30 now estimates the new scattered transmit field from the updated contrast source. The final step in the iteration is the updating of the contrast function with a similar gradient step used for the contrast source update. The contrast source $\mathbf{w}^{(n)}$ is fixed and the new contrast function is

$$\chi^{(n)} = \chi^{(n-1)} + \beta^{(n)}d^{(n)}, \tag{2.37}$$

where β is the step size and $d^{(n)}$ the gradient of the total cost function with respect to the contrast function χ. Calculation of the gradient vectors and step sizes is detailed in [22].

Alternatively, one can update the contrast function using

$$\chi^{(n)} = \frac{\mathbf{w}^{(n)} \cdot \tilde{\mathbf{E}}^*}{|\tilde{\mathbf{E}}|^2}, \tag{2.38}$$

which is the least squares solution to $\left\| \chi^{(n)} \hat{\mathbf{E}} - \mathbf{w}^{(n)} \right\|_D^2$, which is also referred to as the CSI or naive approach. Here, [22] notes that this result is "identical" to using the gradient-step to update the contrast function. Evidently, the CSI-EPT approach uses a forward calculation stage and two parameter updating steps.

THE LISTING

The following listing summarizes the CSI-EPT algorithm:

1. Determine the incident EM fields $\hat{\mathbf{E}}^{inc}$ and $\hat{B}_1^{+;inc}$ and provide $\hat{B}_1^{+;sca}$
2. Determine an initial contrast source $\mathbf{w}^{(0)}$ and from it the contrast $\chi^{(0)}$
3. **Initial forward calculation**: calculate the resulting EM fields with the appropriate object and data operators:
$$\tilde{B}_1^{+;sca} = \mathsf{G}_S^+ \{\mathbf{w}^{(0)}\}$$
and
$$\tilde{\mathbf{E}} = \hat{\mathbf{E}}^{inc} + \mathsf{G}_D \{\mathbf{w}^{(0)}\}$$
4. For each iteration n perform these steps until a convergence criterion has been met or the maximum number of iterations is reached:
   (a) **Update 1**: Update the contrast source while fixing the contrast function $\chi^{(n-1)}$:
   $$\mathbf{w}^{(n)} = \mathbf{w}^{(n-1)} + \alpha^{(n)} \mathbf{v}^{(n)}$$
   with a gradient step of the total cost function $F(\mathbf{w}^{(n-1)}, \chi^{(n-1)})$.
   (b) **Forward calculation** n: Recalculate the estimation $\tilde{B}_1^{+;sca}$ and $\tilde{\mathbf{E}}$ fields with the newly obtained contrast source.
   (c) **Update 2**: Calculate contrast function $\chi^{(n)}$ from $\left\| \chi^{(n)} \tilde{\mathbf{E}} - \mathbf{w}^{(n)} \right\|_D^2$
   Or, alternatively, find
   $$\chi^{(n)} = \chi^{(n-1)} + \beta^{(n)} d^{(n)}$$
   with a fixed contrast source $\mathbf{w}^{(n)}$ and a gradient step of the total cost function $F(\mathbf{w}^{(n)}, \chi^{(n-1)})$.
   (d) **Update costs**: Update the source and object residuals and normalization factors to compute the total cost $F(\mathbf{w}^{(n)}, \chi^{(n)})$.

3

CONTRAST SOURCE INVERSION EPT FOR MRI

In order to apply Contrast Source Inversion to the MRI acquired magnetic field data, knowledge of the complementary EM fields is required. Acquisition of such fields can be done with different methods. Additionally, there exist considerations for the initialization of contrast. Most importantly to this thesis, this chapter describes multiplicative regularization (MR) in CSI-EPT and especially the alternative Total Variation regularization. The current Chapter thus serves to highlight considerations in a broad and theoretical sense. The specific elaborations for the results of the thesis are presented in the next Chapter 4.

An overview of the considerations is given in Section 3.1. Thereafter, the latter four sections follow the sequential steps that determine the multiplicative regularized CSI-EPT starting point.

3.1. CSI-EPT CONSIDERATIONS OVERVIEW

Figure 3.1 graphically presents an overview of the different considerations required for the starting point of the CSI-EPT application. The four consideration domains are:

1. Input magnetic field data (Section 3.2): the transmit field data model that is the input to the CSI data cost function (equation 2.33).

2. Complementary EM field simulation (Section 3.3): the factors considered and assumptions made when simulating the EM fields complementary to the transmit field data.

3. Initialization of contrast sources (Section 3.4): the strategies to generate a starting contrast profile for the iterative algorithm.

4. Type of multiplicative regularization (Section 3.5): the options that are available in applying a regularized contrast updating step.

The multiplicative regularized CSI-EPT algorithm starts by determining one of the input data models to the CSI-EPT algorithm, thereby implicitly altering the presented basic CSI-EPT algorithm (Section 2.2). This also affects the complementary EM field simulation. Hence the order of discussion in the following sections is clockwise around the MRCSI-EPT algorithm in Figure 3.1.

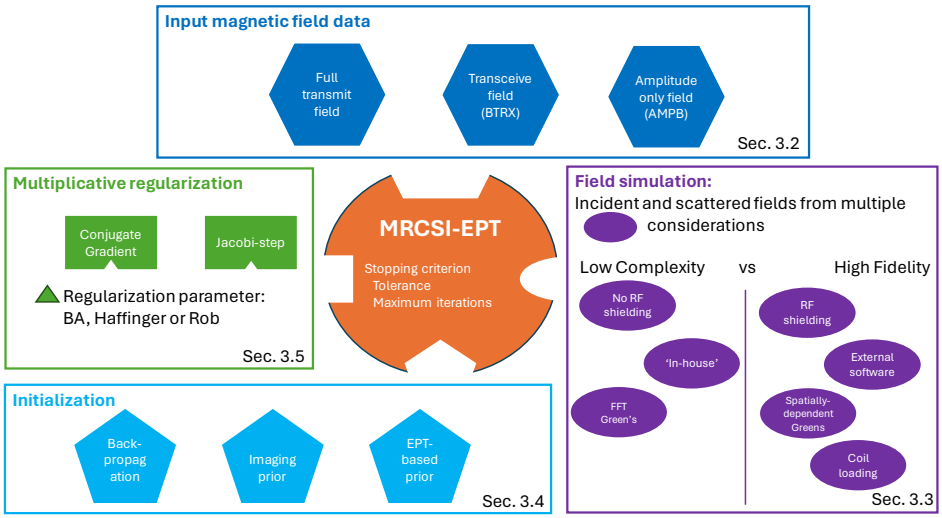

Figure 3.1: An overview of the different considerations for the reconstruction of the electrical properties using CSI-EPT.

3.2. INPUT MAGNETIC FIELD DATA

The forward field propagation of the incident and scattered EM fields can in certain situations be formulated in terms of E-polarized fields (e.g. in the birdcage MR coil [31], [32]) such that a two-dimensional version of the scattering formalism can be used for CSI-EPT. The resulting 2D CSI-EPT version operates on single slices of the object, which performs faster than the 3D version and is therefore more suited to extensively test the multiplicative regularization. The 2D formulation of the forward scattering data operator is presented first in Section 3.2.1.

The non-ideal transceive magnetic field data is discussed next, which requires adjustment of the data cost function. The data cost function verifies a given reconstructed contrast profile and subsequent fields against the measurement data. The latter is essentially retrieved from a spatial-frequency domain representation (the k-space) in MRI and aside from the effects in the signal model, given in equation 2.12, it is also dependent on the specific MRI geometry, data transmission and reception sequences; and object imaging region. However, to maintain a simple and ideal data model the initial assumption is made that the full transmit and receive field are tractable from MRI.

Yet, more realistic implementations will have to do with amplitude and partial phase information as can be read in Sections 3.2.2 and 3.2.3, wherein Transceive Phase Assumption based, Transceive Phase Correcting and Phaseless CSI-EPT versions are explained.

3.2.1. 2D FORMULATION

The 2D version of CSI-EPT is applicable to situations where a two-dimensional plane in the MRI system is essentially E-polarized. An E-polarized field structure in the context

of MRI is characterized by the presence of only longitudinal electric fields and transverse magnetic fields. Such a field structure occurs in the transverse plane in the center of a birdcage coil [29], also named the midplane. As is illustrated in the adapted Figure 3.2 the longitudinally oriented rungs that carry external current densities result in longitudinal electric fields and a two-dimensional magnetic field configuration [29].

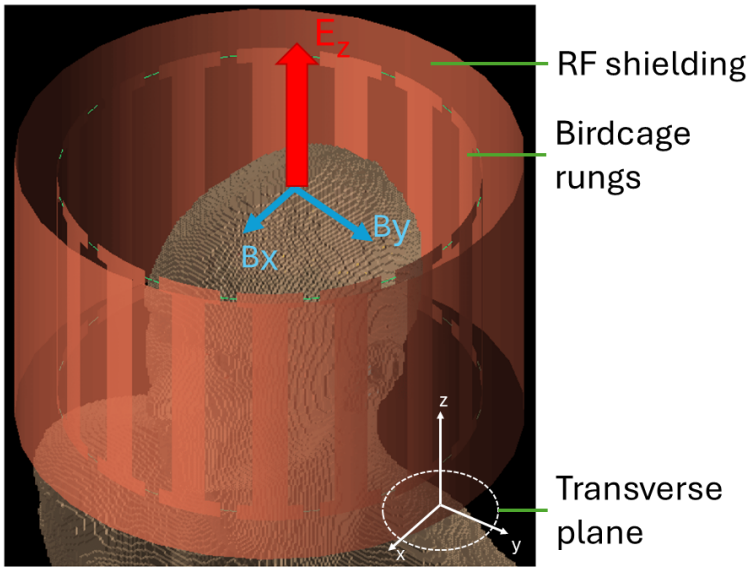

Figure 3.2: E-polarized EM field inside the birdcage coil due to currents running in the longitudinally oriented rungs. Adapted from [29, Figure 1a].

With the E-polarized field structure assumed, it is possible to present the governing equations 2.20 as

$$\hat{\mathbf{E}}_z^{sca}(\mathbf{x}) = k_0^2 \hat{\mathbf{A}}_T^{sca}(\mathbf{x}) \quad \text{and} \quad \hat{\mathbf{B}}_1^{sca}(\mathbf{x}) = j\frac{\omega}{c_0^2}\nabla_T \times \hat{\mathbf{A}}_T^{sca}(\mathbf{x}), \tag{3.1}$$

where $\mathbf{x}$ now denotes a position situated in the MRI slice that coincides with the two-dimensional midplane which is denoted as Ω. Furthermore, the transverse gradient vector is

$$\nabla_T = \left[\frac{\partial}{\partial_x}, \frac{\partial}{\partial_y}, 0\right]^T$$

and lacks the longitudinal component due to the assumed E-polarized field. Important to note is the lack of the gradient-divergence term in the scattered electric field and the altered vector potential now defined with

$$\hat{\mathbf{A}}_T^{sca}(\mathbf{x}) = \int_{\mathbf{x}' \in \Omega} G_T(\mathbf{x}-\mathbf{x}')\mathbf{w}(\mathbf{x}')dV \quad \text{and} \quad G_T(\mathbf{x}) = -\frac{j}{4}H_0^{(2)}(k_0|\mathbf{x}|), \quad \mathbf{x} \in \Omega \tag{3.2}$$

where the two-dimensional Green's function is the Hankel function of the second kind and order zero: $H_0^{(2)}$.

After applying the positive complex vector $\mathbf{i}^+ = (\mathbf{i}_x + j\mathbf{i}_y)/2$ the 2D scattered transmit scalar field is obtained as

$$\hat{B}_1^{+;sca}(\mathbf{x}) = \frac{\omega}{2c_0^2}\left(\partial_x + j\partial_y\right)\hat{A}_z(\mathbf{x}) = \frac{\omega}{c_0^2}\partial^+\hat{A}_z(\mathbf{x}) \tag{3.3}$$

The dependence on longitudinal variations in the transverse vector potential components is missing compared to the three-dimensional implementation of CSI-EPT (see equations 2.25) and instead the transmit scalar field is dependent only on transverse variations in the longitudinal vector potential field.

3.2.2. TRANSCEIVE PHASE FIELD RECONSTRUCTION

The inversion problem posed in Chapter 3 assumes full knowledge on the amplitude and phase of the transmit field, yet in reality only the amplitude is directly obtainable from an MRI scan [13], [33]. The phase information is mixed with contributions from the receive field in such a way that the retrieved magnetic field quantity is referred to as the transceive phase field:

$$\hat{B}_1^{+;TRX}(\mathbf{x}) = |\hat{B}_1^{+;tot}(\mathbf{x})|\exp\left[j(\phi^+(\mathbf{x}) + \phi^-(\mathbf{x}))\right] \tag{3.4}$$

wherein the $\phi^+(\mathbf{x})$ and $\phi^-(\mathbf{x})$ are the transmit and receive field phases respectively.

In order to apply CSI-EPT to such more realistic data, adjustments to the algorithm are required. Either an assumption on the data receive phase is made or there is implementation of a receive phase reconstruction method.

In the following sections the transceive phase assumption and transceive phase reconstruction method are presented. However, first an analysis of the consequent modification to the data cost function is warranted.

ANALYSIS OF LOCAL MINIMA FOR MODIFIED DATA COST

An analysis of local minima of the original cost functional (equation 2.34) was presented in [22], concluding that the likelihood of encountering a local minimum is decreased for an increased number of EM excitations N. The same analysis is repeated here for the modified data cost function that follows from the new magnetic field data model. The new data cost function becomes

$$\begin{aligned} F_S(\mathbf{w},\chi,\phi^-) &= \eta_S' \sum_{q=1}^{N} \left\| \hat{B}_{1,q}^{+;TRX}\exp(-j\phi_q^-) - \hat{B}_{1,q}^{+;inc} - \mathsf{G}_S^+\{\mathbf{w}_q\} \right\|_\Omega^2, \\ \eta_S' &= \left(\sum_{q=1}^{N} \left\| \hat{B}_{1,q}^{+;TRX}\exp(-j\phi_q^-) - \hat{B}_{1,q}^{+;inc} \right\|_\Omega^2 \right)^{-1}, \end{aligned} \tag{3.5}$$

where the adjustment to the receive phase component is a negative complex exponential multiplication in the residual as well as in the normalization η_S'. Furthermore, the incident field term compensates for the incident field term inside $\hat{B}_{1,q}^{+;TRX}$. The total cost

function thus becomes

$$F(\mathbf{w},\chi,\phi^-) = \eta_D \sum_{q=1}^{N} \left\| r_{D,q} \right\|^2 + \eta'_S \sum_{q=1}^{N} \left\| \hat{B}_{1,q}^{+;TRX} \exp(-j\phi_q^-) - \hat{B}_{1,q}^{+;inc} - \mathrm{G}_S^+\{\mathbf{w}_q\} \right\|_\Omega^2 \tag{3.6}$$

where the object cost is unaffected. Here the analysis continues by writing the variables at the point $\mathbf{p} \in \Omega$ as a linear combination of the exact solution and some generic direction:

$$[\mathbf{w}(\mathbf{p}) \quad \chi(\mathbf{p})]^T = [\mathbf{w}^{ex}(\mathbf{p}) \quad \chi^{ex}(\mathbf{p})]^T + \beta[\Delta\mathbf{w}(\mathbf{p}) \quad \Delta\chi(\mathbf{p})]^T \tag{3.7}$$

wherein $\mathbf{w} \in \mathbb{C}^N$ consists of N different coil setting excitations

$$\mathbf{w}(\mathbf{p}) = [w_1(\mathbf{p}) \quad w_2(\mathbf{p}) \quad \dots \quad w_N(\mathbf{p})]^T \tag{3.8}$$

β can be seen describing how far away from the exact solution our reconstruction of point $\mathbf{p}$ is. Next the receive phase is defined as consisting of the true receive phase and an arbitrary receive phase:

$$\phi^- = \phi^{-;ex} + \Delta\phi \tag{3.9}$$

And for brevity the fields are rewritten as f and necessary indications:

$$f_q = \hat{B}_{1,q}^{+;TRX} \qquad \text{and} \qquad f_q^{inc} = \hat{B}_{1,q}^{+;inc} \tag{3.10}$$

The data cost function therefore becomes:

$$F_S(\mathbf{w},\chi,\phi^-) = \eta'_S \sum_{q=1}^{N} \left\| f_q \exp(-j\phi_q^{-,ex}) \exp(-j\Delta\phi_q) - f_q^{inc} - \mathrm{G}_S^+\{\mathbf{w}_q^{ex}\} - \beta \mathrm{G}_S^+\{\Delta\mathbf{w}_q\} \right\|_\Omega^2 \tag{3.11}$$

Like in the original analysis, it is pointed out that most of the terms containing the exact solution vanish in the cost function. As such, the original relation of exact solution terms that sum to zero are used and shown here:

$$\begin{aligned} f_q^{tot} &= f_q \exp(-j\phi_q^{-,ex}) \\ f_q^{tot} &= \mathrm{G}_S^+\{\mathbf{w}_q^{ex}\} + f_q^{inc} \end{aligned} \tag{3.12}$$

In words, the total field is the transceive field adjusted for the true transceive phase (line 1) but it is also the sum of the exact solution scattered field and the incident field (line 2).

However, when writing out the cost function using these two total field definitions, the exact solution terms do not quite vanish but remain in the l_2-norm as they are adjusted by the arbitrary receive phase term. This is shown in the derivation below

$$\begin{aligned} F_S(\mathbf{w},\chi,\phi^-) &= \eta'_S \sum_{q=1}^{N} \left\| f_q^{tot} \exp(-j\Delta\phi_q) - f_q^{tot} - \beta \mathrm{G}_S^+\{\Delta\mathbf{w}_q\} \right\|_\Omega^2 \\ &= \eta'_S \sum_{q=1}^{N} \left\| f_q^{tot} \left(\exp(-j\Delta\phi_q) - 1\right) - \beta \mathrm{G}_S^+\{\Delta\mathbf{w}_q\} \right\|_\Omega^2 \\ &= \eta'_S \sum_{q=1}^{N} \sum_{p=1}^{N_\Omega} \left[\left[f_q^{tot} \left(\exp(-j\Delta\phi_q) - 1\right) \right]^2 - 2\beta f_q^{tot} \left(\exp(-j\Delta\phi_q) - 1\right) \mathrm{G}_S^+\{\Delta\mathbf{w}_q\} + \beta^2 \mathrm{G}_S^+\{\Delta\mathbf{w}_q\}^2 \right] \end{aligned} \tag{3.13}$$

wherein the last line expanded the l_2-norm using the N_Ω different points p inside the discretized 2D domain Ω, however, dependencies on location for the data operator, f_q^{tot} and ϕ_q^- have been left out to prevent clutter.

Now shortly returning to the original total cost function (introduced in equation 2.34), the original analysis in [22] presents a quartic polynomial with respect to β for the particular excitation q.

$$\begin{aligned} F(\mathbf{w}_q, \chi) &= A_D\beta^4 + 2B_D\beta^3 + C_D\beta^2 + C_S\beta^2, \\ C_S &= \eta_S \sum_q \left\| \mathrm{G}_S^+\{\Delta\mathbf{w}_q\} \right\|_S^2, \end{aligned} \tag{3.14}$$

where the three parameters A_D, B_D and C_D originate from the unaffected object cost function (see Appendix A.2 for clarification) and are assumed unchanged. The final parameter C_S is changed as is seen in equation 3.13 and thus the point of focus.

The analysis in [22] continues by mentioning that the derivative of the polynomial with respect to the β parameter is a cubic polynomial with two minima, the global and local minima.

The quartic polynomial that is reached using the modified data cost is:

$$\begin{aligned} F(\mathbf{w}, \chi, \phi^-) = &A_D\beta^4 + 2B_D\beta^3 + C_D\beta^2 \\ &+\eta_S' \sum_{q=1}^{N} \left[\left[f_q^{tot} \left(\exp(-j\Delta\phi_q) - 1 \right) \right]^2 - 2\beta f_q^{tot} \left(\exp(-j\Delta\phi_q) - 1 \right) \mathrm{G}_S^+\{\Delta\mathbf{w}_q\} + \beta^2 \mathrm{G}_S^+\{\Delta\mathbf{w}_q\}^2 \right] \end{aligned} \tag{3.15}$$

and when the derivative to β is employed, again a cubic polynomial is retrieved:

$$\begin{aligned} \frac{dF_{tot}}{d\beta} &= 4A_D\beta^3 + 6B_D\beta^2 + 2C_D\beta \\ &\quad +\eta_S' \sum_{q=1}^{N} \left[-2 f_q^{tot} \left(\exp(-j\Delta\phi_q) - 1 \right) \mathrm{G}_S^+\{\Delta\mathbf{w}_q\} + 2\mathrm{G}_S^+\{\Delta\mathbf{w}_q\}^2 \beta \right] \\ &= 4A_D\beta^3 + 6B_D\beta^2 + 2C_D\beta + E + 2C_s'\beta \end{aligned} \tag{3.16}$$

Finally, it is seen that an introduction of an arbitrary phase term only affects the derivative with a constant E. This simply denotes an additive and linear term w.r.t. β and is therefore ineffectual to the conclusions of the original analysis of local minima of the cubic equation.

However, there is still the question of the effects due to a modified normalization factor η_S' on the now modified parameter C_S' as compared to the original C_S. [22] presents the condition

$$\frac{C_D}{C_S + C_D} < \frac{8}{9} \tag{3.17}$$

that must be satisfied to guarantee absence of local minima. The article then mentions how violating this condition can occur due to a too large object normalization factor η_D present inside C_D relative to the data normalization factor inside C_S.

In the case of the new data normalization factor η_S', the added exponential phase component can increase or decrease the value η_S' and thereby that of C_S'. In the latter

situation the condition is at risk of no longer being satisfied, while increasing the C'_S is inconsequential to the condition. Therefore it is concluded that phase reconstructing CSI-EPT is encounters local minima more often than full transmit field CSI-EPT and so may slow the reconstruction process.

TRANSCEIVE PHASE ASSUMPTION

The Transceive phase assumption (TPA) refers to the assumption where the phases of the transmit and receive fields are similar and so one considers half of the measured phase to come from the transmit field while the other half belongs to the receive field [33]. Implementating the TPA into a transceive phase data based reconstruction, one would set the compensating phase ϕ_q^- in equation 3.5 equal to half of the total measured phase.

However, the TPA has been shown accurate in the case that a low main field strength is used for symmetric objects with low permittivity, while a simple elliptical object can already cause the scattered fields to become elliptically polarized and thus the TPA loses its validity here [34]. The latter effect is also reported by the same article as exacerbated by higher main field strengths (7T or higher) or high object permittivity. The ability to perform EPT at higher field strengths and low geometric constraints on the imaged object is desirable for the improvements in SNR and larger applicability of EPT, respectively. For that reason a more involved CSI-EPT version exists which is described next.

TRANSCEIVE PHASE CORRECTION CSI-EPT

Stijnman et al. [33] presented a transceive phase based data CSI-EPT algorithm using receive field operators to reconstruct the transceive phase term. The so-called Transceive Phase Corrected (TPC) CSI-EPT method adds a forward calculation of the receive field after updating of the contrast. The receive phase ϕ^- is found as the phase angles of the total receive magnetic field. The incident receive field is simulated, while the conjugate of the receive field in iteration n is reconstructed as

$$\tilde{B}_1^{-;sca;*}(\mathbf{x}) = \mathsf{G}_S^-\{\chi^{(n)}\mathbf{E}_z^-\} = -\frac{1}{\omega}k_0^2\partial^- \int_{\mathbf{x}'\in\Omega} G(\mathbf{x}-\mathbf{x}')\chi^{(n)}(\mathbf{x}')\mathbf{E}_z^-(\mathbf{x}')\,dV \tag{3.18}$$

Note the transverse variation dependence in the Wirtinger derivative ∂^- similar to the E-polarized transmit field in equation 3.3.

The TPC CSI-EPT iteration can finish by updating the new cost function using the modified data cost function from equation 3.5 after finding the receive phase from the updated contrast sources, contrast and total electric fields (see subsection 3.2.2). The following paragraphs elaborate on the practical implementation of the TPC and an overview of the TPC algorithm in terms of the fields follows. The calculation and implementation of the scattered receive field (equation 3.18) is discussed in the next chapter.

Receive state TPC Due to the nature of the birdcage coil it is most efficient to transmit the incident EM fields in quadrature rather than with linear excitation. In quadrature transmission the receive field contributions are minimal, which means that the transmit field acquires most of the input energy. However, this receive field is still required in the reconstruction of the receive phase so a distinction is made between the use of TPC in combination with quadrature transmission and use of TPC in linear transmission.

For the purposes of using TPC in quadrature transmitted MRI there are two MRI scans required. One for measuring the amplitude of the magnetic field ($B_1^{+;tot}$), which is done while the RF coils are in transmit mode, i.e. positive 90 degree phase shift between the currents on the two ports on the coil. The second scan measurement is done in receive mode, when the rung currents experience a phase shift in the opposite direction, negative 90 degree phase shift between the coil ports. Using this scan the transceive phase is measured.

Clearly there are two different incident electric fields required to use TPC for quadrature transmitted MRI, one in transmit mode (further referred to as $\mathbf{E}_z^+$) and one in receive mode ($\mathbf{E}_z^-$). This is not the case for the linearly transmitted MRI measurements, where there is only one set of EM fields per measurement. Hence it is possible to directly apply equation 3.18 using the same electric field for the scattered receive field as for the scattered transmit field, thus $\mathbf{E}_z^- = \mathbf{E}_z$.

The TPC CSI-EPT algorithm The so-called Transceive Phase Corrected (TPC) CSI-EPT method adds a forward calculation of the receive field as can be seen in step 4 of the following 2D TPC CSI-EPT listing. Also note, previously in the data operator of basic CSI-EPT the contrast source $\mathbf{w}$ is used inside this operator instead of the contrast and electric field product as is done in TPC CSI-EPT in step 4b.

- Determine the EM fields $\hat{\mathbf{E}}_z^{inc}$, $\hat{B}_1^{+;inc}$ and $\hat{B}_1^{+;sca}$; and the receive fields $\hat{\mathbf{E}}_z^{-;inc}$, $\hat{B}_1^{-;inc}$ and $\hat{B}_1^{-;sca}$
- Determine the initial (transmit) contrast source $\mathbf{w}^{(0)}$ and from it the contrast $\chi^{(0)}$
- **Initial forward calculation**: calculate the total EM fields with the appropriate object and data operators:

$$\tilde{B}_1^{+;sca} = \mathsf{G}_S^+\{\mathbf{w}^{(0)}\} \quad \text{and} \quad \tilde{B}_1^{-;sca;*}(\mathbf{x}) = \mathsf{G}_S^-\{\chi^{(0)}\mathbf{E}_z^-\}$$

  and

$$\tilde{\mathbf{E}}_z^{\pm} = \hat{\mathbf{E}}_z^{\pm;inc} + \mathsf{G}_D\{\chi^{(0)}\mathbf{E}_z^{\pm}\}$$

- Determine the initial receive phase ϕ^-
- For each iteration n perform these steps until a convergence criterion has been met or the maximum number of iterations is reached:
  1. Update contrast source with conjugate gradient using $F(\mathbf{w}^{(n-1)}, \chi^{(n-1)}, \phi^{-;(n-1)})$
  2. Forward calculation of transmit $\mathbf{E}_z^+(\mathbf{x})$
  3. Update contrast to $\chi^{(n)}(\mathbf{x})$ using $F(\mathbf{w}^{(n)}, \chi^{(n-1)}, \phi^{-;(n-1)})$
  4. Update receive phase (either in quadrature receive state or using linear EM fields):
     (a) compute $\mathbf{E}_z^-$ during reception with $\chi^{(n)}$
     (b) compute total receive field: $\tilde{B}_1^-(\mathbf{x}) = \hat{B}_1^{-;inc}(\mathbf{x}) + \tilde{B}_1^{-;sca}(\mathbf{x})$

$$\tilde{B}_1^{-;sca;*}(\mathbf{x}) = \mathsf{G}_S^-\{\chi^{(n)}\mathbf{E}_z^-\}$$

(c) retrieve receive phase $\phi^{-;(n)} = \text{angle}(\tilde{B}_1^-)$

5. update total cost with the modified cost functional $F(\mathbf{w}^{(n)}, \chi^{(n)}, \phi^{-;(n)})$

3.2.3. PHASELESS DATA RECONSTRUCTION

For a sense of completeness, potential CSI-EPT reconstruction based on phaseless transmit field data is discussed as well. The book titled "*Forward and Inverse Scattering Algorithms Based on Contrast Source Integral Equations*" by P.M. van den Berg describes two options for implementation of phaseless input magnetic field data[15, Section 4.8]. There are the intensity and amplitude based residual errors to base the data cost functional around. For a position $\mathbf{p}$ inside source domain S the **intensity** residual error corresponding to source q is

$$r_{S,q}(\mathbf{p}) = \left|\hat{B}_q^{+;tot}(\mathbf{p})\right|^2 - \left|\hat{B}_q^{+;inc}(\mathbf{p}) + \mathsf{G}_S^+\{\mathbf{w}_q\}(\mathbf{p})\right|^2, \tag{3.19}$$

whereas the **amplitude** residual error is

$$r_{S,q}(\mathbf{p}) = \left|\hat{B}_q^{+;tot}(\mathbf{p})\right| - \left|\hat{B}_q^{+;inc}(\mathbf{p}) + \mathsf{G}_S^+\{\mathbf{w}_q\}(\mathbf{p})\right| \tag{3.20}$$

The data cost functionals are still the same: $F_S(\mathbf{w}, \chi) = \eta_S \sum_{q=1}^{N} \left\| r_{S,q} \right\|^2$.

Note that both residual errors need the full approximated scattered transmit field, i.e. its phase and its amplitude, to be reconstructed. The normalization terms η_S are the same as the residual errors except for leaving out the scattered field terms right of the negative signs. Updating of the step lengths α are respectively found from the roots of a cubic equation or from solving a transcendental equation (the latter is generally not doable algebraically and requires approximation).

Arduino et al. 2018 [35] describes the use of the intensity option (as described above) and the solving of the step length using the cubic equation solution from [36]. Noisy experiments were performed with SNR factor that represented 2% and 5% of the average $|\hat{B}_1^+|^2$ (= SNRdb levels 34dB and 26 dB) and 200 iterations, while noting that stopping early can be used as a regularization technique against noise.

3.3. ELECTROMAGNETIC FIELD SIMULATION

The complementary fields are the incident electric and magnetic fields and the initialized scattered electric field. As mentioned these can be retrieved with EM simulation software or from a reference scan. The following subsections detail considerations regarding influences on the retrieved EM simulations: RF shielding, coil loading, external software simulation and the spatially-invariant FFT implementation. It is important to note that this list is not complete. For example, this thesis discusses the E-polarized EM simulation case only, therefore considerations for reference scanning and other EM field configurations have not been documented.

The simulation approaches generally start with modeling the produced incident electric and magnetic fields as affected by the relevant MRI environment, i.e. methodical considerations. Secondary are the implementation considerations. In general, taking into account more realistic methodical considerations or increasing to higher fidelity implementation can affect the CSI-EPT performance due to general higher complexity of the algorithm.

3.3.1. RADIOFREQUENCY SHIELDING

An RF shield component is implemented in the design of an MRI machine. It protects external devices from the strong EM fields generated. [33] argues the RF shielding be taken into account for reconstructing EP profiles in the case of realistic MRI measurements "as these fields are only accessible via simulations". There are two documented approaches for E-polarized field simulation: adjust the Green's tensors or implement mirror currents.

RF SHIELD ADJUSTED GREEN'S TENSORS

The first option requires that the imaging domain now contains an RF shield in the form of a cylindrical perfectly electrically conducting surface which imposes the longitudinal electric field at the boundary of the cylinder to become zero. Such an approach is presented in [37], where the partial differential equation problem of equations 2.15 is modified to become

$$\begin{cases} -\Delta E_z^{tot} - k_b^2 E_z^{tot} = k_b^2 w_z, & \text{in } \Omega \\ E_z^{tot} = 0, & \text{on } \partial\Omega \end{cases} \tag{3.21}$$

wherein Ω and $\partial\Omega$ are the imaging domain and the RF shielding domain, respectively, and the w_z are the RF field sources. By solving for this particular PDE, Green's tensors can be obtained that apply to the propagation behaviour of the fields in the shielded environment.

MIRROR SOURCES FOR RF SHIELD SIMULATION

However, due to the rigid nature of having to define the RF shield location and the loss of spatial invariance of the Green's tensors, Stijnman et al. [33] argues that using mirror sources is better suitable to enforce a net-zero longitudinal electric field at the PEC boundary than the previous method.

The shield implemented in such simulation of the incident electric fields, therefore also the magnetic fields, is described in [33] and is based on placing mirroring currents to simulate a PEC material cylinder just around the coils of the MRI machine. Mirrored sources are placed at distance

$$d + R_s = \frac{R_s^2}{R} \tag{3.22}$$

radially from the central axis of the bore, wherein R_s is the radius of the shield, R is the radius of the RF field electric sources and d is the distance between the shield and the mirror sources [38].

3.3.2. COIL LOADING

Introducing an object into the imaging domain not only affects the scattered fieldsbut also the incident electric fields due to loading of the MRI coils. The coil-object interactions at high fields (>3T) influence the incident fields [39] due to the altered current distribution on the coil surface [40]. Furthermore, the birdcage coil reconstructions in particular suffer from unloaded incident fields [40].

Hence reconstruction errors due to incident field simulations with coil loading objects has been investigated [39]. The study loaded and tuned the coils with various sub-

stitute models the Ella Virtual Family model[1], homogeneous dielectric sphere and the empty coil. Subsequently, the incident fields were simulated and used for reconstruction of the Duke Virtual Family head model. The resulting reconstruction errors were deemed not severe when a comparable reference object was used for the field simulation, e.g. Ella model for the Duke model reconstruction, but otherwise blurring artifacts occur [39].

Alternatively, [40] proposes a modified conjugate gradient method based on "hybrid" sources operators instead of contrast sources based operators. The hybrid sources consider the coil currents, occuring in the source domain S, and the contrast sources occuring in the object domain D. Thereby this modified method iteratively updates the incident fields as well as the scattered fields, whereas only the latter is updated in basic CSI-EPT.

3.3.3. EXTERNAL SOFTWARE AND THE FFT

The previously discussed considerations for modeling the imaging domain are to be implemented in either external simulation software or simulation is performed "in-house", i.e. where the CSI-EPT algorithm is performed. This distinction roughly marks the trade-off between high fidelity simulation and the complexity of implementation. For example, the generation of explicit Green's tensors using RF shield modeling and accurate coil loading objects using external simulation software can be expected to achieve accurate results.

Alternatively, the convolutions in the forward modeling operators $\mathsf{G}_D\{\mathbf{w}\}$ and $\mathsf{G}_S^+\{\mathbf{w}\}$ can be formulated using the Fast Fourier Transform. However, this requires spatially-invariant modeling of the object dependent EM influences (e.g. RF shielding) as the FFT implementation requires spatial-invariance of the Green's tensors [33]. Such implementation is lower in complexity and thus faster than the explicit Green's tensor convolutions.

3.4. INITIALIZATION OF CONTRAST SOURCES

Despite optimizing two variables in their respective solution spaces, i.e. the contrast and contrast sources, Contrast Source Inversion in principle requires only one variable to be initialized. Using the relation $\mathbf{w} = \chi\mathbf{E}$ and its least squares minimizer

$$\chi = \frac{\sum_i w_i E_i^*}{\sum_i |E_i|^2}$$

the other variable can be initialized accordingly. Hence the following initialization strategies discuss either contrast or contrast source initialization.

Broadly speaking three strategies of initialization methods have been identified and summarized here. The first is minimization of the data cost function. The second strategy is based on prior anatomical knowledge of the imaged region or entire object. Therefore this requires availability of such knowledge to initialize based on an (imperfect) contrast distribution. Finally, there is initialization based on other MR-EPT methods.

[1] The Virtual Family is a set of simulated body models based on the database of the IT'IS Foundation (see https://itis.swiss/virtual-population/).

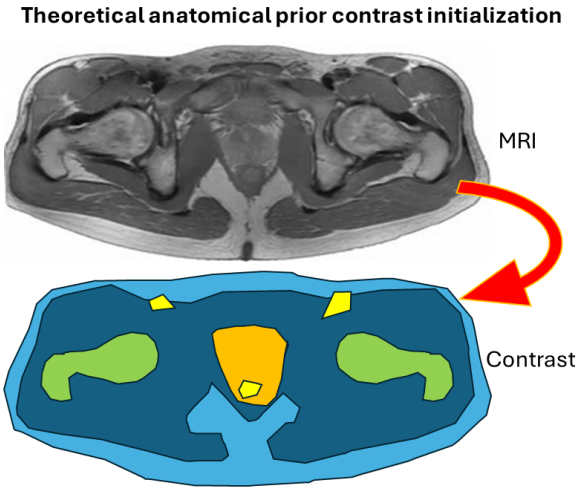

Figure 3.3: Anatomical prior initialization example from MRI image to contrast contrast initialization. Adapted from [41, Figure 12].

3.4.1. MINIMIZATION OF DATA RESIDUAL

Initialization of contrast source from excitation j is done using back propagation [22] for which the following contrast source is initialized based on the imaging data and simulation of the incident magnetic field $\hat{B}^{+;tot}$:

$$\mathbf{w}_{j,bp}^{(0)} = \frac{\left\| \mathsf{G}_S^{+*}\{\hat{B}_j^{+;tot;(0)}\} \right\|_D^2}{\left\| \mathsf{G}_S^{+}\left\{ \mathsf{G}_S^{+*}\{\hat{B}_j^{+;tot;(0)}\} \right\} \right\|_S^2} \mathsf{G}_S^{+*}\{\hat{B}_j^{+;tot;(0)}\}, \tag{3.23}$$

with G_S^{+} and G_S^{+*} the data operator and its adjoint, which map the contrast sources to scattered transmit fields while the adjoint operator does the opposite. This initialization minimizes the starting data cost for the scattered and incident fields.

3.4.2. ANATOMICAL PRIOR KNOWLEDGE

When executing MR imaging for CSI-EPT it is thought within practical limits to perform simultaneous or sequential MRI or CT imaging, even in clinical setting, to acquire anatomical prior information. Such prior information based on (other) imaging modalities can give insight into the object characteristics of general tissue boundary locations and potential dielectric volume distribution. Therefore, the anatomical prior may aid in initializing a contrast distribution that brings the first iteration of the CSI-EPT algorithm close to the optimal solution. Figure 3.3 illustrates this theoretical transformation from an MRI image to a contrast initialization. A secondary option is the use of known distributions from for example a Virtual Family object.

3.4.3. EPT INITIALIZATION

The final initialization approach is to utilize other EPT methods based on either the same MRI data or other modalities. The rationale is to potentially skip passed the initial CSI-EPT iterations. As additional consideration one can focus on computationally inexpensive EPT methods to reduce the total time to diagnosis further. A final method of streamlining the medical process is to make minimal use of different modalities and resources by considering only MR-EPT methods and not from other modalities.

Three different MR-EPT initialization methods for three-dimensional CSI-EPT has been investigated in [42]. The differential H-EPT method for initialization of CSI-EPT reconstruction of the head still is susceptible to the noise according to the results. Furthermore, initialization with a trained deep learning based model [43] has been shown to yield considerably better results than performing CSI-EPT with a homogeneous contrast profile as initialization.

3.5. MULTIPLICATIVE REGULARIZATION

Regularization is incorporating *a priori* information into the reconstruction process in order to improve the reconstruction quality. In the current context, anatomical prior information is mathematically formulated such that the final result is steered towards a reconstruction with the wanted physical properties. This is done with a punishing term that increases the cost of contrast profiles without these properties.

The Tikhonov regularization term, i.e. l_2-norm regularization, is commonly used to create smooth reconstructions thereby reducing noise influence, however, it is unsuitable for modeling discontinuities [15]. The property that is of interest to EPT is minimal total variation, i.e. reconstructions with piece-wise constant structures. Thus application of total variation (TV) regularization has two benefits: reduction of noise (the constant value structures) and edge-preservation (the piece-wise characteristic) [15].

Usually the regularization term $F_R(\chi)$ is additive to the cost functional,

$$F_{tot}(\mathbf{w},\chi) = F_S(\mathbf{w}) + F_D(\mathbf{w},\chi) + \lambda F_R(\chi),$$

however, this introduces a regularization parameter λ that defines the influence of the *a priori* knowledge during the reconstruction process. The choice of the parameter value is commonly found through iterative methods. However, this is cumbersome and computationally expensive.

CONJUGATE GRADIENT REGULARIZATION

Through numerical experimentation the idea of multiplicative regularization (MR) originated and emerged into the form [15], [44]

$$F_{tot}(\mathbf{w},\chi) = \left[F_S(\mathbf{w}) + F_D(\mathbf{w},\chi)\right] F_R(\chi), \tag{3.24}$$

wherein the multiplicative regularization term becomes the weighted-integral total variation $F_R(\chi) = F_{TV}^{(n)}(\chi)$:

$$F_{TV}^{(n)}(\chi) = \frac{1}{V}\int_{\mathbf{x}\in\Omega} \frac{|\nabla\chi(\mathbf{x})|^2 + \delta^{(n)}}{|\nabla\chi^{(n-1)}(\mathbf{x})|^2 + \delta^{(n)}} dV(\mathbf{x}), \tag{3.25}$$

which is also elaborated in [22], [45]. Note the new $\delta^{(n)}$ regularization parameter. The purpose of this regularization parameter, instead of the additive regularization parameter, is to have the influence of the regularization be dependent on the errors in the data and object costs. Instead of determination of an arbitrary value λ, the MR regularization parameter 'evolves' with the reconstruction as it is a function based on the previous and current contrast reconstructions.

The regularization factor punishes a large amount of variation in the reconstructions due to the gradient factor in the numerator. Therefore it has a noise suppression effect on the reconstruction. Furthermore, the multiplicative regularization equals one when the input contrast function is $\chi^{(n-1)}$, i.e. $F_{TV}(\chi^{(n-1)}) = 1$. This occurs in the first update step when the contrast function is fixed and therefore will not affect the contrast source updates.

To update the contrast function using the regularized reconstruction method we can no longer make use of the least-squares (LS) solution $\left\|\chi^{(n)}\tilde{\mathbf{E}} - \mathbf{w}^{(n)}\right\|_D^2$, i.e. the contrast source error norm, and instead the contrast is updated with Polak-Ribière updating directions $d^{(n)}$ as detailed in [22].

SECTION OUTLINE

The alternative formulation of multiplicative TV regularization is introduced first. Briefly, the resulting Jacobi step CSI-EPT algorithm is introduced. Finally, Section 3.5.3 discusses the various multiplicative regularization parameter functions further.

3.5.1. ALTERNATIVE TV REGULARIZATION

P. M. van den Berg [15] details an alternative formulation of the weighted-integral TV regularization that allows the contrast to be updated and regularized with the numerical Jacobi algorithm. It is characterized by its regularization strength in part being determined by the data cost functional and the mean of the LS-solution:

$$\chi_{csi}^{(n)} = \arg\min_{\chi} \left\|\chi^{(n)}\tilde{\mathbf{E}} - \mathbf{w}^{(n)}\right\|_D^2, \tag{3.26}$$

for which the solution is

$$\chi_{csi}^{(n)}(\mathbf{r}) = \frac{\mathbf{w}^{(n)}(\mathbf{r}) \cdot \tilde{\mathbf{E}}^*(\mathbf{r})}{|\tilde{\mathbf{E}}(\mathbf{r})|^2}. \tag{3.27}$$

[15, Section 4.6] introduces an altered objective cost functional $F_I(\mathbf{w})$ by posing the multiplicative regularization to be a minimization of the changes between the regularized contrast and the LS-solution

$$\chi_c^{(n)} = \arg\min_{\chi} \left[\int_{\mathbf{r}\in D} |\chi^{(n)}(\mathbf{r}) - \chi_{csi}^{(n)}(\mathbf{r})|^2 dV\right] \tag{3.28}$$

$$F_I(\mathbf{w}) = \frac{\int_{\mathbf{r}\in D} \left|\chi - \chi_{csi}^{(n)}\right|^2 dV}{\int_{\mathbf{r}\in D} \left|\chi_{csi}^{(n)}\right|^2 dV}. \tag{3.29}$$

It is known that $\chi_{csi}^{(n)}$ minimizes the objective cost functional $F_D(\mathbf{w},\chi)$ as was seen in equation 3.26. As both vector quantities are known to result in $\chi_{csi}^{(n)}$ as optimal solution during any iteration, calculating F_D and its replacement F_I is equivalent. Therefore

the original cost functional of equation 3.24 is reformulated by replacing the object cost functional with the integral-over-integral version $F_I(\mathbf{w})$, hence the complete cost functional becomes:

$$F(\mathbf{w},\chi) = \left[\frac{\int_{\mathbf{r}\in D} \left|\chi - \chi_{csi}^{(n)}\right|^2 dV}{\int_{\mathbf{r}\in D} \left|\chi_{csi}^{(n)}\right|^2 dV} + F_S(\mathbf{w}) \right] F_R(\chi), \tag{3.30}$$

wherein $F_R(\chi)$ is the new total variation regularization functional discussed next.

DERIVING THE NONLINEAR EULER-LAGRANGE EQUATION ALTERNATIVE

The alternative TV regularization form starts with reformulating the weighted-integral TV cost functional $F_{TV}^{(n)}(\chi)$ in equation 3.25. The denominator in the integral is now seen as weights $b^{(n)}$ for the contents of the integral and the mesh size $(\Delta x)^2$ is multiplied on the top and bottom to facilitate discretization and gradient calculations later in the implementation.

$$F_R(\chi) = \frac{(\Delta x)^2}{V} \int_D \left[b^{(n)} \left|\nabla\chi\right|^2 + b^{(n)}\delta^{(n)} \right] dV, \tag{3.31}$$

with the weights $b^{(n)}$ declared as

$$b^{(n)}(\mathbf{r}) = \frac{1}{(\Delta x)^2} \frac{1}{\left|\nabla\chi_{csi}^{(n)}(\mathbf{r})\right|^2 + \delta^{(n)}}. \tag{3.32}$$

The first integral term on the right-hand side can be decomposed as

$$b^{(n)} \left|\nabla\chi\right|^2 = \mathrm{div}(\chi^* b^{(n)} \nabla\chi) - \chi^* \mathrm{div}(b^{(n)}\nabla\chi), \tag{3.33}$$

where $\mathrm{div}(\mathbf{f}) = \nabla\cdot\mathbf{f}$ and χ^* the conjugate of the contrast. Noting that the objective domain D is a closed and bounded surface, the Divergence theorem is applied with the result:

$$\int_D \mathrm{div}\left(\chi^* b^{(n)}\nabla\chi\right) \mathrm{dV} = \int_{\partial D} \left(\chi^* b^{(n)}\nabla\chi\right)\cdot\nu \mathrm{dA} = 0, \tag{3.34}$$

wherein ν is the normal vector on the surface ∂D. The vanishing conjugate contrast χ^* at the boundary of the object domain gives a zero-value for the first term of equation 3.33. In the context of MRI this represents the assumption that there is no contrast present close to the MRI coils inside the scanner.

Thus the regularization functional is now

$$F_R(\chi) = \frac{(\Delta x)^2}{V} \int_{\mathbf{r}\in D} \left[-\chi^* \mathrm{div}(b^{(n)}\nabla\chi) + b^{(n)}\delta^{(n)} \right] dV. \tag{3.35}$$

Applying calculus of variations [46] (specifically the Euler-Lagrange equation for the first variation functional with respect to the χ^* function) to the newly formulated cost func-

tional in equation 3.30 a non-linear Euler-Lagrange equation is retrieved [15]:

$$\left[\frac{\chi-\chi_{csi}^{(n)}}{\int_{\mathbf{r}\in D}\left|\chi_{csi}^{(n)}\right|^2 \mathrm{dV}}\right] F_R^{(n)}(\chi) - \left[F_S(\mathbf{w}) + \frac{\int_{\mathbf{r}\in D}\left|\chi-\chi_{csi}^{(n)}\right|^2 dV}{\int_{\mathbf{r}\in D}\left|\chi_{csi}^{(n)}\right|^2 dV}\right] \frac{(\Delta x)^2}{V}\mathrm{div}\left[b^{(n)}\nabla\chi\right] = 0 \tag{3.36}$$

SOLVING FOR THE LINEARIZED REGULARIZATION EQUATION

Equation 3.36 is linearized with respect to the inner-iteration contrast difference term $\chi(\mathbf{r}) = \chi_{csi}^{(n)} + \delta\chi(\mathbf{r})$ by retaining only the first order terms of $\delta\chi$. After rewriting and using the fact that $F_R(\chi_{csi}) = 1$, the linear equation for χ is reached such that it provides a "regularized version of $\chi_{csi}^{(n)}$" [15, equation 4.76]:

$$\chi(\mathbf{r}) - \left[F_S(\mathbf{w})\frac{1}{V}\int_{\mathbf{r}\in D}\left|\chi_{csi}^{(n)}(\mathbf{r})\right|^2 dV\right](\Delta x)^2\nabla\cdot\left[b^{(n)}(\mathbf{r})\nabla\chi(\mathbf{r})\right] = \chi_{csi}^{(n)}(\mathbf{r}) \tag{3.37}$$

Note, the influence of the weighted Laplacian term $(\nabla\cdot\left[b^{(n)}(\mathbf{r})\nabla\chi(\mathbf{r})\right])$ is controlled by the data cost and the mean of the LS-solution contrast.

To find this regularized contrast function the equation 3.37 is represented as a linear system of equations (LSoE) by applying discretization to the object domain D and denoting it as Ω. P pixels of the locations $\mathbf{x} \in \Omega$ are arranged in a rectangular grid of size N_1 by N_2 such that it enables gradient and divergence operations of equation 3.37 to be replaced with finite difference approximations. The linear system of equations is represented using the vector quantities $\chi, \chi_{csi} \in \mathbb{C}^{P\times 1}$

$$A\chi = \chi_{csi}^{(n)}, \tag{3.38}$$

where $A \in \mathbb{R}^{P\times P}$ represents the Laplacian finite difference operations for the $P = N_1 N_2$ contrast values of equation 3.37.

A Jacobi iteration is used based on the regular splitting $A = D + R$ to solve this system of equations for χ. The idea behind this is to confirm that A is strongly or irreducibly diagonally dominant and consequently the Jacobi iteration converges. Matrices D and R respectively represent the diagonal and off-diagonal elements arising from the weighted Laplacian partial differential equation (PDE). Forward and backward finite difference approximations in the directions x_1 and x_2, denoted as $\Delta_{1,2}$ and $\nabla_{1,2}$ seen on the left hand side in equations 3.39, are used to approximate the PDE because a central finite difference approximation would not take into account the jumps in contrast that may occur in the center points[15], e.g. contrast jumps from position $x_{i+1,j}$ to position $x_{i,j}$.

$$\begin{aligned}
\Delta_1\chi(x_{i,j}) &= \chi(x_{i+1,j}) - \chi(x_{i,j}) \\
\Delta_2\chi(x_{i,j}) &= \chi(x_{i,j+1}) - \chi(x_{i,j}) \\
\nabla_1\chi(x_{i,j}) &= \chi(x_{i,j}) - \chi(x_{i-1,j}) \\
\nabla_2\chi(x_{i,j}) &= \chi(x_{i,j}) - \chi(x_{i,j-1}),
\end{aligned} \tag{3.39}$$

The contrast gradient term is now expressed as:

$$(\Delta x)^2 \left|\nabla\chi\left(x_{i,j}\right)\right|^2 = \frac{1}{2}\left(\left|\Delta_1\chi\left(x_{i,j}\right)\right|^2 + \left|\Delta_2\chi\left(x_{i,j}\right)\right|^2 + \left|\nabla_1\chi\left(x_{i,j}\right)\right|^2 + \left|\nabla_2\chi\left(x_{i,j}\right)\right|^2\right), \quad (3.40)$$

which is used in the expression for the weights $b^{(n)}$ of equation 3.32.

Finally, the calculation of weighted Laplacian term of equation 3.37 is presented:

$$\begin{aligned}(\Delta x)^2\nabla\cdot\left[b^{(n)}\nabla\chi\left(x_{i,j}\right)\right] = &\frac{1}{2}\left\{\Delta_1\left[b^{(n)}\left(x_{i,j}\right)\nabla_1\chi\left(x_{i,j}\right)\right] + \Delta_2\left[b^{(n)}\left(x_{i,j}\right)\nabla_2\chi\left(x_{i,j}\right)\right]\right\}\\ &+\frac{1}{2}\left\{\nabla_1\left[b^{(n)}\left(x_{i,j}\right)\Delta_1\chi\left(x_{i,j}\right)\right] + \nabla_2\left[b^{(n)}\left(x_{i,j}\right)\Delta_2\chi\left(x_{i,j}\right)\right]\right\},\end{aligned} \quad (3.41)$$

which can be fully expressed

$$\begin{aligned}(\Delta x)^2\nabla\cdot\left[b^{(n)}\nabla\chi\left(x_{i,j}\right)\right] = &-\frac{1}{2}\left[b^{(n)}\left(x_{i+1,j}\right) + 2b^{(n)}\left(x_{i,j}\right) + b^{(n)}\left(x_{i,j+1}\right)\right.\\ &\left.+b^{(n)}\left(x_{i-1,j}\right) + 2b^{(n)}\left(x_{i,j}\right) + b^{(n)}\left(x_{i,j-1}\right)\right]\chi\left(x_{i,j}\right)\\ &+\frac{1}{2}\left[b^{(n)}\left(x_{i+1,j}\right) + b^{(n)}\left(x_{i,j}\right)\right]\chi\left(x_{i+1,j}\right)\\ &+\frac{1}{2}\left[b^{(n)}\left(x_{i-1,j}\right) + b^{(n)}\left(x_{i,j}\right)\right]\chi\left(x_{i-1,j}\right)\\ &+\frac{1}{2}\left[b^{(n)}\left(x_{i,j+1}\right) + b^{(n)}\left(x_{i,j}\right)\right]\chi\left(x_{i,j+1}\right)\\ &+\frac{1}{2}\left[b^{(n)}\left(x_{i,j-1}\right) + b^{(n)}\left(x_{i,j}\right)\right]\chi\left(x_{i,j-1}\right),\end{aligned} \quad (3.42)$$

where the first term on the right-hand side is the diagonal element of A and the other four are the off-diagonal elements.

Hence the LSoE for a particular point $x_{i,j}$ in the grid with $i \in 1,2,\ldots,N_1$ and $j \in 1,2,\ldots,N_2$ becomes

$$(D+R)\chi\left(x_{i,j}\right) = \chi_{csi}^{(n)}\left(x_{i,j}\right), \quad (3.43)$$

where the relevant elements of the matrix-vector-product $A\chi$ for the particular point are as follows using a backward and forward finite differences gradient implementation:

$$\begin{aligned}D\chi\left(x_{i,j}\right) = 1 + &\frac{1}{2}F_S(\mathbf{w})\,\mathrm{mean}\left(\left|\chi_{csi}^{(n)}\right|^2\right)\\ &\times\left[b^{(n)}\left(x_{i+1,j}\right) + 2b^{(n)}\left(x_{i,j}\right) + b^{(n)}\left(x_{i,j+1}\right)\right.\\ &\left.+b^{(n)}\left(x_{i-1,j}\right) + 2b^{(n)}\left(x_{i,j}\right) + b^{(n)}\left(x_{i,j-1}\right)\right]\chi\left(x_{i,j}\right)\end{aligned} \quad (3.44)$$

and

$$\begin{aligned}R\chi\left(x_{i,j}\right) = &-\frac{1}{2}F_S(\mathbf{w})\,\mathrm{mean}\left(\left|\chi_{csi}^{(n)}\right|^2\right)\\ &\times\left\{\left[b^{(n)}\left(x_{i+1,j}\right) + b^{(n)}\left(x_{i,j}\right)\right]\chi\left(x_{i+1,j}\right)\right.\\ &+\left[b^{(n)}\left(x_{i-1,j}\right) + b^{(n)}\left(x_{i,j}\right)\right]\chi\left(x_{i-1,j}\right)\\ &+\left[b^{(n)}\left(x_{i,j+1}\right) + b^{(n)}\left(x_{i,j}\right)\right]\chi\left(x_{i,j+1}\right)\\ &\left.+\left[b^{(n)}\left(x_{i,j-1}\right) + b^{(n)}\left(x_{i,j}\right)\right]\chi\left(x_{i,j-1}\right)\right\}.\end{aligned} \quad (3.45)$$

Note how any row of A contains at most five non-zero values, one from the diagonal matrix and four from the off-diagonals due to the neighbouring points of $x_{i,j}$. This is characteristic to the implementation of the 2-point finite difference approximation.

JACOBI METHOD AND CONVERGENCE

The regular splitting of A is of the form $A = D - (-R)$ with D non-singular and both $(-R)$ and the inverse of D non-negative. As such, the updating rule for the Jacobi iteration of a general LSoE $A\mathbf{y} = \mathbf{b}$ is described using the iteration matrix $G = D^{-1}(-R)$ [47, Chapter 4]:

$$\mathbf{y}_{k+1} = G\mathbf{y}_k + D^{-1}\mathbf{b}, \tag{3.46}$$

wherein the k'th iteration vectorized quantity of the tissue contrast function is $\mathbf{y_k} = \chi_k$ and $\mathbf{b} = \chi_{csi}$. In addition, the best initial guess available is $\chi_0 = \chi_{csi}$ and for brevity $\mathbf{f} = D^{-1}\mathbf{b}$ moving forward.

In order to verify the validity of using (multiple) Jacobi iterations we set out to proof that applying G an amount k times to any starting vector $\mathbf{f}$ and initial guess χ_{csi} converges the error between each successive χ_k to zero:

$$\chi_{k+1} - \chi_k = G^k(\mathbf{f} - (I - G)\chi_0) \tag{3.47}$$

The requirements for guaranteed convergence of Jacobi (and Gauss-Seidel) iterations retrieved from such a regular splitting contains the following points[47, Chapter 4]:

Requirements 1

- D, (-R) is a regular splitting of A, i.e. $A = D - (-R)$ with D non-singular and both $(-R)$ and the inverse of D non-negative
- A is either strongly diag. dominant or irreducibly diag. dominant → proving non-singularity of A (through Gershgorin's theorem of disc contained eigenvalues [47])
- A is either positive monomial (for all elements of A the statement: $a_{ij} \geq 0$ is true) and therefore A^{-1} is non-negative

A secondary set of requirements can be found using the spectral radius:

Requirements 2

- D, (-R) is a regular splitting of A, i.e. $A = D - (-R)$ with D non-singular and both $(-R)$ and the inverse of D non-negative
- For a square matrix G with spectral radius $\rho(G) < 1$, $I - G$ is non-singular and the Jacobi iteration converges[47, Chapter 4]. Because the spectral radius of G $\rho(G)$ satisfies $\rho(G) \leq \|G\|$ for any matrix-norm of G, either the 1- or ∞-norm (absolute column and row norms) of G can be evaluated and it can be verified that the upper bound on the spectral norm $\|G\| < 1$ exists

This second set is most general to proof and so these points are discussed in detail. The proof starts with touching on the parameters in each of the elements of D and $(-R)$ and the regular splitting is verified. Finally it is shown that the spectral radius of G is bounded between 0 and 1.

The matrices D and R contain the non-zero positive factor $\alpha = F_S(\mathbf{w})\,\text{mean}\left(\left|\chi_{csi}^{(n)}\right|^2\right)$. Additionally, it is noted that each row p of R represents the FD relations of the particular point $x_{i,j}$ with its neighbouring four points and that the row contains the same Laplacian weights present in the corresponding diagonal element in D, this sum factor is:

$$\begin{aligned}\beta(p) = &\left[b^{(n)}\left(x_{i+1,j}\right) + b^{(n)}\left(x_{i,j}\right)\right] + \left[b^{(n)}\left(x_{i-1,j}\right) + b^{(n)}\left(x_{i,j}\right)\right] \\ &+ \left[b^{(n)}\left(x_{i,j+1}\right) + b^{(n)}\left(x_{i,j}\right)\right] + \left[b^{(n)}\left(x_{i,j-1}\right) + b^{(n)}\left(x_{i,j}\right)\right],\end{aligned} \tag{3.48}$$

and all these Laplacian weights are positive when choosing the regularization parameter $\delta^{(n)}$ positive.

3

SPECTRAL STABILITY ANALYSIS

Returning to the discretization of the 2D object domain Ω, the matrix $D \in \mathbb{R}^{P\times P}$ is a diagonal matrix of non-zero entries

$$d_{pp} = 1 + \frac{\alpha}{2}\beta(p) \tag{3.49}$$

Its determinant, as the product of these diagonal entries, is non-zero and therefore D is non-singular. The inverse of D thus exists and is also non-negative due to the inverse diagonal form: $D^{-1} = \text{diag}(1/d_{11}, 1/d_{22}, ..., 1/d_{PP})$ for all $p = 1, 2, ..., P$.

Matrix $(-R)$ is also non-negative: each row of the $P \times P$ matrix $(-R)$ contains the four non-zero values that are a product of the positive values $\frac{\alpha}{2}$ and now one of the terms in $\beta(p)$.

Therefore $(D, -R)$ is thus a regular splitting of A and an upper bound on the spectral radius of G is to be found using any matrix norm to prove convergence regardless of $\mathbf{f}$ and χ_0. The matrix ∞-norm is used since this reduces the calculation of the bound to finding the maximum row 1-norm of G. The p'th row and m'th column element of G is denoted as $[G]_{p,m}$ where $p, m = 1, 2, ..., P$.

$$\|G\|_\infty = \max_p \sum_{m=1}^{P} |[G]_{p,m}| = \max_p \sum_{m=1}^{P} \left|\left[D^{-1}(-R)\right]_{p,m}\right| = \max_p d_{pp}^{-1} \sum_{m=1}^{P} [-R]_{p,m} \tag{3.50}$$

where it is seen that each row of (-R) is scaled by the corresponding D^{-1} element and the absolute notation can be dropped due to non-negativity of D and (-R). Now using that the sum of the elements in row p of (-R) is the same as equation 3.48 (up to a scaling with $\alpha/2$), it can be substituted and the matrix norm of G is found from

$$\|G\|_\infty = \max_p \left[1 + \frac{\alpha}{2}\beta(p)\right]^{-1} \frac{\alpha}{2}\beta(p). \tag{3.51}$$

Now noting that the result of equation 3.51 has the form $\frac{z}{1+z}$ and evaluating it with limits for z on the interval $[0, \infty)$:

$$\begin{gathered}\lim_{z\to 0} \frac{z}{1+z} < \|G\|_\infty < \lim_{z\to\infty} \frac{z}{1+z} \\ 0 < \|G\|_\infty < 1\end{gathered} \tag{3.52}$$

the resulting absolute row norm has upper bound 1. Therefore the spectral radius of G satisfies $\rho(G) < 1$ and the Jacobi iteration converges for the discretized screened Laplacian PDE of equation 3.37. Furthermore, due to non-negativity of the problem ($\beta(p) > 0$ and $\alpha > 0$) z is positive non-zero and therefore $\rho(G) > 0$. Finally, the result means that for any iteration, the specified regular splitting (D, -R) confirms that A is non-singular and its inverse non-negative [47, Theorem 4.4].

Therefore the Jacobi-step regularization can feature any number of inner-iterations to perform the regularization using any initial estimate $\mathbf{x}_0$ while converging to a final form of the first-order regularized contrast at that outer-iteration. To start the regularized update in the vicinity of a contrast that is considered as optimal as is known the initial estimate is the LS-solution contrast, i.e. $\mathbf{x}_0 = \chi_{csi}^{(n)}$. A single Jacobi iteration regularized contrast $\chi^{(n)}$ for iteration n is thus achieved using

$$\chi^{(n)} = D^{-1}\left(\chi_{csi}^{(n)} - R\chi_{csi}^{(n)}\right) \tag{3.53}$$

STRENGTH OF THE REGULARIZATION

The global asymptotic convergence factor $\phi_c = \lim_{k\to\infty} \left\|G^k\right\|^{\frac{1}{k}} = \rho(G)$ is bounded by the same limits seen in inequality 3.52. The lower the convergence rate the stronger the total variation regularization for that outer-iteration n in the sense that each Jacobi iteration produces a contrast function which is (geometrically) further away from the initial LS-solution $\chi_{csi}^{(n)}$:

$$\begin{aligned}\left\|\chi_K - \chi_{csi}^{(n)}\right\| &= \left\|\chi_K - \chi_{K-1} + \chi_{K-1} - \chi_{K-2} + \ldots + \chi_1 - \chi_{csi}^{(n)}\right\| \\ &= \left\|(G^{K-1} + G^{K-2} + \ldots + G + I)(G + D^{-1} - I)\chi_{csi}^{(n)}\right\|\end{aligned} \tag{3.54}$$

where the difference between each Jacobi iteration result is found using equation 3.47 and the initial estimate $\mathbf{f} = D^{-1}\chi_{csi}$.

The factors α and β in equation 3.51 thus regulate the strength of the regularization through iteration matrix G as well as the number of inner-iterations K. Embedded in first two factors are the data cost $F_s(\mathbf{w}^{(n)})$, mean intensity of $\chi_{csi}^{(n)}$ and the regularization parameter $\delta^{(n)}$.

Other solution methods

The Gauss-Seidel method (GS) is also valid using a similar matrix splitting to find a regularized version of equation 3.37. After some initial testing it was concluded that the dependence of neighbouring pixels was too large, thereby strong contrasts were smeared across the entire object domain. Thereby GS is deemed not suitable for this problem in addition to the unfavourable sequential computation needed for GS, which is slow when compared to the Jacobi's parallel computation. Successive-over-Relaxation (SOR) and its variants are reliant on a similar algorithm as Gauss-Seidel. Therefore these methods were also disregarded.

Other methods suitable for solving the linear system of equations of equation 3.38 consist of other finite difference methods for sparse linear systems such as: poisson fast solver, sparse direct solution, descent algorithms (other than the CG) and Krylov subspace methods. Furthermore, implementation based on Finite Element Methods and

spectral methods may be suitable for solving the more general regularization equation 3.37 or higher order approximations of the non-linear Euler-Lagrange equation 3.36.

3.5.2. JACOBI STEP CSI-EPT

Regularization of the least squares contrast can thus also be performed by a Jacobi iteration instead of a conjugate gradient step (CG). Consequently, the two-step updating process of CSI-EPT then features two differently-natured updating rules, one CG and one Jacobi iteration based. To summarize, the Jacobi-step contrast updating for CSI-EPT involves reformulation of the original weighted-integral TV multiplicative regularization term (equation 3.25) into a weighted Laplacian PDE (equation 3.37). Each outer-iteration of the Jacobi-step CSI-EPT performs finite difference approximation of the PDE by applying one or more Jacobi iterations (i.e. inner-iterations).

The following is a listing summarizing the Jacobi-step CSI-EPT algorithm. The only difference compared to basic CSI-EPT is the updating of the contrast in Update 2.

- Determine the incident EM fields $\hat{\mathbf{E}}^{inc}$ and $\hat{\mathbf{B}}_1^{+;inc}$ and provide $\hat{\mathbf{B}}_1^{+;sca}$
- Determine the initial contrast source $\mathbf{w}^{(0)}$ (see Section 3.4) and from it the contrast $\chi^{(0)}$
- **Initial forward calculation**: calculate the resulting EM fields with the appropriate object and data operators:

  $$\tilde{B}_1^{+;sca} = \mathsf{G}_S^+\{\mathbf{w}^{(0)}\}$$

  and

  $$\tilde{\mathbf{E}} = \hat{\mathbf{E}}^{inc} + \mathsf{G}_D\{\mathbf{w}^{(0)}\}$$

- For each outer-iteration n perform these steps until a convergence criterion has been met or the maximum number of iterations is reached:

  1. **Update 1**: Update the contrast source while fixing the contrast function $\chi^{(n-1)}$:

     $$\mathbf{w}^{(n)} = \mathbf{w}^{(n-1)} + \alpha^{(n)}\mathbf{v}^{(n)}$$

     with a gradient step of the total cost function $F(\mathbf{w}^{(n-1)}, \chi^{(n-1)})$.
  2. **Forward calculation**: Recalculate the estimation $\tilde{B}_1^{+;sca}$ and $\tilde{\mathbf{E}}$ fields with the newly obtained contrast source.
  3. **Update 2**: Calculate the intermediary CSI contrast function $\chi_{csi}^{(n)}$ from $\left\| \chi^{(n)}\tilde{\mathbf{E}} - \mathbf{w}^{(n)} \right\|_D^2$ and perform K inner-iterations by applying the Jacobi-step contrast update based on the linear PDE approximation $(D+R)\chi^{(n)} = \chi_{csi}^{(n)}$:

     $$\chi_K^{(n)} = D^{-1}\left(\chi_{K-1}^{(n)} - R\chi_{K-1}^{(n)}\right),$$

     with $\chi_0^{(n)} = \chi_{csi}^{(n)}$.

4. **Update costs**: Update the source and object cost as in the basic CSI-EPT and use

$$F_R^{(n)}(\chi_K^{(n)}) = \frac{1}{V}\int_{\mathbf{x}\in\Omega} \frac{|\nabla\chi_K^{(n)}(\mathbf{x})|^2 + \delta^{(n)}}{|\nabla\chi^{(n-1)}(\mathbf{x})|^2 + \delta^{(n)}} dV(\mathbf{x}),$$

to update the multiplicative regularization cost. Finally, update the total cost function: $F(\mathbf{w}^{(n)}, \chi_K^{(n)}) = (F_D + F_S)\, F_R$

3.5.3. TV DELTA PARAMETER

The $\delta^{(n)}$ regularization parameter was originally required for differentiability [22], but also regulates influence of the regularization factor and is originally chosen to increase this influence as the iteration number increases [45]. As the $\delta^{(n)}$ term decreases, the weight of the total variation of the contrast function (i.e. the ratio of gradient terms) increases within the regularization factor. A naturally decreasing term in the CSI method is the object error term and thus the original regularization parameter is a product of the objective functional and the reciprocal of the mesh size Δ (resulting from discretization of the imaging domain Ω) [22]:

$$\delta^{(n)} = F_{D,n}\Delta^2, \tag{3.55}$$

with $\Delta^2 = 1/(d_x d_y)$ using the mesh sizes d_x and d_y.
With the use of the object and data objectives on the object domain Ω the known regularization parameters are:

- Chosen to decrease in value and named "Berg-Abubakar" as presented in [22]

$$\delta_{BA}^{(n)} = F_{D,n}\Delta^2 \tag{3.56}$$

- Experimentally found yet unpublished: "Remis"

$$\delta_{Remis}^{(n)} = \frac{F_{S,n}}{F_{D,n}}\Delta^2 \tag{3.57}$$

- "Haffinger" regularization parameter was presented in the doctoral thesis [48, Section 2.3.3.] as the mean of the variation of $\left|\nabla\chi^{(n-1)}\right|^2$

$$\delta_{Haff}^{(n)} = \frac{1}{V}\int_{\mathbf{x}\in\Omega} |\nabla\chi(\mathbf{x})|^2 dV = \frac{1}{N_\Omega}\sum_i \left(|\nabla\chi(\mathbf{x}_i)|^2\right), \tag{3.58}$$

wherein N_Ω is the number of pixels in the masking that covers the object domain and $\mathbf{x}_i$ denotes the i'th 2D location inside that mask.

4

METHODS AND IMPLEMENTATION

This chapter serves to explain the implementation of methods that put the contributions of Section 1.2 into full context. This is done along the lines of the considerations and choices that were presented in Chapter 3.

Despite the primary focus of this thesis being the application and performance of the Jacobi step regularization, the algorithmic order of CSI-EPT as presented in the previous chapter is followed. Therefore, this chapter starts by presenting the simulation of the field data, be it full or transceive fields. Thereafter, Section 4.2 elaborates on the CT and MRI-based contrast initialization method. Finally, the specific implementations of the two multiplicative regularization versions are described in Section 4.3. Other CSI-EPT related parameters are mentioned when relevant at the results (Chapter 5). The simulations, mappings and algorithm execution is all performed using Matlab (version 2022b).

4.1. EM FIELDS SIMULATION

The following sections are dedicated to the simulation of the EM data. The simulation of all incident and scattered EM fields is elaborated first and adapted for calculation of the receive fields for the Transceive Phase Correction CSI-EPT later in this section. The simulations start with one of the various 2D contrast objects which are to be reconstructed. The field simulation implementations are explained along the lines of incident fields, RF shielding influence, scattered field operators and the addition of noise to the field data.

4.1.1. CONTRAST OBJECTS

Various 2D objects were used to simulate illumination of a patient with EM fields to act as the experimentation transmit field data and generate the complementary EM fields. For most experiments the Ella model from the Virtual Family published by the IT'IS foundation [49] was used. It is modeled to be anatomically representative of a 26 year old female in terms of tissue values. In this thesis the conductivity and relative permittivity mapping data are used to generate a contrast mapping of a 2D transverse slice of the Ella model. From this model three different axial slices were picked to perform reconstruction with.

First, the pelvis model was picked for its ease of reference to to the article using the same region [14], wherein the CG updating step is evaluated. The pelvis model additionally features different levels of detail in the 2D tissue profile as seen in Figures 4.1 and 4.2.

MRI is suitable for imaging the soft tissue differences in the brain. This makes the brain region a prevalent subject for MRI research and is therefore also added to the regions to evaluate EP reconstruction on.

In the abdomen slice the contrast object is convoluted by asymmetry. Especially in the transceive phase field case this invalidates the Transceive Phase Assumption further [33], [34]. Therefore, the abdomen region is the third slice from the Ella model to be used in the reconstructions. The conductivity and relative permittivity profiles of the three slices are shown in the Figures 4.1 - 4.6.

All contrast objects are discretized using a square meshing grid with mesh size 2.5 mm. Discretization of the imaging domain Ω makes the norm and convolution integrals into summations over the P different pixels. Here $P = NM$ refers to the discretization in N rows and M columns. A binary mask which denotes the pixels inside the actual virtual object is applied to simulate the true reception domain of an MRI, i.e. the air surrounding the object or body does not transmit a signal and is excluded from such a mask.

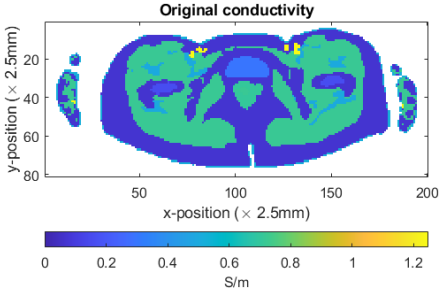

Figure 4.1: Original conductivity profile of slice 168 in the Ella Virtual Family model.

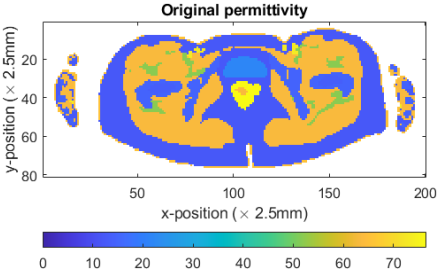

Figure 4.2: Original relative permittivity profile of slice 168 in the Ella Virtual Family model.

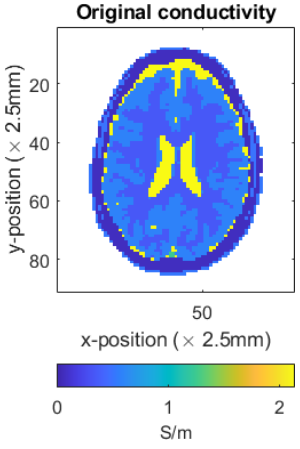

Figure 4.3: Original conductivity profile of head model (slice 319) of the Ella Virtual Family model.

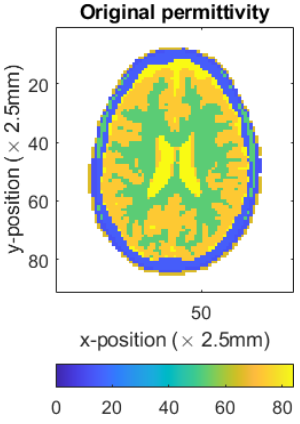

Figure 4.4: Original relative permittivity profile of head model (slice 319) of the Ella Virtual Family model.

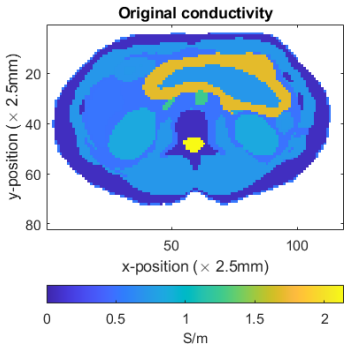

Figure 4.5: Original conductivity profile of abdomen model (slice 216) of the Ella Virtual Family model.

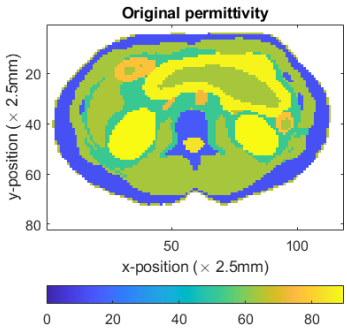

Figure 4.6: Original relative permittivity profile of abdomen model (slice 216) of the Ella Virtual Family model.

4

4.1.2. INCIDENT ELECTRIC FIELDS

The incident fields in the discretized imaging domain Ω are simulated by a summation of the individual fields from 16 line sources. These are oriented in the longitudinal direction and extend into infinity such that they only propagate longitudinally-oriented incident electric fields. The sources are located uniformly at a radial distance R as is shown in the Figure 4.7 by the red dots. In the results R is 0.352 m. The radiated fields from the line sources at $\mathbf{y_i}$ into the positions $\mathbf{x} \in \Omega$ are summed to achieve the incident electric field:

$$E_z^{inc}(\mathbf{x}) = \sum_{i=1}^{16} -p(\theta_i)\frac{\omega\mu_0}{4} H_0^{(2)}(k_0|\mathbf{x}-\mathbf{y_i}|), \tag{4.1}$$

wherein $|\mathbf{x}-\mathbf{y_i}|$ is the Euclidean distance and $p(\theta_i)$ is a factor which determines the current density of line source number i at the time of transmission. Employing a sinusoidal current density factor like

$$p(\theta_i) = cos(\theta_i) \qquad \theta_i = (i-1)\frac{2\pi}{16}$$

simulates linear excitations, while the complex exponential factor $\exp(j\theta_i)$ simulates quadrature excitation.

In similar fashion, the contributions from each of the line sources to the initial transmit fields at position $\mathbf{x}$ is summed:

$$\hat{\mathbf{B}}_1^{sca}(\mathbf{x}) = \sum_{i=1}^{16} p(\theta_i)\frac{\omega}{2c_0^2}\left(\partial_x + j\partial_y\right) G_T(\mathbf{x}-\mathbf{y}_i) J^{ext}(\mathbf{y}_i) \tag{4.2}$$

Implementation of the RF shielding is done with the 16 mirror sources such that the shield is at distance $R_s = 0.3715\ m$. The mirror sources shown in Figure 4.7 (in blue) carry the same current density as their red line source counterpart but with opposite sign. At the dotted line a net-zero electric field is the result. The field contributions of these RF line sources are also added to form the shielded incident EM fields.

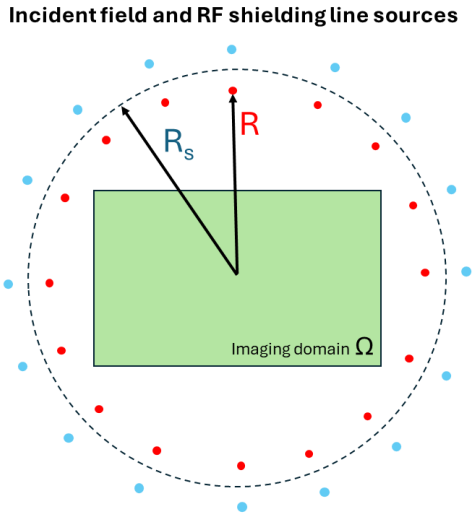

Figure 4.7: Transversal view of the line sources configurations that transmit the longitudinal electric fields (red) and simulate the RF shield (the dotted circle) at a radius R_s by transmitting an opposing current (blue line sources).

4.1.3. SCATTERED EM FIELDS

For simulating the scattered electric fields the ground truth contrast, object operators and incident electric field are employed inside a Generalized Minimum Residual (GMRES) scheme to retrieve the total electric fields. GMRES is an iterative projection based method [47]. It is used for simulation of the total electric field E_z as its vectorized equivalent $\mathbf{e}$ is found from

$$\begin{aligned} E_z - \mathsf{G}_D\{\chi E_z\} &= E_z^{inc} \\ \mathscr{D}\mathbf{e} &= \mathbf{e}^{inc} \end{aligned} \tag{4.3}$$

The resulting contrast sources, i.e. the product χE_z, are then used to simulate the scattered magnetic fields with the data operators G_S^+ and its receive field equivalent G_S^- (for TPC CSI-EPT). In general the data and object operators used to update the scattered magnetic fields are implemented with spatially-relative Green's functions and the use of the Fast Fourier Transform. These are detailed next.

FOURIER OPERATORS AND THE WEAK GREENS FUNCTION

The forward field calculations are performed using the Fast Fourier Transform (FFT) and, due to the discretization of the Ω, the scattered EM field operators require the use of the Weak Green's function.

Throughout the CSI-EPT algorithms, the FFT is employed to find the inherent convolutions of contrast sources and (derivatives of) the Greens functions, i.e. the operators are implemented as:

$$\mathsf{G}_D\{\mathbf{w}\} = \mathrm{FFT}^{-1}\left\{\mathrm{FFT}\{g_E(\mathbf{x}-\mathbf{x}')\}\cdot\mathrm{FFT}\{\mathbf{w}(\mathbf{x}')\}\right\}, \qquad \mathbf{x},\mathbf{x}' \in \Omega \tag{4.4}$$

$$\mathsf{G}_S^+\{\mathbf{w}\} = \frac{1}{\omega}\,\mathrm{FFT}^{-1}\left\{\mathrm{FFT}\{g^+(\mathbf{x}-\mathbf{x}')\}\cdot\mathrm{FFT}\{\mathbf{w}(\mathbf{x}')\}\right\}, \qquad \mathbf{x},\mathbf{x}'\in\Omega \tag{4.5}$$

wherein the g_E and g^+ functions are contractions of the wave-related constants, the derivatives and the Green's function for the scattered electric field and transmit fields, respectively. Note that the Green's functions are implemented using relative distances $\mathbf{x}-\mathbf{x}'$ which warrants use of the FFT. This would not be the case when the RF shielding or coil loading effects are also taken into account into the construction of the Green's functions. Spatial-invariance is then lost [33].

A weakened form of the Green's function is required for the implementation of the transverse Green's function (equation 3.3) in a discretized domain. Otherwise poles at $G_T(\mathbf{0})$ invalidate differentiation. The 2D weak Green's function $G_w(\mathbf{x})$ is described in [50] and is of the form:

$$G_w(\mathbf{x}) = \frac{-j}{2k_0 a}J_1(k_0 a)H_0^{(2)}(k_0|\mathbf{x}|) \tag{4.6}$$

wherein J_1 is the Bessel function of the first kind, a half the mesh size and k_0 the free-space wavenumber.

Using the Weak Greens function and longitudinal E fields designated in the E-polarized field case, the 2D scattered electric field and transverse magnetic field operators are repeated as they were introduced in Section 3.2.1:

$$\mathsf{G}_D\{\mathbf{w}\}(\mathbf{x}) = k_0^2\int_{\mathbf{x}'\in\Omega} G_w(\mathbf{x}-\mathbf{x}')\mathbf{w}(\mathbf{x}')\,dV \tag{4.7}$$

$$\mathsf{G}_S^+\{\mathbf{w}\}(\mathbf{x}) = \frac{\omega}{2c_0^2}\left(\partial_x + j\partial_y\right)\hat{A}_z(\mathbf{x}) = \frac{\omega}{c_0^2}\partial^+\int_{\mathbf{x}'\in\Omega} G_w(\mathbf{x}-\mathbf{x}')\mathbf{w}(\mathbf{x}')\,dV \tag{4.8}$$

The partial derivatives used to define the g^+ involve the first order Hankel function $H_1^{(2)}(u)$ and the vector distance $\mathbf{r}=\mathbf{x}-\mathbf{x}'\in\mathbb{R}^2$ between location $\mathbf{x}$ and a particular contrast source at $\mathbf{x}'$:

$$\begin{aligned}
\partial_x H_0^{(2)}(k_0|\mathbf{r}|) &= \frac{\partial(k_0|\mathbf{r}|)}{\partial_x}\frac{\partial H_0^{(2)}(k_0|\mathbf{r}|)}{\partial(k_0|\mathbf{r}|)} \\
&= \frac{2k_0 r_x}{2\sqrt{r_x^2+r_y^2}}H_{-1}^{(2)}(k_0|\mathbf{r}|) \qquad \left(\text{using } \frac{d}{dx}H_0^{(2)}(u) = \frac{du}{dx}H_{-1}^{(2)}(u)\right) \\
&= -\frac{k_0 r_x}{|\mathbf{r}|}H_1^{(2)}(k_0|\mathbf{r}|) \qquad \left(\text{simplifying } H_{-1}^{(2)}(u) = -H_1^{(2)}(u)\right)
\end{aligned} \tag{4.9}$$

Using this result and the similar partial derivative w.r.t. the distances in the y-direction in the Greens term, one arrives at the Wirtinger partial derivative defining the propagation

of the transverse receive fields:

$$\begin{aligned} g^+ &= k_0^2 \partial^+ G_w(\mathbf{x}-\mathbf{x}') \\ &= \frac{k_0^2}{2}\left[\frac{-j}{2k_0 a} J_1(k_0 a)\right]\left[\partial_x H_0^{(2)}(k_0|\mathbf{r}|) + j\partial_y H_0^{(2)}(k_0|\mathbf{r}|)\right] \\ &= \frac{k_0^2}{2}\left[j\frac{k_0 r_x}{2k_0 a|\mathbf{r}|} J_1(k_0 a) H_1^{(2)}(k_0|\mathbf{r}|) + j^2 \frac{k_0 r_y}{2k_0 a|\mathbf{r}|} J_1(k_0 a) H_1^{(2)}(k_0|\mathbf{r}|)\right] \\ &= k_0^2 \frac{(r_x + j r_y)}{2}\left[\frac{j}{2a|\mathbf{r}|} J_1(k_0 a) H_1^{(2)}(k_0|\mathbf{r}|)\right] \end{aligned} \tag{4.10}$$

4.1.4. MEASURED FIELD NOISE

Implementation of noise is done similarly to [29], where it is described how separate amplitude and phase noise must be applied due to the nature of acquiring transmit field amplitude and phase data separately. The final resulting MRI SNR factor that can be expected was simulated and reported in [51] to be approximately 55 ($\approx 36dB$) at main field strength of $3T$. Moving forward the SNR or noise levels are expressed in decibels (dB). To test noise robustness or to compare to similar EPT methods the noise levels used are either 30, 40 or 50 dB.

The superimposed noise models for the amplitude and phase noise are only applied on the $\hat{B}_1^+$ transmit field data. The additive noise of the amplitude and phase are Gaussian distributed with zero mean and variance of $m_{|B|}$ and var($\angle B$) normalized by the chosen noise level, respectively, wherein $m_{|B|}$ is the median amplitude value of the generated transmit field and var($\angle B$) the variance of the transmit field complex phase.

4.2. IMAGING-BASED CONTRAST INITIALIZATION

The default contrast source initialization is the backpropagation presented in Equation 3.23. Unless mentioned otherwise, backpropagation is the initialization method used in this thesis. In the transceive field data case, this method requires adjustment to compensate the lack of transmit phase knowledge. Therefore, before the measured transceive field is used in the adjoint data operator, it is multiplied with a complex exponential containing an initial receive phase guess. For this the TPA is used due to its simplicity.

The remaining two initialization strategies are anatomical prior information based and EPT based. Numerical results in the past were said to exhibit counterintuitive reconstruction behaviour when initialized with methods other than back propagation. Hence in order to test robustness and in the ambition of finding further reconstruction improvements from the initial experiments concerning the Jacobi-step regularization ; investigating these other initialization methods was deemed interesting as secondary experiments to the alternative MR CSI-EPT algorithm.

IMAGING MODALITY RESCALING

The biophysical and structural information that numerous imaging modalities can provide is well-documented. Due to the authors theoretical familiarity with CT and MRI, initialization based on these imaging modalities was developed. The motivation for testing this initialization strategy is twofold: investigate whether the structural a priori infor-

mation is beneficial to reconstruction times and determine what artifacts (if any) are introduced due to the multiplicative regularization types.

The idea behind the imaging modality rescaling (IMR) method is to (hand)pick tissue regions, e.g. bone, that are known to be prominent in either CT imaging or MRI and rescale the Virtual Family contrast values to reflect the same prominence as the original imaging modality. This rescaled contrast profile is then used as the initialization of the contrast sources using the initially simulated E-fields. After all, in CT one can find good contrast between bone structures and soft tissue, hence it is deemed interesting to introduce such structural a priori information to the CSI-EPT algorithm.

Available were the EPs of the virtual family model at each slice. The admittance at $3T$ MRI images is dominated by the conductivity, which is the reason for the subsequent discrimination of tissue regions based on the conductivity and prominance in the appropriate imaging modality. These regions were grouped according to the conductivity thresholds shown in Table 4.1 and the regions are shown in Figure 4.8.

Tissue type	conductivity σ [S/m]	σ in CT	σ in MRI
blood vessels	1.249	0.05	1.2
rectum	0.705214 - 0.719235	0.1	0.5
muscle tissue (muscle; tendons)	0.719235; 0.498727	0.3	0.45; 0.7
skin	0.522704	0.15	0.15
bladder	0.298014	0.05	1
femoral bone and cartillage	0.0673524 - 0.162021	1	0.1
pectineal and pubic bones	0.0673524	1	0.1
other (fat, distal skin layers, etc.)	0.0697299	0.2	0.25

Table 4.1: Anatomical regions and their conductivity values in the Ella pelvis model, the CT and MRI modality profiles have adjusted conductivity according to arbitrary assignment.

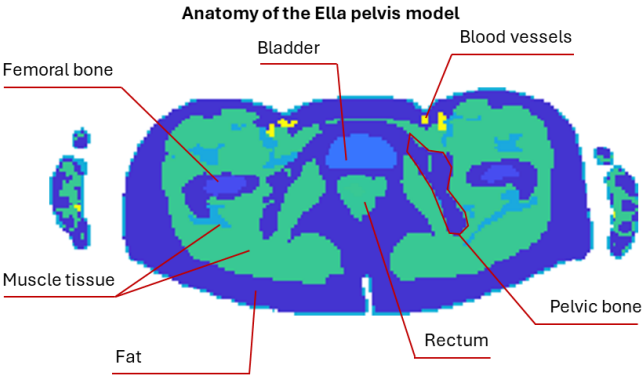

Figure 4.8: The division of anatomical regions in the conductivity profile of the pelvis model

The latter two columns in Table 4.1 show the new conductivity initialization values for the CT and MRI based initialization profiles. Note that these values have been assigned based on the author's understanding of the respective imaging modalities. Addi-

tionally, for the goals of the experiment the use of anatomically accurate rescaling values is not crucial. The prominance of bone in CT imaging is highlighted in the table with borders and similarly the good contrast in soft tissue is highlighted in the MRI column.

After rescaling the conductivity, it is assumed that the relative permittivity has mostly the same structure as the conductivity yet higher absolute value at the $128MHz$ frequency of $3T$ imaging. Therefore the average ratio of relative permittivity and conductivity is taken from the original pelvis region and applied to the rescaled CT and MRI conductivity values. This average ratio is 99.71 for the EPs of the pelvis region shown in Figures 4.1 and 4.2. The initial conductivity profiles become as is shown in Figure 4.9. Imperfect structural information can also be tested by entering an offset slice just above or below the intended slice. The resulting four anatomical prior initializations are depicted in the appendix Figures B.8 - B.11.

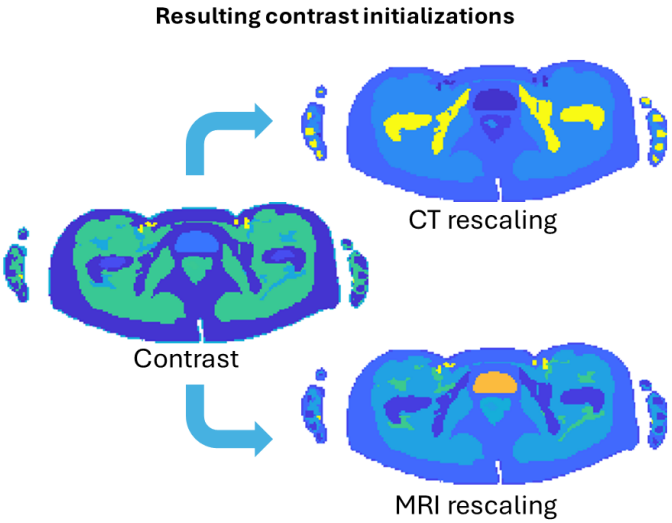

Figure 4.9: Applying the imaging modality rescaling to the original conductivity profile (on the left) to obtain the CT-based and MRI-based conductivity profiles (on the right).

4.3. MULTIPLICATIVE TV REGULARIZATION

The mix of forward and backward finite differences is part of the implementation to achieve a PDE solvable with the Jacobi regular splitting method. The following paragraphs describe further choices in the implementation of the Jacobi-step regularization. In addition motivation and experiments for choice of regularization parameter and the testing of multiple Jacobi inner-iterations are elaborated in this section.

The Conjugate Gradient (CG) and Jacobi-step total variation multiplicative regularizations (TVMR) are to be compared in terms of visual quality and post-reconstruction noise. The starting point to both regularized contrast updating steps is the least-squares update from contrast sources to a contrast profile as in equation 3.27. The implementa-

tion of the CG contrast updating step is as documented in [22, Section 3].

4.3.1. IMPLEMENTATION OF JACOBI-STEP

The implementation of the Jacobi-step update does not require large sparse matrices as was presented in the previous Chapter. The D and R matrices are calculated using the equations 3.44 and 3.45 for each of the N × M points in the pelvis region. The Jacobi-step is then applied according to Equation 3.53.

The original book section [15, Section 4.6] mentions to use a $\max\{F_s, 0.01\}$ function to maintain the effect of the regularization, even when F_s is small, instead of simple weighting of the Laplacian with the F_s value. However, use of such a function was regarded arbitrary. Therefore, in favour of eliminating as much arbitrary parameters from the total regularized reconstruction, in this thesis the F_s value weighting, as seen in equations 3.44 and 3.45, is reinstated. There are adverse effects to using the maximum function in more complicated structures as shown in Figure 4.10. Maintaining a high TV strength causes the loss of detail in the reconstruction as can best be seen in the over-smoothing of the blood vessels.

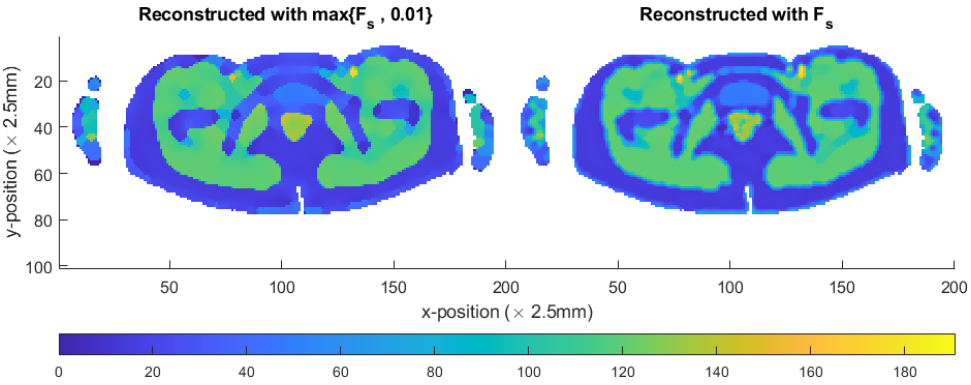

Figure 4.10: Demonstration of the adverse effects of using the arbitrary max function using two reconstructions (absolute value of contrast function $|\chi|$) both at 50 SNRdB noise level and 500 iterations.

4.3.2. REGULARIZATION PARAMETER STUDY

Though there are different $\delta^{(n)}$ functions possible, there was no prior indication which performs best under which conditions. The goal is to find what impacts the regularization parameter choice has on the final reconstruction in terms of the visual image similarity to the original, using the SSIM metric, and in terms of the residual noise, which is measurable with a mean-square-error metric such as the RRE.

The Structural Similarity Index (SSIM) is a metric developed to measure image quality based on the degradation of structures in a processed image and the original [52]. The metric scores a 1 when comparing two pictures with exact similarity but a -1 when comparing a processed image with reversed contrasts of the original. The three main components of SSIM are image contrast, luminance and structure, which are based on the mean image intensity and standard deviation. The components can be weighted

with exponents to emphasize importance but in this thesis that was not done. Hence the SSIM value of an original conductivity profile **x** and a reconstructed profile **y** is calculated as [52]

$$\mathrm{SSIM}(\mathbf{x},\mathbf{y}) = \frac{(2\mu_x\mu_y + C_1)(2\sigma_{xy} + C_2)}{(\mu_x^2 + \mu_y^2 + C_1)(\sigma_x^2 + \sigma_y^2 + C_2)} \qquad -1 \leq \mathrm{SSIM}(\mathbf{x},\mathbf{y}) \leq 1, \tag{4.11}$$

wherein μ and σ are the mean and standard deviations and C_1 and C_2 constants (proportional to the image dynamic range) that prevent instability for zero-mean or zero-variance signals.

The relative residual error (RRE) metric is and error-based metric. The square of the error with the original image pixel value is normalized with the absolute of the same pixel value. The sum of these individual RRE values is then summed into the final result. The RRE is used separately on the conductivity and relative permittivity parts of the reconstructed contrast[39]:

$$\mathrm{RRE} = \sqrt{\frac{\sum_{i=1}^{N} |y_i - x_i|^2}{\sum_{i=1}^{N} |x_i|^2}}, \tag{4.12}$$

with **x** the original conductivity (or relative permittivity) profile and **y** the reconstructed conductivity.

4.3.3. MULTIPLE JACOBI STEP

Throughout initial testing of the Jacobi-step contrast update it was noted that increasing the number of inner-iterations K increases the strength with which the total variation regularization is applied in each outer-iteration. Strong regularization thus refers to a high cost from the regularization cost function relative to the object and data cost functions.

The regularization strength ρ_{TV} of a particular Jacobi step regularized solution χ_K is expressed using the norm distance that the regularized solution has "travelled away" from the initial guess $\chi_{csi}^{(n)}$:

$$\rho_{TV}(\chi_K) = \frac{\left\| \chi_K - \chi_{csi}^{(n)} \right\|}{\left\| \chi_{csi}^{(n)} \right\|}, \tag{4.13}$$

wherein $\left\| \chi_K - \chi_{csi}^{(n)} \right\|$ is as described in equation 3.54. Through initial experimentation it was found that a too strong regularization erases all detail in favour of producing a few piece-wise constant contrast regions, while a weak regularization is unable to effectively remove noise. This is further elaborated in Section 5.2.1.

Two methods were thought of to take advantage of this increase in regularization strength:

1. Increasing inner-iterations may require less outer-iterations for similar performance

2. Varying the number of inner-iterations may lead to improved performance

The first point could increase reconstruction speed due to a lowered number of calculations performed in total. Especially gradient calculations and algorithmic extensions into 3D or high fidelity implementations of the Green's functions are computational bottlenecks that are then reduced. Such expensive calculation could be spared by decreasing the number of outer-iterations yet increasing the number of inner-iterations. This type of Jacobi-step CSI-EPT is referred to as static-K.

The idea to vary K throughout the different outer-iterations came from observing relatively fast convergence (within 100 outer-iterations) to reconstructions with a strong edge-preservation characteristic when using multiple Jacobi-steps ($K \geq 3$). Similar to the one exhibited on the left in Figure 4.10, these reconstructions were thought to serve as fast and easy to achieve structural priors for the later stages of the reconstruction process to refine. Hence potentially increasing the reconstruction performance. This type of Jacobi-step CSI-EPT is referred to as dynamic-K.

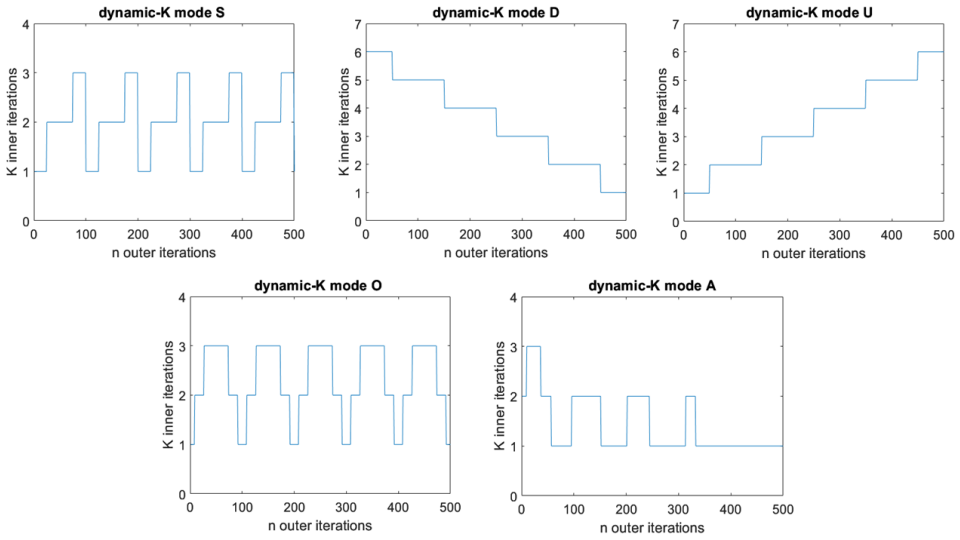

Figure 4.11: The dynamic-K modes shown with a period $T = L/5$ for the maximum outer-iterations $L = 500$ as described in Section 4.3.3.

Different modes have been tested. To test the frequency with which the inner-iterations could be varied the period of change is defined based on the maximum number of outer-iterations L: $T = L/2, L/5, L/10, L/25$. In other words, the period parameter determines how quickly a high number of inner-iterations follows an outer-iteration with a low number of inner-iterations.

The functions used to define these modes are shown below and are rounded to create an integer number of K inner-iterations for the outer-iteration n. The shapes of the resulting dynamic-K modes at period $T = L/5$ is show in the Figure 4.11. It must be noted that the introduction and implementation of such modes however introduces the

arbitrary regularization parameter being the period T.

$$\text{Upscaling (mode U)}: \quad K(n) = 1 + \frac{n}{T}$$

$$\text{Downscaling (mode D)}: \quad K(n) = (1 + \frac{L}{T}) - \frac{n}{T}$$

$$\text{Oscillating (mode O)}: \quad K(n) = 1 + |2\sin(\frac{n\pi}{T})|$$

$$\text{Sawtooth (mode S)}: \quad K(n) = 1 + \frac{2\,\mathrm{mod}(n,T)}{T}$$

$$\text{Damped oscillation (mode A)}: \quad K(n) = 1 + \exp\left(\frac{-2n}{L}\right)\left(1 + \sin(\frac{2n\pi}{T})\right)$$

5

NUMERICAL SIMULATION RESULTS

The hypotheses of interest are mostly related to the performance of the alternative Jacobi step multiplicative regularization in comparison with the Conjugate Gradient variant. The outline of this chapter follows the rationale of adding more algorithmic components in the form of field excitations and RF shielding. In the first Section 5.1, the Jacobi step regularization performance is observed by varying the reconstruction regions, noise level and regularization parameter. Adding multiple inner-iterations to the Jacobi step CSI-EPT is discussed later, as well as applying the anatomical *a priori* initialization. These presented are presented in Section 5.2.

The pelvis electrical properties profiles have been presented in Section 4.1. However, the majority of the results will be presenting the contrast functions instead, for which the ground truth (of the pelvis model) is seen in Figure 5.1. The line profiles that occasionally present a 1D view of the reconstructed EPs are taken from line 41 as highlighted by the red dotted line.

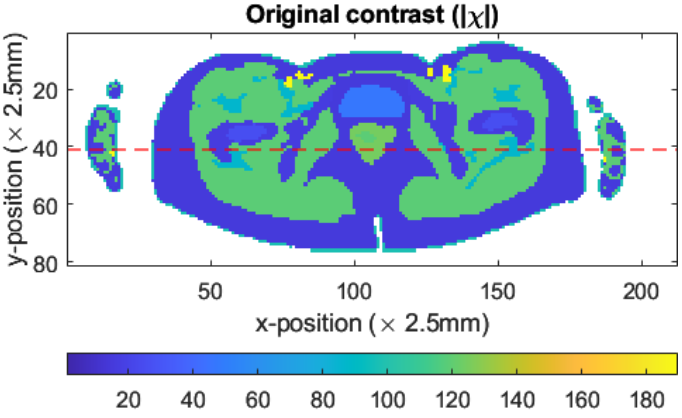

Figure 5.1: Contrast profile (in absolute value) of slice 168 in the Ella Virtual Family model. The red striped line denotes the location of the line profiles for the pelvis (line 41).

All reconstructions were performed using a 2GHz Intel Core i7–8565U CPU, 8GB RAM and Matlab version 2022b. On average the reconstruction times per 100 iterations of Ja-

cobi step reconstructions for the abdomen, pelvis and head models were respectively 7.06, 21.43 and 24.57 seconds. The same regions reconstructed with the conjugate gradient regularization took 6.70, 20.76 and 24.52 seconds per 100 iterations.

5.1. SINGLE JACOBI STEP UPDATING

In first instance, the reconstructions are made without RF shielding affecting the incident fields and with the default regularization parameter being the 'Berg-Abubakar' regularization parameter. For this section the initialization is back-propagation. Unless mentioned otherwise, the reconstructions are made using 500 iterations. Final results have shown that extending the reconstructions past this point did not yield additional significant results while quality improvement has generally slowed.

The following sections present general qualities of the single Jacobi step regularized CSI-EPT reconstruction. Influences of applying multiple EM field excitations, the RF shielding, transmit field noise level and the regularization parameter are analyzed.

MULTIPLE EM FIELD EXCITATIONS

Figure 5.2 shows that increasing the amount of EM excitations and using regularization are both beneficial to the reconstruction due to noise reduction. The weak electric field on the diagonal of the imaging domain creates artefacts in the reconstructions based on only a single quadrature or linear excitation similar to the 2D reconstructions in Balidemaj et al. [14, Figures 4(a), (b)]. There is less information available in these regions to accurately reconstruct the electrical properties [14] and so the reconstruction is prone to noise in these areas.

Furthermore, it is noted that the Jacobi step CSI-EPT reconstruction has improved noise reduction and edge preservation characteristics compared to the unregularized and CG regularized reconstructions. There are clearly flat regions of invariant contrast in the muscle and skin layers of the Jacobi reconstructions, whereas these regions are still noisy in the unregularized and even in the CG regularized reconstructions. The same conclusions are drawn from the line profile comparisons in Figures 5.3 and 5.4.

Throughout the rest of this chapter reconstructions presented are made with the 3 different excitations, i.e. quadrature, horizontally linear and vertically linear excitation.

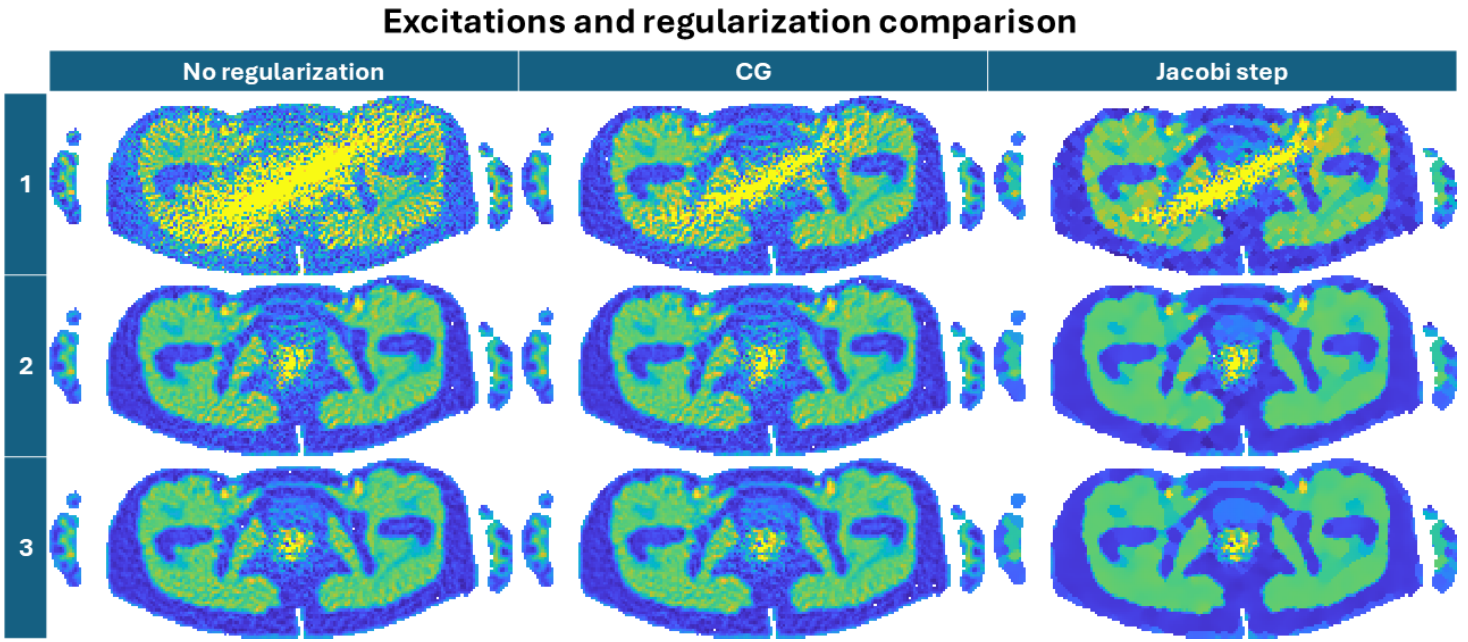

Figure 5.2: Reconstructions from 1, 2 or 3 different EM field excitations made with no regularization, Conjugate Gradient regularization and Jacobi step regularization. All 9 reconstructions were terminated at 500 iterations and produced using an input noise level of 40 dB SNR.

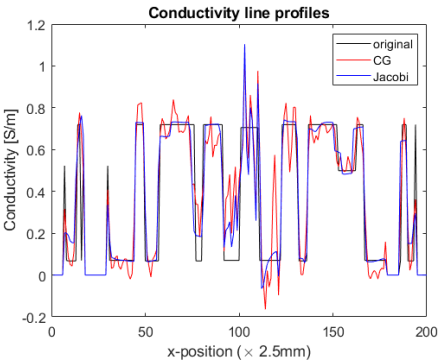

Figure 5.3: Conductivity profile as reconstructed by CG and Jacobi step CSI-EPT using 3 EM field excitations and compared to the original profile.

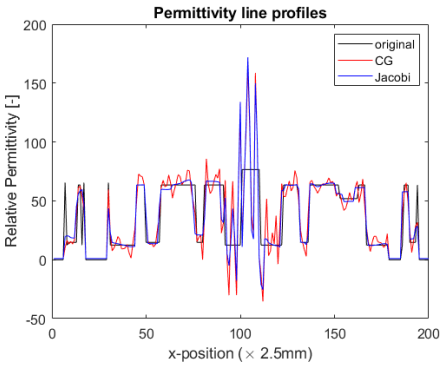

Figure 5.4: Permittivity profile as reconstructed by CG and Jacobi step CSI-EPT using 3 EM field excitations and compared to the original profile.

5

RF SHIELDING

The RF shielding influence on the pelvis reconstructions is shown in Figure 5.5. Initially no changes are noticed when compared to the unshielded reconstruction in Figure 5.6. However, after comparing the RRE and SSIM metrics for all three reconstruction regions in Table 5.1, a reconstruction quality improvement is observed when implementing the RF shielding using the mirror sources. Judging from the 9.59% and 11.27% decrease in RRE there is less residual noise left in the reconstructions due to the introduction of the RF shielding. In addition, incorporation of the RF shielding benefits the reconstruction of the relative permittivity as seen by the change in that particular SSIM metric.

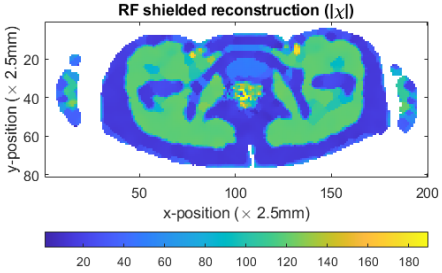

Figure 5.5: Reconstruction of the pelvis when using the incident fields originating from a shielded MRI setup.

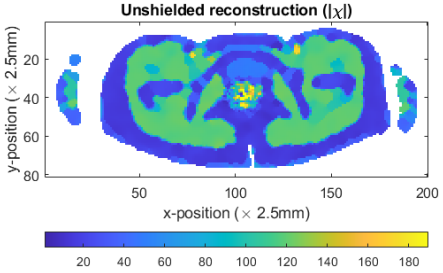

Figure 5.6: Reconstruction of the pelvis without RF shielded MRI setup.

However, when the two reconstructions are compared using line profiles as presented in Figures 5.7 (a) and (b), it is seen that the differences between the two reconstructions, shielded and unshielded, resides mainly in the center of the contrast profile (see the red line). Since this is generally the most noisy part of the reconstructions due to the consequence of the 2D formulation of the E-polarized assumption, this perceived improvement in quality remains to be proven for three-dimensional implementation of the RF shielded single Jacobi step regularization.

Reconstruction	Shield	RRE σ	RRE ε	SSIM $\lvert\chi\rvert$	SSIM σ	SSIM ε
Pelvis	on	0.2470	0.2843	0.5029	0.8300	0.4870
	off	0.2732	0.3204	0.4581	0.7874	0.4502
	% change	**-9.59**	**-11.27**	**9.78**	**5.41**	**8.17**
Head	on	0.3719	0.2537	0.2771	0.6828	0.2797
	off	0.3832	0.2779	0.2682	0.6742	0.2640
	% change	**-2.94**	**-8.71**	**3.32**	**1.28**	**5.95**
Abdomen	on	0.1649	0.2425	0.3642	0.9233	0.2895
	off	0.1880	0.2806	0.3343	0.8990	0.2715
	% change	**-12.29**	**-13.58**	**8.94**	**2.70**	**6.63**

Table 5.1: The effect of shielding on the reconstruction is observed in the improved metrics across all reconstruction regions for the 40 dB noise level; the relative residual errors are 3 to 14% lower while the SSIM improved with 1 to 10%.

NOISE INFLUENCE

The improved noise-robustness for the pelvis model is again exhibited in Figure 5.8. At an increased input noise level of 30 dB the conjugate gradient reconstruction is heavily corrupted by noise, while the Jacobi step counterpart produces a crude yet less noise afflicted reconstruction.

At 40 and 50 dB input SNR the quality of both regularized reconstructions improve, but the Jacobi step CSI-EPT remains better at producing noise-free reconstructions. Reconstruction of the center is tough at all noise levels; the center remains corrupted by noise due to the small electric field strength. A similar analysis applies to the abdomen region reconstructions as is presented in Appendix B.5.

When comparing the reconstructions of the head model in Figure 5.9 reveals a different pattern however. The CG CSI-EPT arguably acquires a reconstruction of the head model more faithfully than the Jacobi-step reconstruction does, despite the usual and significant residual noise error in the former. Looking at Figure 5.9, the Jacobi step version applies a stronger TV regularization; the different Jacobi step reconstructions at the different noise levels feature piecewise constant regions but at the cost of details.

The difficulty in this particular reconstruction for the Jacobi step CSI-EPT may lay in the increased contrast amplitude of the ground truth model (see the increased scale at the bottom of Figure 5.9). Consequently, the mean value of the LS contrast χ_{csi} is higher than in the pelvis and abdomen models which results in a larger contribution from the weighted Laplacian term in the original linearized regularization equation 3.37. Therefore, this increase TV regularization strength in combination with the finite difference dependencies of the Jacobi regularization and insufficient resolution of the discretization lead to the lack of detail in the reconstruction. The separation of white and grey matter in the brain is only discernible in the CG reconstruction at 50dB SNR.

The RRE and SSIM of the various reconstructions and noise levels are presented in Table 5.2. The conductivity is better reconstructed across all regions and noise levels than the permittivity. This is expected to be caused by the amount of information that is available from a large contrast or admittance. At $3T$ MRI fields the conductivity portion of the admittance is higher than that of the relative permittivity. Hence error in conduc-

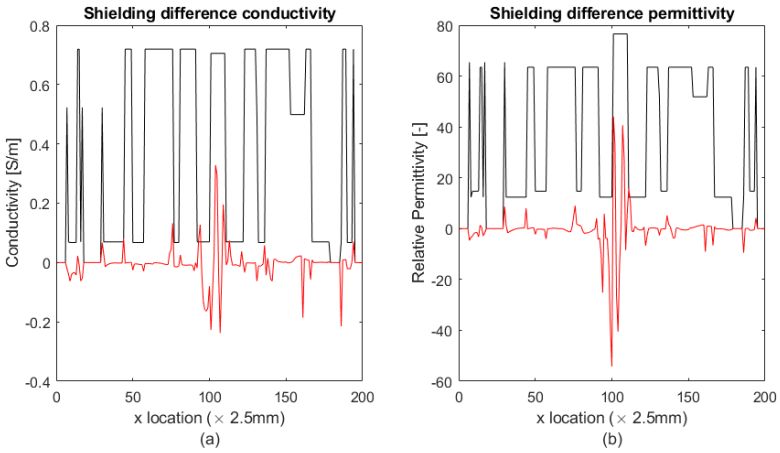

Figure 5.7: Differences in reconstructed EP's with and without shielding (red lines) and the original conductivity and relative permittivity profile (black lines). Reconstructions of the pelvis made with 40 dB SNR transmit field noise and 500 outer-iterations.

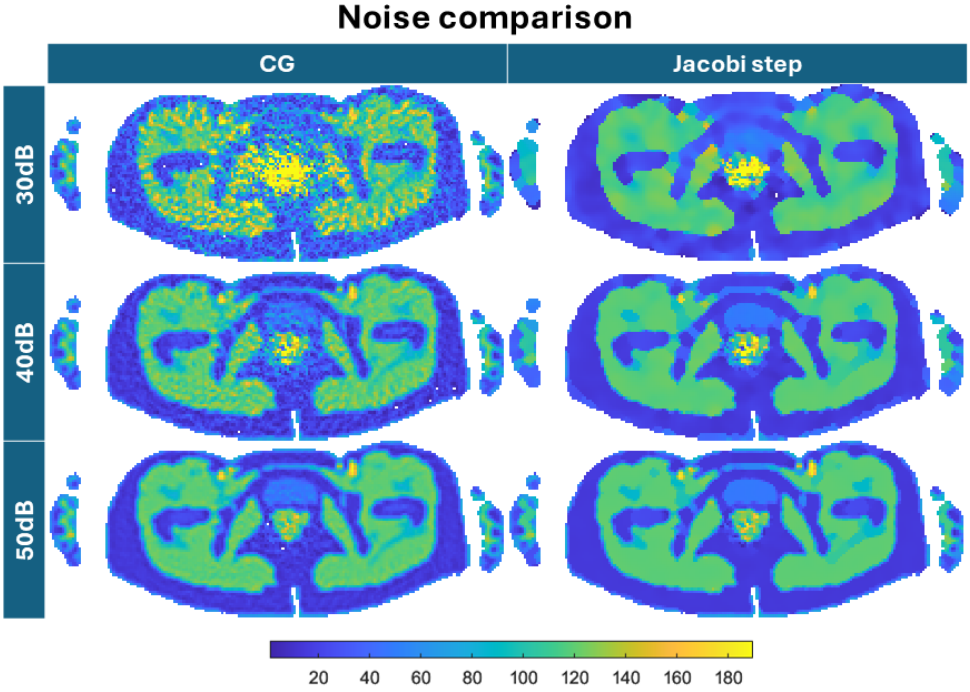

Figure 5.8: Input transmit field noise of different levels affects the reconstruction quality in the comparison between the two multiplicative regularized CSI-EPT algorithms. Using 500 outer-iterations and the Berg-Abubakar regularization parameter.

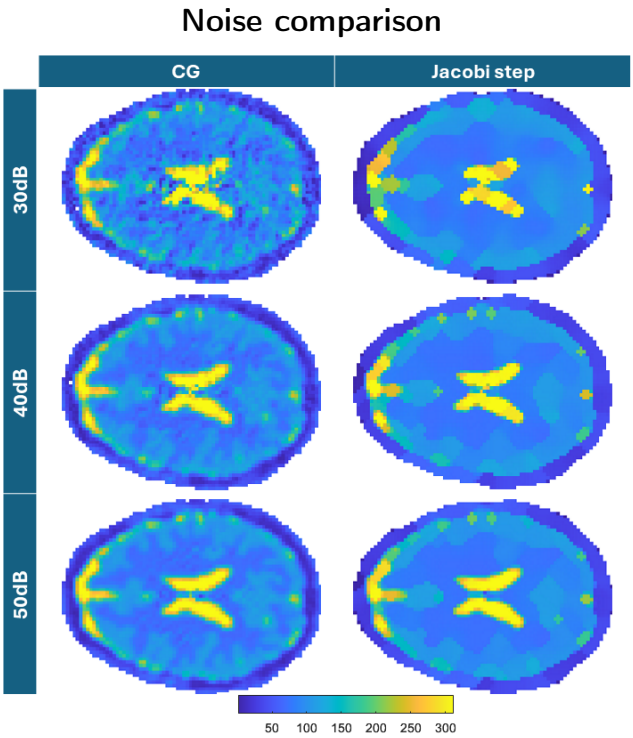

Figure 5.9: Noise comparison of head model reconstructions using 500 outer-iterations and the Berg-Abubakar regularization parameter.

tivity reconstruction is more costly to the total cost function than similar size errors in the relative permittivity reconstructed values.

The RRE values achieved are compared to the three dimensional reconstructions of a similar Virtual Family model named Duke in [39] (7T main magnetic field, quadrature driven head-sized birdcage coil with SNR factor 50 $\approx 34dB$ SNR). The black lines in Figure 4b of the article presents RRE values for the conductivity profiles between 0.5 and 0.6 and approximately 0.4 for the relative permittivity profiles at 1000 iterations for the CG regularized reconstruction using the Haffinger parameter. The RRE values of the Jacobi step reconstructed conductivity and relative permittivity profiles are lower than those values which is highlighted in bold in the Table 5.2 at approximately 0.4 and 0.3 RRE for conductivity and permittivity respectively.

REGULARIZATION PARAMETER

In order to understand the influence of the TV regularization parameter $\delta^{(n)}$, the different options of Section 3.5.3 were used to reconstruct the pelvis at different noise levels. In Figure 5.10 these reconstructions are presented. The reconstructions of the pelvis model at 40 and 50 dB SNR in the left and right columns, respectively, while the rows depict reconstructions using the Berg-Abubakar, Haffinger and Remis regularization parameter $\delta^{(n)}$.

Reconstruction	Noise level [dB]	RRE σ	RRE ε	SSIM $\lvert\chi\rvert$	SSIM σ	SSIM ε
Pelvis	30	0.3868	0.5035	0.3779	0.7077	0.3714
	40	0.2470	0.2843	0.5029	0.8300	0.4870
	50	0.2157	0.2237	0.5455	0.8710	0.5240
Head	30	**0.4123**	**0.2920**	0.2381	0.6413	0.2401
	40	**0.3719**	**0.2771**	0.2682	0.6828	0.2797
	50	0.3647	0.2406	0.2916	0.6974	0.3036
Abdomen	30	0.2588	0.3858	0.2842	0.8522	0.2409
	40	0.1649	0.2425	0.3642	0.9233	0.2895
	50	0.1483	0.2081	0.3838	0.9391	0.3160

Table 5.2: Metrics from the single Jacobi step reconstructions at different noise levels produced from 500 outer-iterations, Berg-Abubakar regularization parameter and RF shielded incident field simulation.

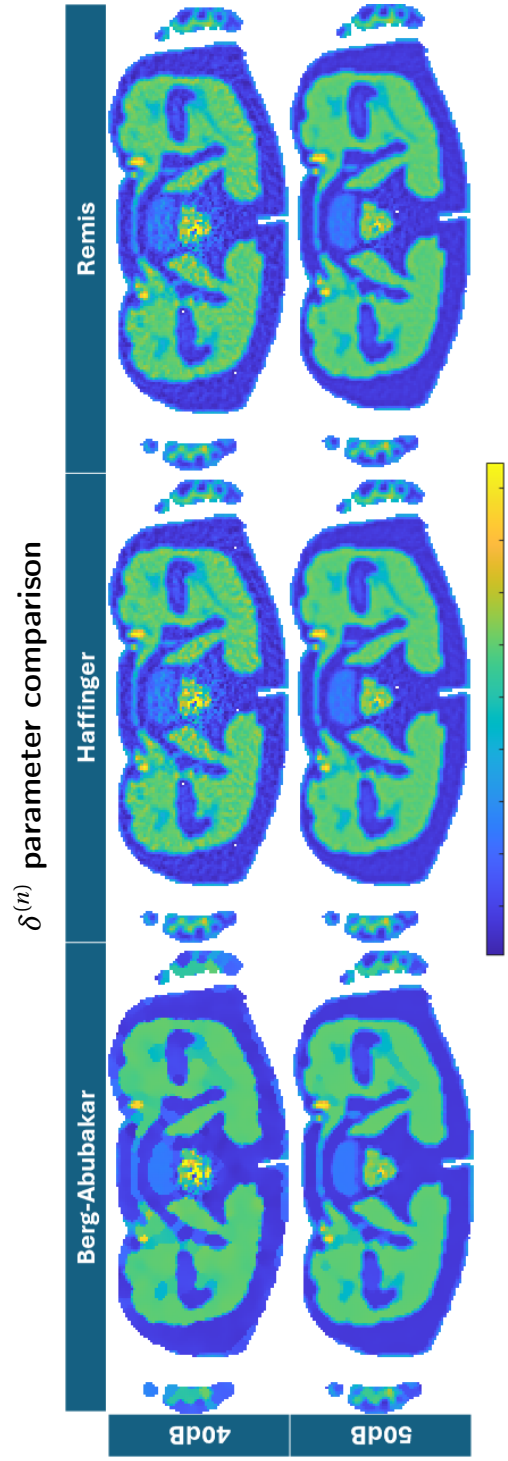

Figure 5.10: Different Jacobi step reconstructions obtained using the 'Berg-Abubakar', 'Haffinger' and 'Remis' $\delta^{(n)}$ regularization parameters during reconstruction of the pelvis model with 40dB SNR noise and 50dB.

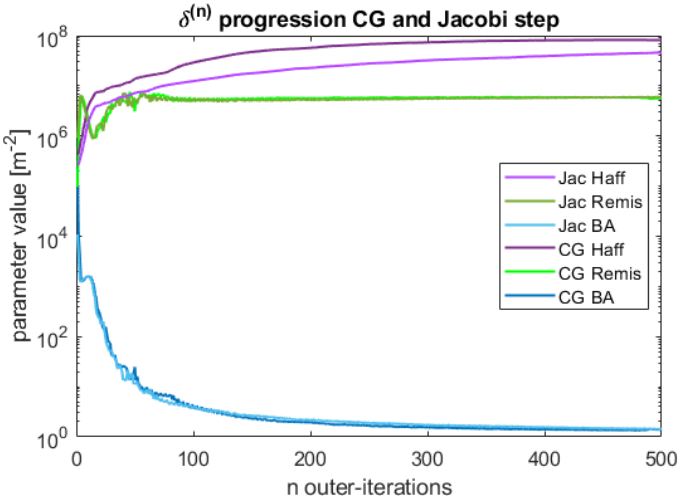

Figure 5.11: Progression of the different regularization parameter $\delta^{(n)}$ settings 'Berg-Abubakar' (BA, blue), 'Haffinger' (Haff, purple) and 'Remis' (green) during reconstruction of the pelvis model with 40dB SNR.

Notably, the improved edge-preserving and noise reduction characteristics that were observed earlier are no longer observed when using the Haffinger and Remis regularization parameters. By visualizing the progression of these parameter values throughout the reconstructions a pattern emerged that is presented in Figure 5.11. During reconstruction the BA parameter is several orders of magnitude smaller than the other two regardless of the multiplicative regularization type.

When the regularization parameter is small the gradient and Laplacian terms[1] gain influence in the respective CG and Jacobi step regularization, thus increasing the regularization strength that is applied to the reconstruction.

Applying the Haffinger or Remis regularization parameter to the Jacobi step CSI-EPT head model reconstruction, a similar reconstruction is retrieved as the CG reconstructions in Figure 5.9 at 40 dB SNR. The regularized reconstructions of the head and abdomen using the different regularization parameters are seen in the appendix Figure B.3 and B.4. Table 5.3 shows that the Haffinger and Remis reconstructions of the head are better in quality than using the stronger TV regularization from the Berg-Abubakar parameter for Jacobi CSI-EPT. Hence it shows the Jacobi step regularization can perform similar to the CG regularization in situations when the higher regularization strength is excessive for the head model.

5.2. ADDITIONAL CSI-EPT VARIANTS

From the multiple Jacobi step CSI-EPT the static inner-iterations variant is evaluated first. The reconstruction quality is to be compared with the single Jacobi version in order to conclude whether reconstruction speed-up occurs or not. Hereafter, in Section 5.2.1, the amount of inner-iterations is varied throughout the reconstruction in an attempt to

[1] See equation 3.25 for the CG gradient terms and equation 3.32 for the Laplacian weights of the Jacobi step.

Reconstruction	$\delta^{(n)}$	RRE σ	RRE ε	SSIM $\lvert\chi\rvert$	SSIM σ	SSIM ε
Head CG	Berg-Abubakar	0.3275	0.2310	0.4374	0.8388	0.3814
	Haffinger	0.3363	0.2680	0.4337	0.8355	0.3797
	Remis	0.3325	0.2352	0.4324	0.8344	0.3837
Head Jacobi	Berg-Abubakar	0.3719	0.2771	0.2682	0.6828	0.2797
	Haffinger	0.3318	0.2770	0.4336	0.8357	0.3889
	Remis	0.3286	0.2292	0.4378	0.8392	0.3879

Table 5.3: The RRE and SSIM metrics are improved when using the Haffinger and Remis $\delta^{(n)}$ parameters on the head model. Results from $40dB$ SNR and 500 outer-iterations Jacobi and CG reconstruction.

improve reconstruction quality by the hypothetical principle of repeatedly applying a crude structural prior. Finally, the anatomical prior initialization is evaluated in Section 5.2.2.

5.2.1. MULTIPLE ITERATION JACOBI REGULARIZATION

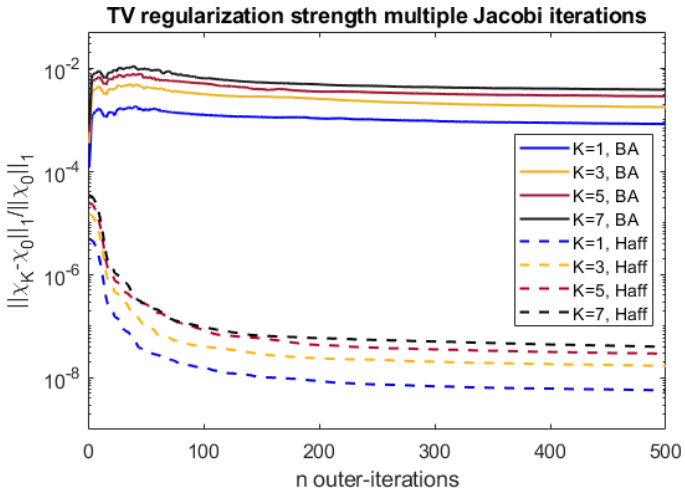

Figure 5.12: TV strength ρ_{TV} shown throughout Jacobi step reconstructions of the pelvis with the Berg-Abubakar and Haffinger $\delta^{(n)}$ parameters.

Introducing multiple Jacobi inner-iterations increases the TV regularization strength that is applied as can be seen in the Figure 5.12. The distance between the regularized χ_K and unregularized χ_0 contrasts (see Section 4.3.3) is plotted for each outer-iteration during the reconstruction of the pelvis at 40dB SNR. The higher the amount of inner-iterations the more the TV regularization is applied. In addition Figure 5.12 also shows again that the Haffinger $\delta^{(n)}$ enacts lower regularization strength.

It is hypothesized that such increase in regularization can improve the reconstruction performance in either reconstruction time or visual quality by utilizing multiple Jacobi iterations. Either a static increase or preset pattern of increased and lowered amount of inner-iteration Jacobi steps is applied to achieve this and the results are de-

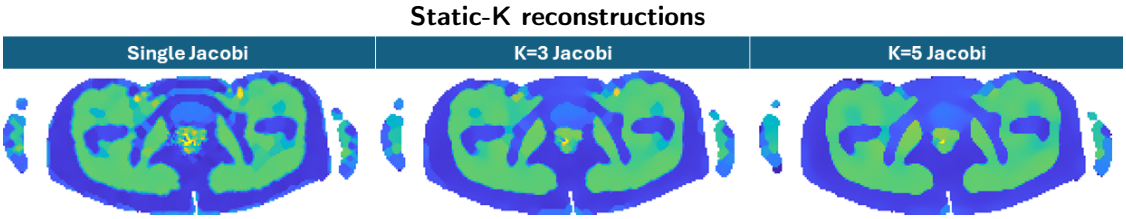

Figure 5.13: Pelvis reconstructions using one, three and five Jacobi iterations for performing the regularization at 40dB noise level and 500 outer-iterations.

scribed in the following two sections.

STATIC-K JACOBI

Figure 5.13 presents the reconstructions from applying either a single, three or five Jacobi steps as the regularized contrast update. The increased TV strength is clearly reducing the amount of detail in fine structures such as the blood vessels and lower contrast muscle tissue at the final reconstruction iteration (500 outer-iterations).

From Figures 5.14, 5.15 and 5.16 it is noted that the static increase in inner-iterations also does not result in early structural quality improvements over the single Jacobi regularization.

DYNAMIC-K JACOBI

With the knowledge that high inner-iteration counts reduce reconstruction detail certain dynamic-K modes presented in Section 4.3.3 were expected to show similar low detail reconstructions due to ending the reconstruction process on a high number of inner-iterations. These are the Upscaling and Sawtooth modes. However, the resulting reconstructions in Figure 5.17 show that the dynamic-K modes produce similar reconstructions as the original single Jacobi reconstruction (highlighted in the box top left). Still there is loss of detail in most of these reconstructions, mostly around the bladder area where the faint muscle and bladder tissues seem merged with the surrounding tissues.

At 30dB again the reconstructions become more crude and lose details. Figures 5.18 and 5.19 present the RRE throughout the reconstruction process of the pelvis model at 30dB SNR. The figures show that it can be beneficial to the reconstruction to limit the reconstruction process to approximately 200 iterations. Reconstructions that result from early-stopping at 200 outer-iterations are seen in Figure 5.20 and are noted as smooth versions of the otherwise crude but longer running reconstructions from Figure 5.17.

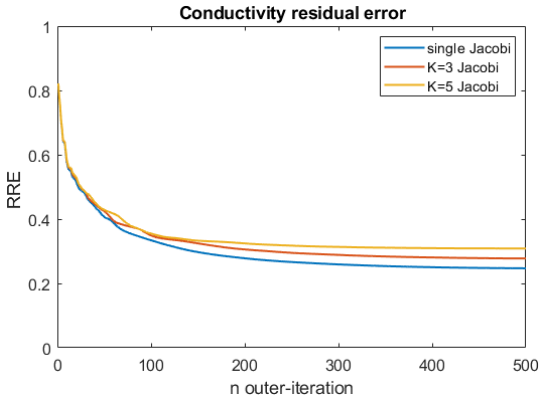

Figure 5.14: Relative residual error in the conductivity reconstructions comparing the single and multiple Jacobi step regularization CSI-EPT versions.

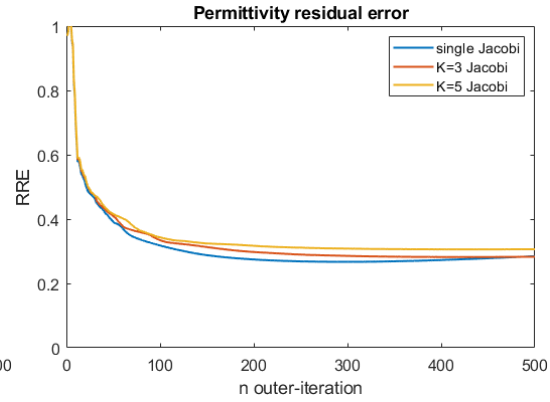

Figure 5.15: Relative residual error in the conductivity reconstructions comparing the single and multiple Jacobi step regularization CSI-EPT versions.

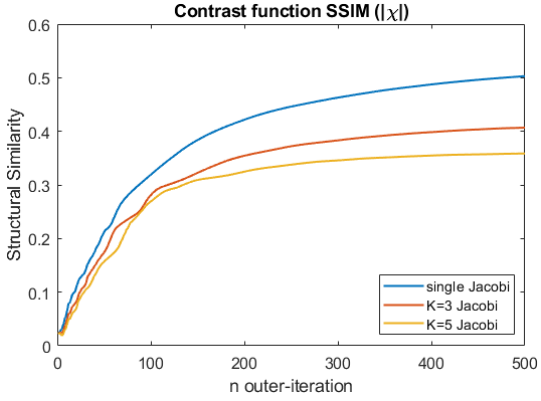

Figure 5.16: Sufficient SSIM of the contrast does not occur earlier for the multiple Jacobi step versions than the regular single Jacobi step regularization.

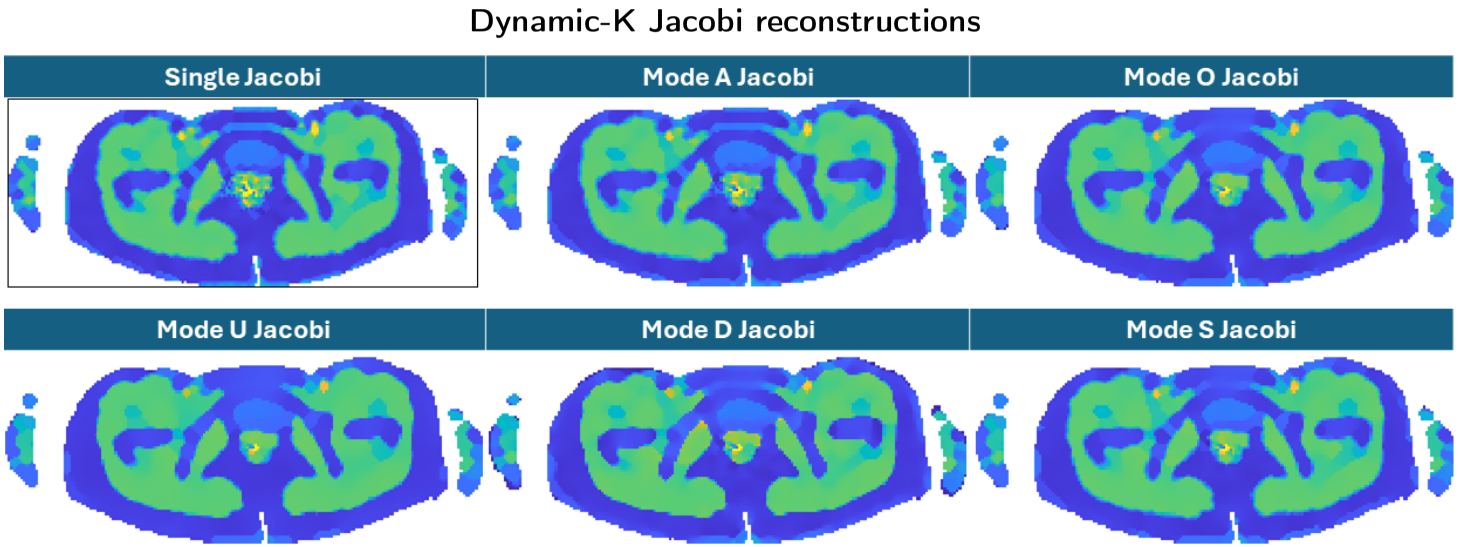

Figure 5.17: The reconstructions from the different dynamic-K modes of Jacobi step reconstruction compared to the single Jacobi step reconstruction highlighted in the top left. Results from reconstructions at 40dB SNR and 500 outer-iterations.

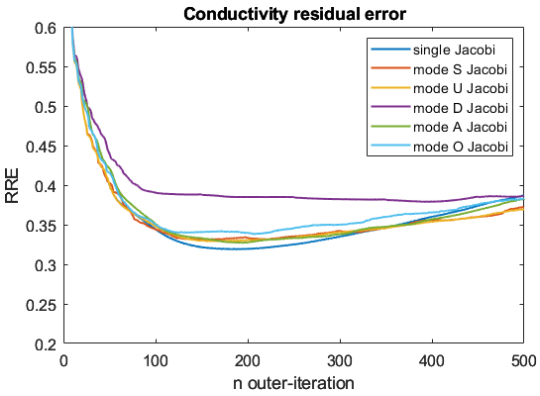

Figure 5.18: RRE of reconstructed conductivity profile of the pelvis model for 30dB SNR transmit field noise.

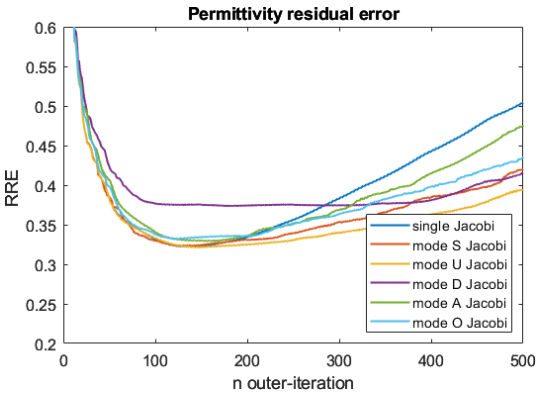

Figure 5.19: RRE of reconstructed permittivity profile of the pelvis model for 30dB SNR transmit field noise.

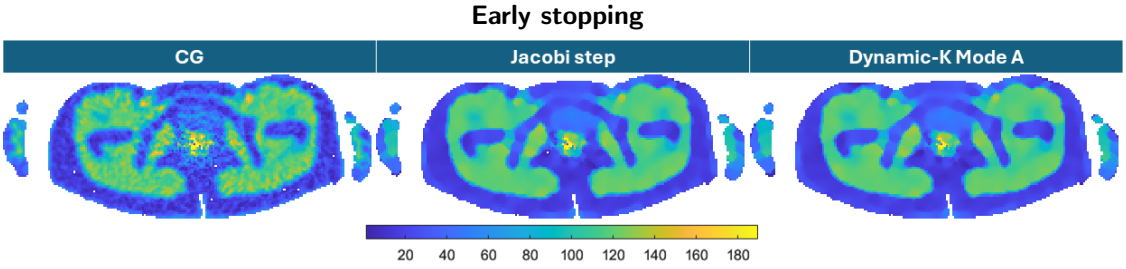

Figure 5.20: Early stopping reconstructions of the Conjugate Gradient, single Jacobi step and dynamic-K mode A regularized contrast updating using the Berg-Abubakar regularization parameter for 200 outer-iterations.

The increase in inner-iterations also does not result in early structural quality improvements over the single Jacobi regularization as is seen in Figures 5.21 and 5.22. The hypothesized mechanism of *a priori* knowledge improving reconstruction quality while the subsequent iterations refine the details is concluded not to be present in these CSI-EPT reconstructions.

5.2.2. CONTRAST SOURCE INITIALIZATION TESTING

The modality rescaling method from Section 4.2 was applied to initialize contrast for the Jacobi step and conjugate gradient reconstructions of the pelvis, respectively seen in Figures 5.23 and 5.24. These figures compare the reconstruction results from the different initialization methods back propagation (highlighted with a black border), the *a priori* knowledge based initialization from CT and MRI imaging; and initializing the contrast to be the ground truth contrast (the bottom left reconstruction).

Edge preservation of the Jacobi step regularization is present in areas where both the initialization and the true contrast have strong edges. Examples are the bone structures for CT initialization and bladder and blood vessels for MRI initialization. This results in clearly defined bone tissue boundaries for the "CT no offset" initialized reconstruction

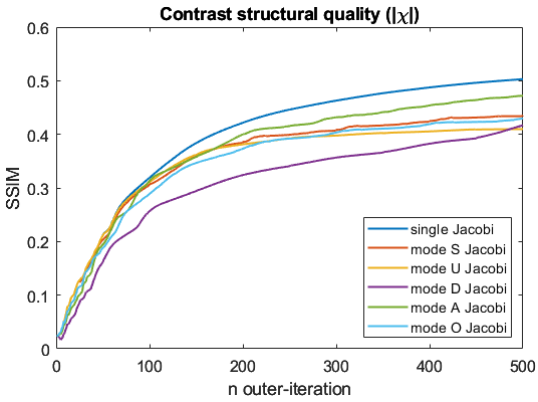

Figure 5.21: SSIM of the absolute contrast reconstruction of the pelvis model for **40dB** SNR transmit field noise.

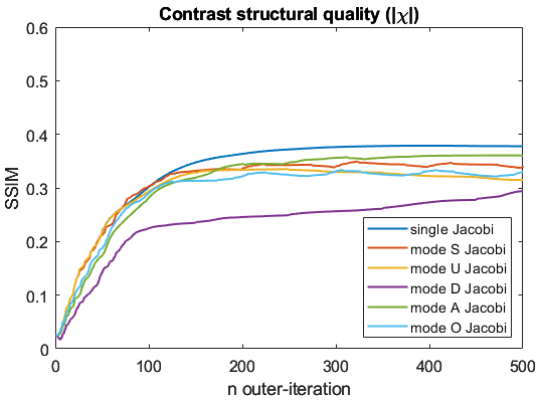

Figure 5.22: SSIM of the absolute contrast reconstruction of the pelvis model for **30dB** SNR transmit field noise.

5

and similar for the distinct muscle tissue boundaries and vessels in the MRI initialized counterpart. However, when the initialization contains a similar strong edge but at the wrong location, as is seen in CT initialization with a slice offset, this strong edge is seen to persist throughout the reconstruction process. Hence between the right pelvic and femoral bones in the "CT offset 1" reconstruction there is a small region of strong contrast remaining.

Finally, initializing with the ground truth contrast this strong edge preservation leads to the retention of the intricate structures in the hands and the thin muscle tissue in front of the bladder. These structures are usually smoothed during reconstruction.

In general, these reconstructions show that the Jacobi step regularized CSI-EPT is mostly robust against slight structural errors in its initialization and at best can retain sharp tissue boundaries when the initialization and ground truth agree in these areas. Similar edge-preservation from *a priori* structural knowledge is not exhibited in the conjugate gradient regularized CSI-EPT counterpart. This is highlighted in the metric Tables 5.4 and 5.5. Here the RRE and SSIM scores of CG reconstructions are worse than the Jacobi equivalents; hence the red coloring of these rows. On the contrary, utilizing the back propagation initialization method for CG CSI-EPT still achieves relatively good reconstructions compared to initializations from slightly offset structural priors.

Initialization	Reg.	RRE σ		RRE ε	
		SNR = 40 dB	50 dB	40 dB	50 dB
CT 0	CG	0.2585	0.2178	0.4419	0.3864
	Jacobi	0.2394	0.2102	0.3138	0.3052
MRI 0	CG	0.3023	0.2807	0.3485	0.2981
	Jacobi	0.2385	0.2176	0.2718	0.2238
CT 1	CG	0.2953	0.2618	0.4140	0.3552
	Jacobi	0.2570	0.2425	0.3046	0.2818
MRI 1	CG	0.2804	0.2572	0.4007	0.3603
	Jacobi	0.2495	0.2204	0.2906	0.2560
BP	CG	0.2499	0.2124	0.3014	0.2246
	Jacobi	0.2470	0.2108	0.2843	0.2207
GT	CG	0.3250	0.2960	0.3600	0.2990
	Jacobi	0.2120	0.2140	0.2330	0.1530

Table 5.4: RRE metrics from the CG and Jacobi step regularized reconstructions initialized with CT, MRI modality rescaling or ground truth (GT) contrasts or back propagation (BP) at 40 and 50 dB transmit field SNR. The red to green coloring scale highlights the results from bad to good quality compared to the other values in the column.

Initialization	Reg.	SSIM $\lvert\chi\rvert$		SSIM σ		SSIM ε	
		SNR = 40 dB	50	40	50	40	50
CT 0	CG	0.4845	0.5307	0.8008	0.8658	0.3289	0.3963
	Jacobi	0.4910	0.5292	0.8256	0.8649	0.4415	0.4590
MRI 0	CG	0.4770	0.5091	0.7635	0.8086	0.3783	0.4212
	Jacobi	0.5152	0.5619	0.8371	0.8751	0.5023	0.5416
CT 1	CG	0.4709	0.5118	0.7734	0.8342	0.3444	0.4098
	Jacobi	0.4935	0.5149	0.8200	0.8419	0.4656	0.4796
MRI 1	CG	0.4737	0.4999	0.7709	0.8134	0.3431	0.3808
	Jacobi	0.4879	0.5425	0.8175	0.8669	0.4703	0.5108
BP	CG	0.5021	0.5467	0.8028	0.8680	0.4244	0.5020
	Jacobi	0.5029	0.5537	0.8300	0.8779	0.4870	0.5300
GT	CG	0.5430	0.5890	0.7360	0.7920	0.4780	0.5420
	Jacobi	0.5930	0.6200	0.8960	0.8870	0.5780	0.6290

Table 5.5: SSIM metrics from the CG and Jacobi step regularized reconstructions initialized with CT, MRI modality rescaling or ground truth (GT) contrasts or back propagation (BP) at 40 and 50 dB transmit field SNR. The red to green coloring scale highlights the results from bad to good quality compared to the other values in the column.

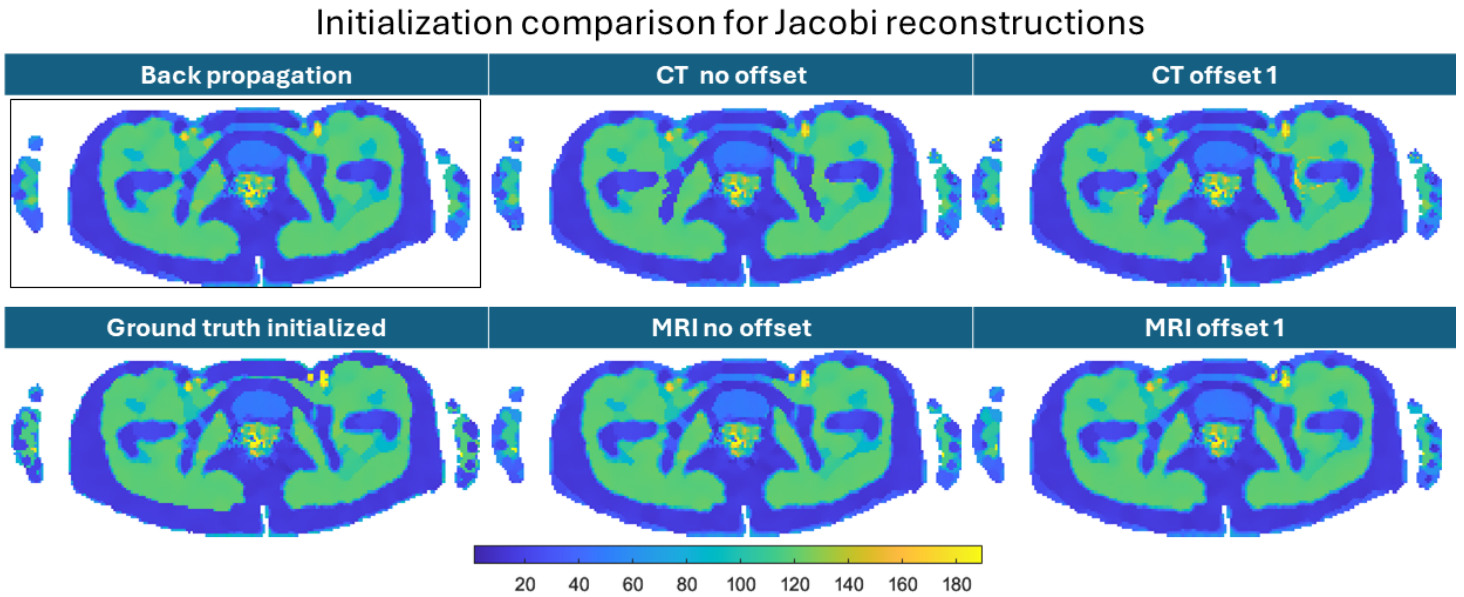

Figure 5.23: Comparison of Jacobi step reconstruction using the initialization methods: back propagation (as seen in earlier comparisons), CT and MRI imaging modalities with and without slice offset and using the ground truth as contrast initialization.

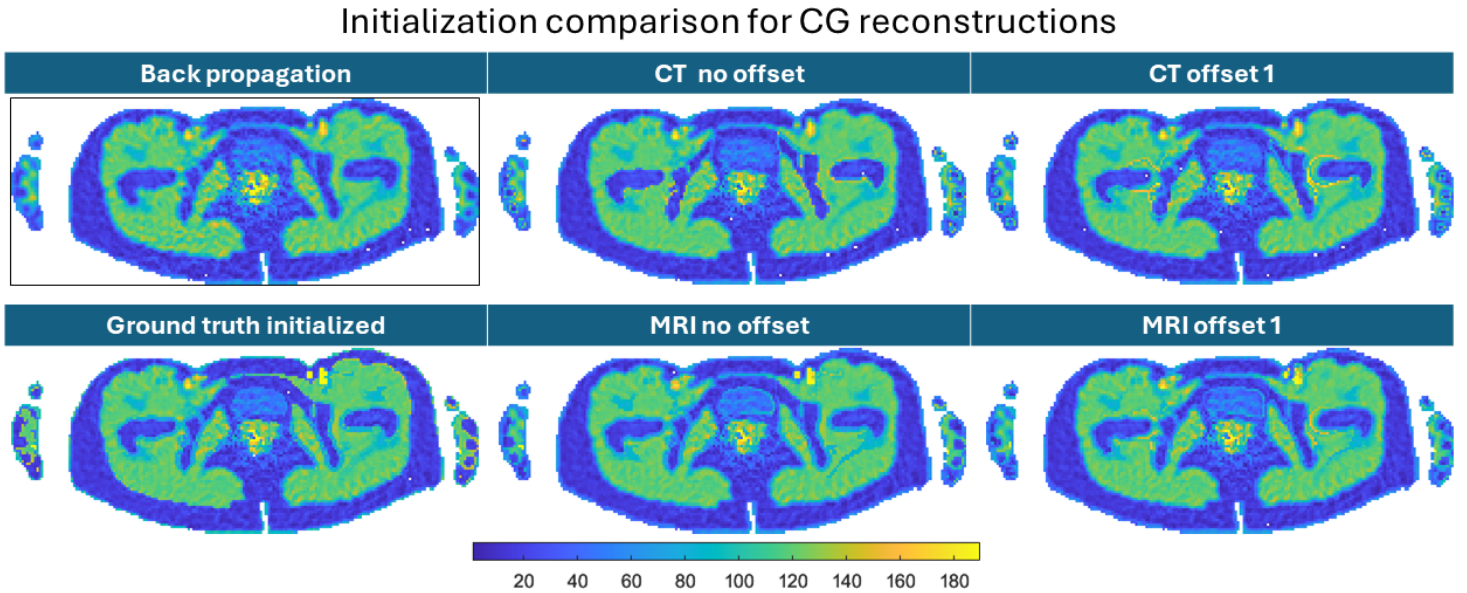

Figure 5.24: Comparison of conjugate gradient reconstruction using the initialization methods: back propagation, CT and MRI imaging modalities with and without slice offset and using the ground truth as contrast initialization.

6

CONCLUSION

This thesis has presented a novel regularization method in the electrical properties reconstruction problem that is Contrast Source Inversion Electrical Properties Tomography (CSI-EPT). Reconstruction of the conductivity and relative permittivity of tissue based on simulated MRI tractable data is shown to improve for the CSI-EPT method compared to other method variants. Total Variation regularization was applied to perform noise suppression while maintaining the edges of the piece-wise electrical properties profile. The multiplicative nature of the regularization meanwhile limits regularization parameter optimization that is otherwise common to additive forms of regularization. The Jacobi method is employed to enact the regularized contrast updating step in CSI-EPT, hence named the Jacobi step CSI-EPT.

This proved to be a robust regularization method for noise suppression and edge-preservation of the reconstructed tissue electrical properties, while the reconstruction process is unchanged in computation time complexity compared to the already existing Conjugate Gradient regularization.

The Jacobi step CSI-EPT is a more flexible regularization method than the CG regularization method. The Jacobi step CSI-EPT responds strongly to the change of the regularization parameter $\delta^{(n)}$ which is noted in the applied regularization strength throughout the reconstruction process. By changing the regularization parameter the reconstructions of the head model changed from crude to more detailed yet also more noisy reconstructions in similar fashion to the CG regularized reconstructions.

Furthermore, the option to apply multiple Jacobi inner-iterations within one CSI-EPT iteration was explored. By increasing that amount of inner-iterations benefits in terms of reconstruction quality or reduction of reconstruction time were hypothesized. However, such benefits were not observed as a result of increased TV regularization strength associated with each additional Jacobi inner-iteration. The general conclusion on TV regularization strength reads: too strong regularization leads to crude or oversimplified reconstructions while too weak regularization is unable to suppress noise.

Additionally, unconventional initialization based on anatomical *a priori* information, which is presumably known prior to the execution of the CSI-EPT methods, was performed. Acquisition of the required transmit field data and conventional imaging of the anatomical structure can theoretically be combined in the medical context of MR-EPT. Hence utilizing the structural prior knowledge for initialization of the contrast was

theorized as a potential improvement to the practical application of CSI-EPT. The results for this anatomical prior initialization indicate that edge preservation of the Jacobi step CSI-EPT is enhanced at areas where the initialization and ground truth contrast agree. However, slight tissue boundary errors from the initialization contrast may persist and then degrade the reconstruction quality in comparison to reconstructions from the common back propagation initialization method.

The Jacobi step regularization method is thus recommended for future implementations of CSI-EPT in order to further advancements in medical diagnostics or providing more complete insight into the EM interactions inside MRI or other EM systems.

6.1. DISCUSSION AND FUTURE RECOMMENDATIONS

Given the proposed methods and resulting contributions presented in this thesis there are some points warranting further discussion leading into future recommendations for the Jacobi step regularization and general CSI-EPT method.

The results presented were made using field simulations for a 3T MRI machine. Knowing that the contribution to admittance shifts from the conductivity to the permittivity when the main magnetic field strength increases, it is important to test the reconstruction quality at different main magnetic field strengths. Reconstruction accuracy of the conductivity profile at 3T was better than that of the permittivity profile. This was explained by the higher share in admittance that the conductivity forms at 3T imaging compared to the permittivity. This is reversed when the angular frequency increases in higher main magnetic field strength MRI imaging.

Furthermore, the contrast initialization method in the current form is not extensively tested and developed for application to entire regions of the body. The implementation currently does not take into account the noise that is usually present in CT and MRI imaging. As a consequence the initialization results only represent an ideal situation.

An obvious recommendation is to extend the Jacobi step regularization to the three-dimensional CSI-EPT method presented in Leijsen et al. [53]. In three dimensions the 2-point finite difference approach to the weighted Laplacian operator $\nabla\cdot(b^{(n)}\nabla\chi)$ should result in an additional two points per voxel in the calculation of the Jacobi regularized contrast.

This thesis presented the factors that influence the strength of the regularization. Section 5.1 highlighted the situation where the strength was adjusted by changing the regularization parameter when the region of interest changed from the pelvis to the head model. However, ideally one would apply the Jacobi step regularization without having to switch the parameter. For a potential full body 3D CSI-EPT reconstruction the question arises whether it is appropriate to use the regularization parameter that guarantees reconstruction quality in the pelvis or in the head region. Hence, it is recommended that the strength of the Jacobi step regularization is better understood in terms of the input noise level, the reconstruction regions of interest and the regularization parameter. Potentially, a regularization parameter can then be found that maintains a balance in the trade-off between noise-suppression and detail of the final reconstruction. Otherwise there is the alternative of increasing resolution, e.g. using interpolation techniques or during acquisition of the data, such that the finer structures in the EP profiles are less affected by the stronger TV regularization. However, this not only increases computation

times but also complicates either pre-processing or acquisition processes.

In the elaboration of the non-linear Euler-Lagrange equation of Section 3.5.1, the first-order linearization with respect to the contrast difference term $\delta\chi$ leads to the Jacobi step implementation. Van den Berg [15] states that such a first-order linearization suffices for the purposes of finding a regularization method. Yet when allowing the second order terms or an elaboration of the nonlinear Euler-Lagrange equation is employed it could be argued that the minimization of the total regularized cost is better approximated. However, when such an elaboration was experimented with the resulting reconstructions exhibited stronger regularization and thus again more crude reconstructions. This was therefore abandoned quickly in the final days of working on the thesis.

The results in this thesis and the majority of the research on CSI-EPT are based on simulations of the MRI data and fields, however, to evaluate practical applicability of the algorithm a few general recommendations are mentioned.

Improving fidelity of the simulations allows for a more faithful evaluation of CSI-EPT and the performance of the Jacobi step regularization. Such an improvement was shown in [39] through taking into account the coil loading effect on the basis of contrast profiles that are non-ideal yet available *a priori* in practical contexts. A specific improvement for this thesis is the use of external EM simulation software to incorporate effects that influence the fidelity of the simulated field data such as coil loading effects and effects from a fully modelled bird cage and RF shielding instead of the line sources approximation. Yet, increasing the fidelity does not mean better results or more practical application. Therefore, such modeling steps must be critically evaluated in terms of the practical complexity versus the benefits in reconstruction accuracy that they may provide.

Finally, there is the issue of the non-ideal transceive phase field measurements. The application of the Jacobi step regularization has been shown for the basic CSI-EPT algorithm, however, the regularization has not been tested on the TPC CSI-EPT algorithm or a similar transmit field amplitude only CSI-EPT algorithm. Neither has it been shown whether the increased likelihood of running into local minima (due to the modified cost function) is significant to the performance of the TPC CSI-EPT algorithm. Some reconstructions have been performed but lacked conclusive elaboration and are therefore placed in the appendix Section A.3.

Adopting algorithms that are able to handle the non-ideal transceive field measurement data finally allows evaluation of performance based on actual MRI measurements such as in [33]. Furthermore, the regularization can then be tested on the recently published ADEPT dataset [54] for the further promotion of standardized testing in the research field and further comparison with the other MR-EPT methods.

BIBLIOGRAPHY

[1] R. L. Siegel, K. D. Miller, N. S. Wagle, and A. Jemal, "Cancer statistics, 2023", *CA Cancer J. Clin.*, vol. 73, no. 1, pp. 17–48, Jan. 2023.

[2] C. Santucci, S. Mignozzi, M. Malvezzi, *et al.*, "European cancer mortality predictions for the year 2024 with focus on colorectal cancer", *Annals of Oncology*, 2024, ISSN: 0923-7534. DOI: https://doi.org/10.1016/j.annonc.2023.12.003.

[3] M. Roser and H. Ritchie, "Cancer", *Our World in Data*, 2019. [Online]. Available: https://ourworldindata.org/cancer.

[4] C. Gabriel, S. Gabriel, and E. Corthout, "The dielectric properties of biological tissues: 1. literature survey", *Physics in medicine and biology*, vol. 41, pp. 2231–49, Dec. 1996. DOI: 10.1088/0031-9155/41/11/001.

[5] S. Gabriel, R. W. Lau, and C. Gabriel, "The dielectric properties of biological tissues: 2. measurements in the frequency range 10 hz to 20 ghz", *Physics in Medicine and Biology*, vol. 41, no. 11, p. 2251, Nov. 1996. DOI: 10.1088/0031-9155/41/11/002.

[6] S. Gavazzi, P. Limone, G. D. Rosa, F. Molinari, and G. Vecchi, "Comparison of microwave dielectric properties of human normal, benign and malignant thyroid tissues obtained from surgeries: A preliminary study", *Biomedical Physics and Engineering Express*, vol. 4, no. 4, p. 047 003, May 2018. DOI: 10.1088/2057-1976/aa9f77.

[7] S. Huang, W. Cai, S. Han, *et al.*, "Differences in the dielectric properties of various benign and malignant thyroid nodules", *Medical Physics*, vol. 48, no. 2, pp. 760–769, 2021. DOI: https://doi.org/10.1002/mp.14562.

[8] K. Sasaki, E. Porter, E. A. Rashed, L. Farrugia, and G. Schmid, "Measurement and image-based estimation of dielectric properties of biological tissues —past, present, and future—", *Physics in Medicine and Biology*, vol. 67, no. 14, 14TR01, Jul. 2022. DOI: 10.1088/1361-6560/ac7b64.

[9] J. Shin, M. J. Kim, J. Lee, *et al.*, "Initial study on in vivo conductivity mapping of breast cancer using mri", *Journal of Magnetic Resonance Imaging*, vol. 42, no. 2, pp. 371–378, 2015. DOI: https://doi.org/10.1002/jmri.24803.

[10] I. Hancu, J. C. Roberts, S. Bulumulla, and S.-K. Lee, "On conductivity, permittivity, apparent diffusion coefficient, and their usefulness as cancer markers at mri frequencies", *Magnetic Resonance in Medicine*, vol. 73, no. 5, pp. 2025–2029, 2015. DOI: https://doi.org/10.1002/mrm.25309.

[11] R. Pethig, "Dielectric properties of biological materials: Biophysical and medical applications", *IEEE Transactions on Electrical Insulation*, vol. EI-19, no. 5, pp. 453–474, 1984. DOI: 10.1109/TEI.1984.298769.

[12] R. Pethig, "Dielectric properties of body tissues", *Clinical Physics and Physiological Measurement*, vol. 8, no. 4A, p. 5, Nov. 1987. DOI: 10.1088/0143-0815/8/4A/002.

[13] R. Leijsen, W. Brink, C. van den Berg, A. Webb, and R. Remis, "Electrical properties tomography: A methodological review", *Diagnostics*, vol. 11, no. 2, 2021, ISSN: 2075-4418. DOI: 10.3390/diagnostics11020176.

[14] E. Balidemaj, C. A. van den Berg, J. Trinks, *et al.*, "CSI-EPT: A contrast source inversion approach for improved mri-based electric properties tomography", *IEEE Transactions on Medical Imaging*, vol. 34, no. 9, pp. 1788–1796, 2015. DOI: 10.1109/TMI.2015.2404944.

[15] P. M. van den Berg, *Forward and Inverse Scattering Algorithms Based on Contrast Source Integral Equations*. Hoboken, NJ: John Wiley and Sons, Inc., 2021, ISBN: 978-1-119-74160-2.

[16] D. I. Hoult, "The principle of reciprocity in signal strength calculations—a mathematical guide", *Concepts in Magnetic Resonance*, vol. 12, no. 4, pp. 173–187, 2000. DOI: https://doi.org/10.1002/1099-0534(2000)12:4<173::AID-CMR1>3.0.CO;2-Q.

[17] J. Liu, Y. Wang, U. Katscher, and B. He, "Electrical properties tomography based on $B_{\{1\}}$ maps in MRI: Principles, applications, and challenges", en, *IEEE Trans. Biomed. Eng.*, vol. 64, no. 11, pp. 2515–2530, Nov. 2017.

[18] F. Schweser, A. Deistung, and J. R. Reichenbach, "Foundations of mri phase imaging and processing for quantitative susceptibility mapping (qsm)", *Zeitschrift für Medizinische Physik*, vol. 26, no. 1, pp. 6–34, 2016, ISSN: 0939-3889. DOI: https://doi.org/10.1016/j.zemedi.2015.10.002.

[19] S. Mandija, A. Sbrizzi, U. Katscher, P. R. Luijten, and C. A. van den Berg, "Error analysis of helmholtz-based mr-electrical properties tomography", *Magnetic Resonance in Medicine*, vol. 80, no. 1, pp. 90–100, 2018. DOI: https://doi.org/10.1002/mrm.27004.

[20] T. Voigt, U. Katscher, and O. Doessel, "Quantitative conductivity and permittivity imaging of the human brain using electric properties tomography", *Magnetic Resonance in Medicine*, vol. 66, no. 2, pp. 456–466, 2011. DOI: https://doi.org/10.1002/mrm.22832.

[21] A. Arduino, F. Pennecchi, U. Katscher, M. Cox, and L. Zilberti, "Repeatability and reproducibility uncertainty in magnetic resonance-based electric properties tomography of a homogeneous phantom", *Tomography*, vol. 9, no. 1, pp. 420–435, 2023, ISSN: 2379-139X. DOI: 10.3390/tomography9010034.

[22] P. Berg and A. Abubakar, "Contrast source inversion method: State of art", *Journal of Electromagnetic Waves and Applications*, vol. 15, pp. 1503–1505, Jan. 2001. DOI: 10.1163/156939301X00067.

[23] R. Hong, S. Li, J. Zhang, *et al.*, "3-D MRI-based electrical properties tomography using the volume integral equation method", *IEEE Transactions on Microwave Theory and Techniques*, vol. PP, pp. 1–10, Jul. 2017. DOI: 10.1109/TMTT.2017.2725830.

[24] J. E. C. Serrallés, I. I. Giannakopoulos, B. Zhang, *et al.*, "Noninvasive estimation of electrical properties from magnetic resonance measurements via global maxwell tomography and match regularization", *IEEE Transactions on Biomedical Engineering*, vol. 67, no. 1, pp. 3–15, 2020. DOI: 10.1109/TBME.2019.2907442.

[25] P. S. Fuchs, S. Mandija, P. R. S. Stijnman, W. M. Brink, C. A. T. van den Berg, and R. F. Remis, "First-order induced current density imaging and electrical properties tomography in MRI", *IEEE Transactions on Computational Imaging*, vol. 4, no. 4, pp. 624–631, 2018. DOI: 10.1109/TCI.2018.2873407.

[26] G. Bal, "Hybrid inverse problems and internal functionals", *Inverse problems and applications: inside out. II*, vol. 60, pp. 325–368, 2013.

[27] J. K. Seo and E. J. Woo, "Magnetic resonance electrical impedance tomography (mreit)", *SIAM Review*, vol. 53, no. 1, pp. 40–68, 2011. DOI: 10.1137/080742932.

[28] A. Timonov, "A novel method for the numerical solution of a hybrid inverse problem of electrical conductivity imaging", *Journal of Mathematical Sciences*, pp. 1–16, 2023.

[29] R. Leijsen, P. Fuchs, W. Brink, A. Webb, and R. Remis, "Developments in electrical-property tomography based on the contrast-source inversion method", *Journal of Imaging*, vol. 5, no. 2, 2019, ISSN: 2313-433X. DOI: 10.3390/jimaging5020025.

[30] R. Kleinman and P. den Berg, "A modified gradient method for two- dimensional problems in tomography", *Journal of Computational and Applied Mathematics*, vol. 42, no. 1, pp. 17–35, 1992, ISSN: 0377-0427. DOI: https://doi.org/10.1016/0377-0427(92)90160-Y.

[31] C. E. Hayes, W. A. Edelstein, J. F. Schenck, O. M. Mueller, and M. Eash, "An efficient, highly homogeneous radiofrequency coil for whole-body nmr imaging at 1.5 t", *Journal of Magnetic Resonance (1969)*, vol. 63, no. 3, pp. 622–628, 1985, ISSN: 0022-2364. DOI: https://doi.org/10.1016/0022-2364(85)90257-4.

[32] S. F. Ahmad, Y. C. Kim, I. C. Choi, and H. D. Kim, "Recent progress in birdcage RF coil technology for MRI system", en, *Diagnostics (Basel)*, vol. 10, no. 12, p. 1017, Nov. 2020.

[33] P. R. S. Stijnman, S. Mandija, P. S. Fuchs, C. A. T. van den Berg, and R. F. Remis, "Transceive phase corrected 2d contrast source inversion-electrical properties tomography", *Magnetic Resonance in Medicine*, vol. 85, no. 5, pp. 2856–2868, 2021. DOI: https://doi.org/10.1002/mrm.28619.

[34] A. L. H. M. W. van Lier, A. Raaijmakers, T. Voigt, *et al.*, "Electrical properties tomography in the human brain at 1.5, 3, and 7t: A comparison study", *Magnetic Resonance in Medicine*, vol. 71, no. 1, pp. 354–363, 2014. DOI: https://doi.org/10.1002/mrm.24637.

[35] A. Arduino, O. Bottauscio, M. Chiampi, and L. Zilberti, "Magnetic resonance-based imaging of human electric properties with phaseless contrast source inversion", *Inverse Problems*, vol. 34, no. 8, p. 084 002, Jun. 2018. DOI: 10.1088/1361-6420/aac536.

[36] L. Li, H. Zheng, and F. Li, "Two-dimensional contrast source inversion method with phaseless data: Tm case", *IEEE Transactions on Geoscience and Remote Sensing*, vol. 47, no. 6, pp. 1719–1736, 2009. DOI: 10.1109/TGRS.2008.2006360.

[37] A. Arduino, L. Zilberti, M. Chiampi, and O. Bottauscio, "CSI-EPT in presence of RF-shield for MR-coils", en, *IEEE Trans. Med. Imaging*, vol. 36, no. 7, pp. 1396–1404, Jul. 2017.

[38] J. Jin, *Electromagnetic analysis and design in magnetic resonance imaging*, English (US). CRC Press, Jan. 2018, ISBN: 084939693X. DOI: 10.1201/9780203758731.

[39] R. L. Leijsen, W. M. Brink, A. G. Webb, and R. F. Remis, "Effects of simulated error-sources on different 3-d csi-ept strategies", *IEEE Transactions on Computational Imaging*, vol. 7, pp. 713–723, 2021. DOI: 10.1109/TCI.2021.3094742.

[40] L. Guo, M. Li, P. Nguyen, F. Liu, and S. Crozier, "Integral MR-EPT with the calculation of coil current distributions", en, *IEEE Trans. Med. Imaging*, vol. 39, no. 1, pp. 175–187, Jan. 2020.

[41] A. E. Li, S. T. Jawetz, H. G. Greditzer, A. J. Burge, D. H. Nawabi, and H. G. Potter, "Mri for the preoperative evaluation of femoroacetabular impingement", *Insights into Imaging*, vol. 7, pp. 187–198, 2016. DOI: 10.1007/s13244-015-0459-0.

[42] R. Leijsen, C. van den Berg, A. Webb, R. Remis, and S. Mandija, "Combining deep learning and 3d contrast source inversion in mr-based electrical properties tomography", *NMR in Biomedicine*, vol. 35, no. 4, e4211, 2022. DOI: https://doi.org/10.1002/nbm.4211.

[43] S. Mandija, E. F. Meliadò, N. R. F. Huttinga, P. R. Luijten, and C. A. T. van den Berg, "Opening a new window on MR-based electrical properties tomography with deep learning", en, *Sci. Rep.*, vol. 9, no. 1, p. 8895, Jun. 2019.

[44] P. M. van den Berg and R. E. Kleinman, "A total variation enhanced modified gradient algorithm for profile reconstruction", *Inverse Problems*, vol. 11, no. 3, p. L5, Jun. 1995. DOI: 10.1088/0266-5611/11/3/002.

[45] P. M. van den Berg, A. Abubakar, and J. T. Fokkema, "Multiplicative regularization for contrast profile inversion", *Radio Science*, vol. 38, no. 2, DOI: https://doi.org/10.1029/2001RS002555.

[46] R. Courant and D. Hilbert, "The calculus of variations", in *Methods of Mathematical Physics*. Inter-science Publishers, 1953, vol. 1, ch. 4, pp. 164–274, ISBN: 047017952.

[47] Y. Saad, *Iterative Methods for Sparse Linear Systems*, Second. Society for Industrial and Applied Mathematics, 2003. DOI: 10.1137/1.9780898718003.

[48] P. R. Haffinger, *Seismic Broadband Full Waveform Inversion by shot/receiver refocusing*. Delft, Netherlands: Delft University of Technology, 2013, ISBN: 9789088915086. DOI: doi.org/10.4233/uuid:d2d8d264-5037-4573-8418-a079afa8d1e7.

[49] A. Christ, W. Kainz, E. G. Hahn, *et al.*, "The virtual family—development of surface-based anatomical models of two adults and two children for dosimetric simulations", *Physics in Medicine and Biology*, vol. 55, no. 2, N23, Dec. 2009. DOI: 10.1088/0031-9155/55/2/N01.

[50] R. Remis and E. Charbon, "An electric field volume integral equation approach to simulate surface plasmon polaritons", *Advanced Electromagnetics*, vol. 2, no. 1, pp. 15–24, Feb. 2013. DOI: 10.7716/aem.v2i1.23.

[51] C. M. Collins and M. B. Smith, "Signal-to-noise ratio and absorbed power as functions of main magnetic field strength, and definition of "90 degrees " RF pulse for the head in the birdcage coil", en, *Magn. Reson. Med.*, vol. 45, no. 4, pp. 684–691, Apr. 2001.

[52] Z. Wang, A. Bovik, H. Sheikh, and E. Simoncelli, "Image quality assessment: From error visibility to structural similarity", *IEEE Transactions on Image Processing*, vol. 13, no. 4, pp. 600–612, 2004. DOI: 10.1109/TIP.2003.819861.

[53] R. L. Leijsen, W. M. Brink, C. A. T. van den Berg, A. G. Webb, and R. F. Remis, "3-d contrast source inversion-electrical properties tomography", *IEEE Transactions on Medical Imaging*, vol. 37, no. 9, pp. 2080–2089, 2018. DOI: 10.1109/TMI.2018.2816125.

[54] T. G. Meerbothe, E. F. Meliado, P. R. S. Stijnman, C. A. T. van den Berg, and S. Mandija, "A database for mr-based electrical properties tomography with in silico brain data—adept", *Magnetic Resonance in Medicine*, vol. 91, no. 3, pp. 1190–1199, 2024. DOI: https://doi.org/10.1002/mrm.29904.

A

APPENDIX A: SUPPLEMENTARY MATERIAL

A.1. SYMMETRY OF THE (-R) MATRIX

The (-R) matrix of the regular splitting presented in the Section 3.5.1 is symmetric. To show this, one can take the Laplacian weights $b^{(n)}$ of the contrast χ at point (i, j) and the corresponding row p and column p from the total $P = N_1 N_2$ discretized locations of the N_1 by N_2 imaging domain Ω that are rearranged into the diagonalized matrix representing matrix $A \in \mathbb{R}^{P\times P}$. The scaled entry of (-R) that relates this point to its neighbour at $(i-1, j)$ is positioned N_1 columns to the left in the column and has value

$$(\alpha/2)^{-1}\,[(-R)]_{(p-N_1),p} = b^{(n)}(x_{i-1,j}) + b^{(n)}(x_{i,j}) \tag{A.1}$$

Yet similarly, the point $(i-1, j)$ has the corresponding row and column $p - N_1$ of the scaled entry of (-R) that relates this point to its neighbour at discretized object domain point (i, j), is positioned in the matrix N_1 columns to the right and has value

$$\begin{aligned}(\alpha/2)^{-1}\,[(-R)]_{p,(p-N_1)} &= b^{(n)}(x_{i-1+1,j}) + b^{(n)}(x_{i-1,j}) \\ &= b^{(n)}(x_{i,j}) + b^{(n)}(x_{i-1,j}),\end{aligned} \tag{A.2}$$

which is the same value of the point (i, j). Idem for the relations between neighbours in the other directions (denoted with j's) of the discretized imaging domain. This makes it so that the sum of row p is equivalent to summing over column p in the spectral convergence analysis of the Jacobi method application.

Corollary to this is the statement that $A = D + R$ is also symmetric with D being a diagonal matrix $\in \mathbb{R}^{P\times P}$.

A.2. ORIGINAL ANALYSIS OF LOCAL MINIMA COST FUNCTION

This section serves to elucidate the A_D, B_D and C_D coefficients of Section 3.2.2. The original local minima analysis for CSI-EPT was presented in [22, Section 3.1]. Instead of arriving at the polynomial in β of equation 3.15, the original quartic polynomial is:

$$F(\mathbf{w}, \chi, \phi^{-}) = A_D\beta^4 + 2B_D\beta^3 + (C_D + C_S)\,\beta^2, \tag{A.3}$$

wherein the coefficients are

$$\begin{aligned} A_D &= \eta_D \sum_q \left\| \Delta\chi \mathsf{G}_D\{\Delta w_q\} \right\|_D^2, \\ B_D &= \eta_D \,\mathrm{Re}\left[\sum_q \left\langle \Delta\chi \mathsf{G}_D\{\Delta w_q\}, \Delta\chi u_q^{\mathrm{ex}} - \Delta w_q + \chi^{\mathrm{ex}} \mathsf{G}_D\{\Delta w_q\} \right\rangle_D \right] \\ C_D &= \eta_D \sum_q \left\| \Delta\chi u_q^{\mathrm{ex}} - \Delta w_q + \chi^{\mathrm{ex}} \mathsf{G}_D\{\Delta w_q\} \right\|_D^2 \\ C_S &= \eta_S \sum_q \left\| \mathsf{G}_S\{\Delta w_q\} \right\|_S^2 \end{aligned} \tag{A.4}$$

with u_q^{ex} the exact electric field being the sum of the incident electric field and the scattered electric field $\mathsf{G}_D\{w_q^{\mathrm{ex}}\}$, while domains D and S are the object and source domains of a general inverse scattering problem.

A.3. TRANSCEIVE PHASE CSI-EPT: DISCUSSIONS ON CALCULATION AND COST

The transceive phase CSI-EPT has been performed using TPC CSI-EPT as described in [33] and in this thesis in Section 3.2.2. During various experiments the following points arose that warrant presentation and some description, despite a lack of conclusive explanation.

The first section is on the calculation of the receive fields required for implementation of the transceive phase correction for transceive field based CSI-EPT. Thereafter a discussion on the visualization of the modified transceive field cost function is presented.

A.3.1. TPC CSI-EPT AND THE RECEIVE FIELD

The Transceive Phase Correction CSI-EPT has been implemented according to [33] and performed on the head and pelvis slices. Such reconstructions are presented in Figures A.1 and A.2. The reconstruction of the head is blurry compared to full information transmit field reconstructions. Reconstruction of the pelvis shows similar blurring and two high contrast peaks placed symmetrically on either side of the diagonal of the weak electric field region from the quadrature excitation field. Due to the anti-quadrature excitation of the receive field that enables retrieval of the transceive phase field, it is possible that the contrast peaks originate from the weak electric fields in anti-quadrature excitation.

The original article [33] presents the receive field operator G_S^- as

$$\mathsf{G}_S^{-*}\{\chi^{(n)} E_z^{(n)}\}(\mathbf{x}) = -\frac{k_0^2}{\omega}\partial^- \int_{\mathbf{x}'\in\Omega} G_w(\mathbf{x}-\mathbf{x}')\chi^{(n)}(\mathbf{x}')E_z^{(n)}(\mathbf{x}')\,dV \tag{A.5}$$

Note again the use of the conjugation for calculation of the receive field Fourier coefficients as prescribed by equation 2.14.

When implementing the operator using the FFT method for processing the convolution (see equation 4.5) the receive field Wirtinger partial derivative factor g^{-*} is found

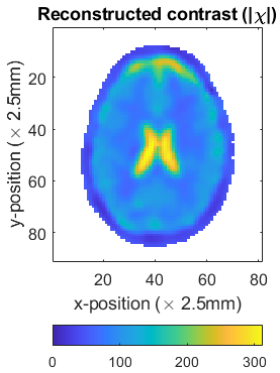

Figure A.1: TPC reconstruction of the head

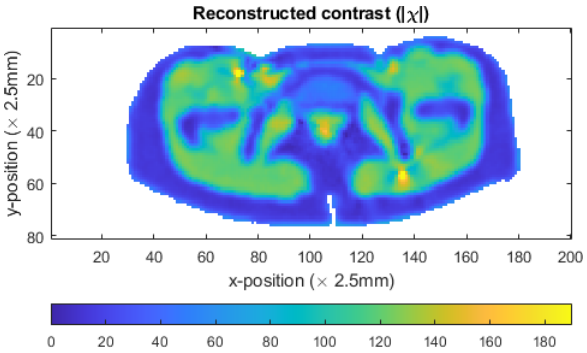

Figure A.2: TPC reconstruction of the pelvis

in similar fashion to g^{+} using equation 4.9. The Wirtinger partial derivative defining the propagation of the transverse receive fields is thus:

$$\begin{aligned} g^{-*}(\mathbf{x}-\mathbf{x}') &= -k_0^2 \partial^- G_w(\mathbf{x}-\mathbf{x}') \\ &= -k_0^2 \frac{(r_x - j r_y)}{2} \left[\frac{j}{2a|\mathbf{r}|} J_1(k_0 a) H_1^{(2)}(k_0|\mathbf{r}|) \right] \end{aligned} \tag{A.6}$$

Hence throughout the TPC CSI-EPT algorithm this is used to perform the receive field data operator:

$$\begin{aligned} \mathsf{G}_S^{-*}\{\chi^{(n)} E_z^{(n)}\} &= -\frac{1}{\omega} \mathrm{FFT}^{-1}\left\{ \mathrm{FFT}\{g^{-*}(\mathbf{x}-\mathbf{x}')\} \cdot \mathrm{FFT}\{\chi^{(n)}(\mathbf{x}') E_z^{(n)}(\mathbf{x}')\} \right\}, \qquad \mathbf{x},\mathbf{x}' \in \Omega \\ &= -\frac{k_0^2}{\omega} \partial^- \int_{\mathbf{x}' \in \Omega} G_w(\mathbf{x}-\mathbf{x}') \chi^{(n)}(\mathbf{x}') E_z^{(n)}(\mathbf{x}') dV, \end{aligned} \tag{A.7}$$

which is in agreement with the Stijnman's receive field operator as implemented with negative sign. However, through an error in derivation a positive sign was implemented which creates the following reconstructions in the Figures A.3 and A.4. The TPC reconstruction of the head has become further blurred, while the pelvis reconstruction is further distorted by a "rippling" artefact; like an envelope attenuating the reconstruction like a ripple in water at the edges of the reconstruction.

A.3.2. TPC COST FUNCTION

In pursuit of finding an explanation for the contrast peaks and rippling artefacts in the TPC pelvis reconstructions, the local minima analysis had been performed that is presented in Section 3.2.2. To further confirm that local minima may be encountered, as possible culprit of the artefacts, the following two parameter CSI-EPT experiment has been devised to visualize the cost function.

In order to visualize local minima in the cost function, we limit ourselves to plotting cost values using only two parameters: uniform conductivity and permittivity. These are

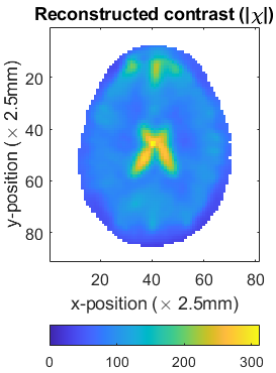

Figure A.3: TPC reconstruction using positively signed scaling for the head from Stijnmans code

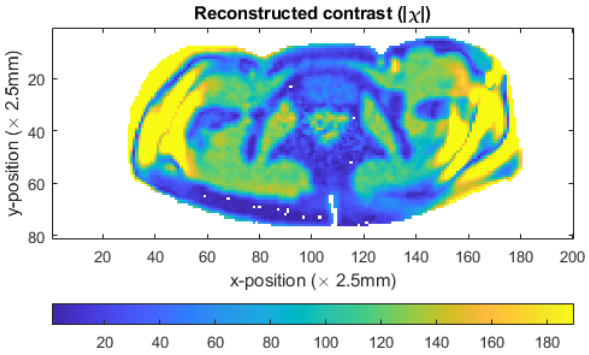

Figure A.4: TPC reconstruction using positively signed scaling for the pelvis from Stijnmans code

the parameters of a circular disc contrast. The unregularized TPC CSI-EPT algorithm is then instructed to reconstruct that disc to provide the next step with EM fields and phases. During every 100 iterations, circular contrast discs are generated with conductivity and relative permittivity values in the respective ranges $[0,3]$ and $[0,100]$; and the EM fields and receive phase are used to produce the total cost function value for each of the electrical properties combinations. Finally, these cost values are plotted in a three dimensional view as can be seen in Figure A.5.

This experiment shows that for this specific, simplified case of TPC CSI-EPT there are no local minima present in the vicinity of the ground truth contrast (denoted with red lines). Hence it lead to good reconstruction of the original circular contrast profile. Unfortunately, the experiment in this form is not able to visualize the cost function shape while reconstructing more elaborate structures such as the pelvis and head models. Introducing a method that is able to provide insight into the convexity of such complex structures for the CSI-EPT problem is recommended to dispel the worry of local minima.

As a side note, at the $3T$ main magnetic field strength the permittivity reconstruction is expected to be less accurate as can be reasoned from Figure A.5. The slopes in the direction of the conductivity are steeper than in the direction of the relative permittivity. Therefore, a correction in the conductivity will bring about a larger cost function improvement than a similar correction in the relative permittivity.

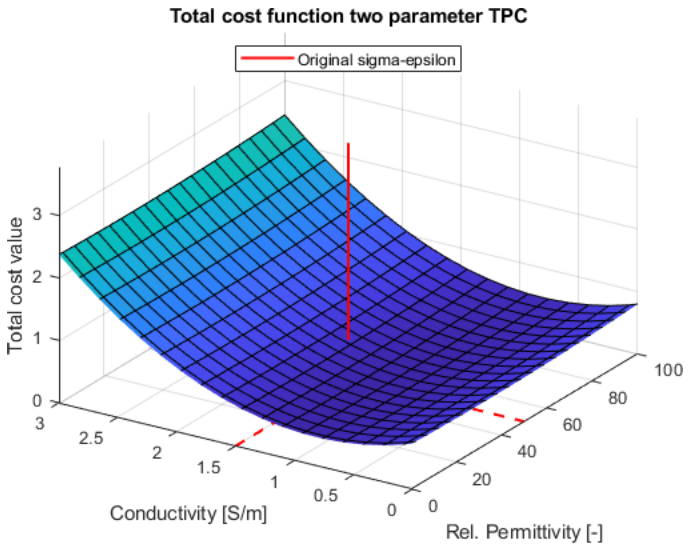

Figure A.5: The cost function values of the round dummie TPC reconstruction at iteration 500 plotted for various combinations of conductivity and relative permittivity. The true EP combination is shown by the red lines.

B

APPENDIX B: ADDITIONAL FIGURES

B.1. QUADRATURE EXCITATION RECONSTRUCTION HEAD AND ABDOMEN

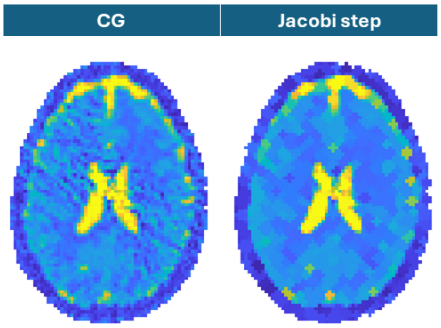

Figure B.1: Regularized reconstructions of the absolute contrast ($|\chi|$) of the head using only the quadrature excitation, 40 dB SNR noise on the transmit field measurement, Berg-Abubakar regularization parameter and 500 iterations.

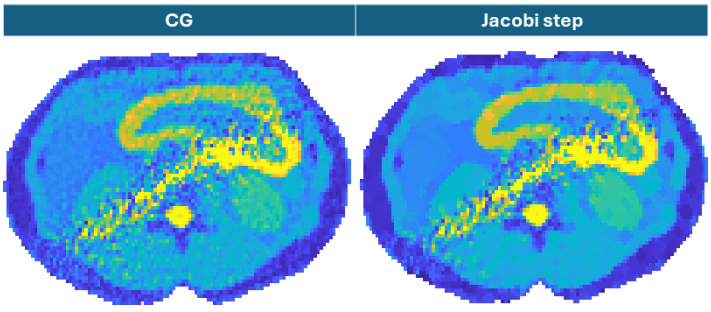

Figure B.2: Regularized reconstructions of the absolute contrast ($|\chi|$) of the abdomen using only the quadrature excitation, 40 dB SNR noise on the transmit field measurement, Berg-Abubakar regularization parameter and 500 iterations.

B.2. REGULARIZATION PARAMETER INFLUENCE

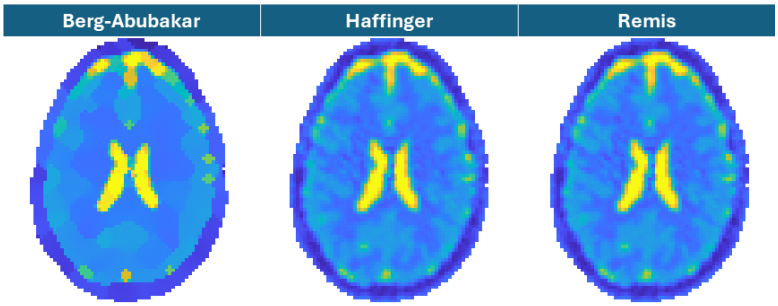

Figure B.3: Jacobi step regularized reconstructions of the absolute contrast ($|\chi|$) of the head using the quadrature and two linear excitations, 40 dB SNR noise on the transmit field measurement and 500 iterations.

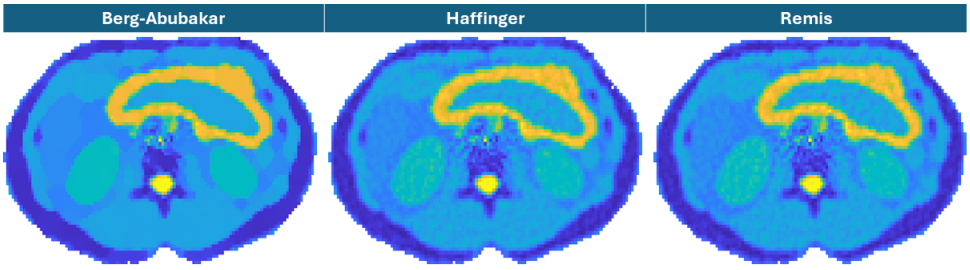

Figure B.4: Jacobi step regularized reconstructions of the absolute contrast ($|\chi|$) of the abdomen using the quadrature and two linear excitations, 40 dB SNR noise on the transmit field measurement and 500 iterations.

B.3. NOISE COMPARISON OF THE ABDOMEN MODEL

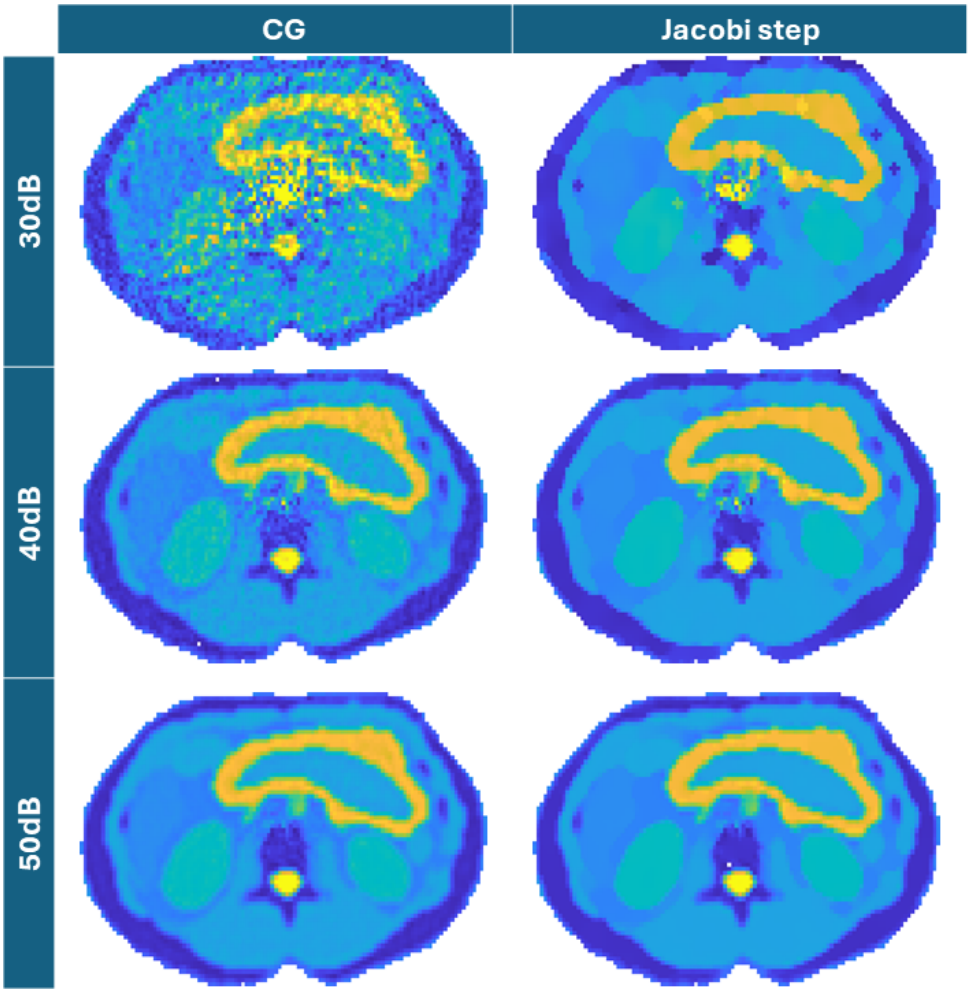

Figure B.5: Input noise of different levels affects the reconstruction of the abdomen in similar fashion as in the pelvis model (see Section 5.1). 500 outer-iterations and the Berg-Abubakar regularization parameter are used.

B

B.4. MULTIPLE ITERATIONS JACOBI

STATIC-K JACOBI RECONSTRUCTIONS HEAD AND ABDOMEN

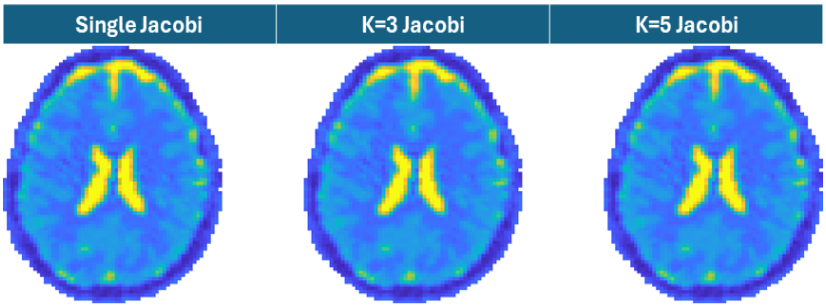

Figure B.6: Multiple inner-iterations reconstructions of the head model at 40dB SNR and 500 outer-iterations.

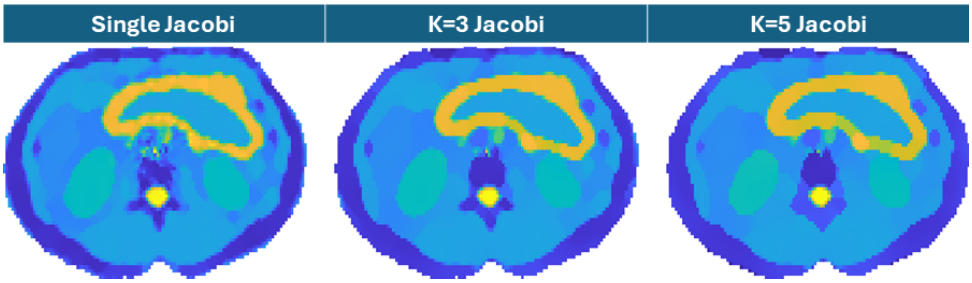

Figure B.7: Multiple inner-iterations reconstructions of the abdomen model at 40dB SNR and 500 outer-iterations.

B.5. CONTRAST INITIALIZATION GUESS

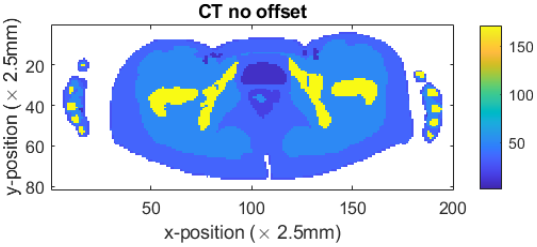

Figure B.8: Absolute contrast of CT anatomical prior contrast initialization of the pelvis model.

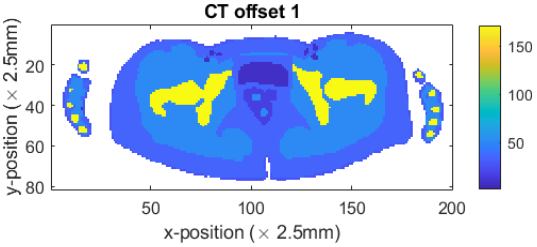

Figure B.9: Absolute contrast of CT anatomical prior contrast initialization of the slice above that of the original pelvis model.

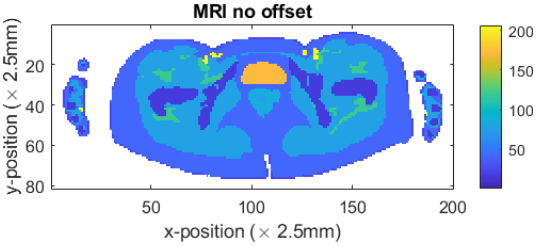

Figure B.10: Absolute contrast of MRI anatomical prior contrast initialization of the pelvis model.

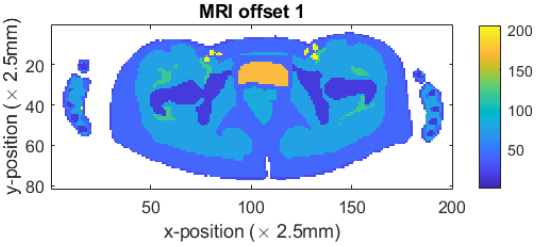

Figure B.11: Absolute contrast of MRI anatomical prior contrast initialization of the slice above that of the original pelvis model.

C

APPENDIX C: IEEE J-ERM PAPER

The article "Improved Multiplicative Regularization for CSI-EPT" published in the IEEE Journal of Electromagnetics, RF and Microwaves in Medicine and Biology describes the findings of this thesis on the Jacobi step regularized CSI-EPT using full transmit field phase information. The article attached (starting on the next page) is the author's latest version of the manuscript and not the published version of the paper. The published version is available at the IEEE Explore page https://ieeexplore.ieee.org/document/10438521 or found using the DOI: 10.1109/JERM.2024.3363428.

IEEE JOURNAL OF ELECTROMAGNETICS, RF AND MICROWAVES IN MEDICINE AND BIOLOGY 1

Improved Multiplicative Regularization for CSI-EPT

Florens Helfferich, Peter M. van den Berg, and Rob F. Remis

C

***Abstract*—We present an improved multiplicative Contrast Source Inversion (CSI) approach for Electrical Properties Tomography (EPT). In EPT, the conductivity and permittivity profiles of a body part are reconstructed based on a known circularly polarized part of the magnetic field (the B_1^+-field) that has its support inside the body part of interest. The CSI method attempts to reconstruct these profiles in an iterative and alternating manner by first fixing the contrast and updating the contrast source (product of tissue contrast and electric field) and subsequently fixing the contrast source and updating the contrast. In this paper, regularization is included in a multiplicative way similar to the standard multiplicative CSI-EPT method. However, the regularized objective function is different and an update for the contrast is obtained through one-step Jacobi filtering of a least-squares reconstruction that is based on the updated contrast source. Two-dimensional numerical experiments for conductivity and permittivity tissue profiles of a female body model show that, for data with various noise levels, the proposed regularization approach generally provides improved tissue reconstructions compared with standard multiplicative CSI-EPT.**

***Keywords*—Magnetic resonance imaging, electrical properties tomography, multiplicative contrast source inversion, B_1^+ field.**

I. INTRODUCTION

ELECTRICAL Properties Tomography or EPT is a hybrid inverse scattering problem in Magnetic Resonance Imaging (MRI) in which the objective is to reconstruct the conductivity and permittivity profiles of a body part of interest [1], [2]. Based on the left-handed circularly polarized part of the magnetic field that is known at the Larmor frequency *inside* the body part of interest (EPT is a so-called hybrid inverse problem with data supported inside the reconstruction domain), reconstruction methods attempt to retrieve the dielectric tissue profiles. Knowledge about the conductivity and permittivity of tissue is of great importance in MR safety [3], [4], [5], hyperthermia treatment planning [6], and stroke imaging [7], for example.

A wide variety of EPT reconstruction approaches have been developed each with its own advantages and disadvantages. We refer to [8] for an overview of these methods and to [9] and [10] as examples of recent learning-based EPT reconstruction methods. In this paper, we focus on the Contrast Source Inversion (CSI) method, which was proposed in [11] for remote sensing problems, applied to various inverse scattering problems in [12], [13], and [14] for example, and applied to the EPT problem in [15]. In particular, we consider a specific one-step Jacobi multiplicative regularization approach for CSI, which was originally proposed for remote sensing problems in [16]. We apply this approach to the EPT problem and demonstrate that it generally provides improved EPT reconstructions of a body part of interest compared with standard multiplicative CSI as obtained in [17], for example, where the effects of various modeling errors in CSI-EPT are discussed as well. The regularization step is noniterative and consists of a simple one-step Jacobi correction of the inverted least-squares contrast. Furthermore, similar to the original multiplicative regularization scheme, no regularization parameter needs to be determined for each new data set and, finally, the computational costs are similar to the costs of the original multiplicative CSI method.

This paper is organized as follows. In Section II we briefly review the basic equations for CSI-EPT. The standard CSI-EPT method and the standard multiplicative CSI-EPT scheme are reviewed in Section III, while the one-step Jacobi regularization approach is presented in Section IV. In Section V we present numerical experiments that demonstrate the effectiveness of the new regularization approach and the conclusions can be found in Section VI.

F. Helfferich is an MSc student at the Faculty of Electrical Engineering, Mathematics, and Computer Science of the Delft University of Technology.

P. M. van den Berg is professor emeritus of the Delft University of Technology.

R. F. Remis is with the Terahertz Sensing Group of the Faculty of Electrical Engineering, Mathematics, and Computer Science of the Delft University of Technology (correspondence e-mail: R.F.Remis@tudelft.nl).

II. BASIC EQUATIONS

Let us first briefly present the basic equations that govern our 2D EPT problem. We consider an E-polarized RF field in a configuration that is invariant in the z-direction. A penetrable body part of interest, characterized by a conductivity σ and a permittivity ε, occupies a bounded domain $\mathbb{D}$ in the xy-plane and is embedded in free space. In EPT, the problem is to reconstruct the conductivity and permittivity profiles of the body from a known circularly polarized part of the magnetic field *inside* the body. This part of the magnetic field is called the B_1^+-field and since the B_1^+-field is known inside the reconstruction domain $\mathbb{D}$, the EPT reconstruction problem is what is called a hybrid inverse problem.

A set of line sources (representing the rungs of a birdcage coil) surrounds the object under test (see also Fig. 1 below). The electric field generated by these sources when the object is absent is denoted as the incident field u^{inc}, while the field that is present when the object is present is denoted as the total field u. The scattered field $u^{\text{sc}} = u - u^{\text{inc}}$ is introduced as the difference between the total and incident field and for this scattered field we have the integral representation

$$u^{\text{sc}}(\mathbf{x}) = k_0^2 \int_{\mathbf{x}' \in \mathbb{D}} G(\mathbf{x} - \mathbf{x}') \chi(\mathbf{x}') u(\mathbf{x}') \, \mathrm{d}V, \qquad (1)$$

which holds for $\mathbf{x} \in \mathbb{R}^2$. In the above equation, $k_0 = \omega/c_0$ is the wave number of the background medium, where c_0 is the electromagnetic wave speed of the background, $G(\mathbf{x}) = -\frac{\mathrm{j}}{4} H_0^{(2)}(k_0|\mathbf{x}|)$ is the Green's function with $H_0^{(2)}$ the Hankel

function of the second kind and order zero, and χ is the contrast function of the object given by

$$\chi(\mathbf{x}) = \varepsilon_{\mathrm{r}}(\mathbf{x}) - 1 - \mathrm{j}\frac{\sigma(\mathbf{x})}{\omega\varepsilon_0} \tag{2}$$

with ε_{r} the relative permittivity of the object and σ its conductivity.

The input data of CSI-EPT is the scattered B_1^+-field within the domain of interest $\mathbb{D}$, which we denote by $d(\mathbf{x})$. From Maxwell's equations it follows that for this scattered field data we have the representation

$$d(\mathbf{x}) = \frac{1}{2\omega}\partial^+ u^{\mathrm{sc}} = \frac{\omega}{2c_0^2}\partial^+ \int_{\mathbf{x}'\in\mathbb{D}} G(\mathbf{x}-\mathbf{x}')\chi(\mathbf{x}')u(\mathbf{x}')\,\mathrm{d}V \tag{3}$$

for $\mathbf{x} \in \mathbb{D}$, where $\partial^+ = \partial_x + \mathrm{j}\partial_y$. We write the above expression for the data more compactly as

$$d = \mathcal{G}_{\mathrm{d}} w, \tag{4}$$

where $w = \chi u$ is the contrast source and $\mathcal{G}_{\mathrm{d}}$ the data operator given by

$$\mathcal{G}_{\mathrm{d}} w = \frac{\omega}{2c_0^2}\partial^+ \int_{\mathbf{x}'\in\mathbb{D}} G(\mathbf{x}-\mathbf{x}')w(\mathbf{x}')\,\mathrm{d}V \tag{5}$$

with $\mathbf{x} \in \mathbb{D}$. Equation (4) is referred to as the data equation. Finally, using the definition of the scattered field $u^{\mathrm{sc}} = u - u^{\mathrm{inc}}$ in (1), restricting the observation vector to the domain of interest $\mathbb{D}$, and multiplying by the contrast χ, we arrive at the object or state equation

$$w - \chi\mathcal{G}_{\mathrm{o}} w = \chi u^{\mathrm{inc}}, \tag{6}$$

with $\mathbf{x} \in \mathbb{D}$, where we have introduced the object operator as

$$\mathcal{G}_{\mathrm{o}} w = k_0^2 \int_{\mathbf{x}'\in\mathbb{D}} G(\mathbf{x}-\mathbf{x}')w(\mathbf{x}')\,\mathrm{d}V, \quad \mathbf{x} \in \mathbb{D}. \tag{7}$$

With the introduction of the data and object equations and operators, we are in a position to discuss the CSI-EPT reconstruction algorithm.

III. Contrast Source Inversion

Suppose that the body part of interest that occupies the domain $\mathbb{D}$ is illuminated by RF fields due to $N_{\mathrm{ex}} \geq 1$ different coil excitations. For the ith excitation, we then have the data and object equation

$$d_i = \mathcal{G}_{\mathrm{d}} w_i \quad \text{and} \quad w_i - \chi\mathcal{G}_{\mathrm{o}} w_i = \chi u_i^{\mathrm{inc}}, \tag{8}$$

for $i = 1, 2, ..., N_{\mathrm{ex}}$, respectively.

To measure the discrepancy in satisfying the data and object equations for arbitrary contrasts χ and contrast sources w_i, we introduce the data and object residuals as

$$r_{\mathrm{d};i} = d_i - \mathcal{G}_{\mathrm{d}} w_i \quad \text{and} \quad r_{\mathrm{o};i} = \chi u_i^{\mathrm{inc}} - w_i + \chi\mathcal{G}_{\mathrm{o}} w_i, \tag{9}$$

for $i = 1, 2, ..., N_{\mathrm{ex}}$, respectively. We note that since the total field u_i inside the object domain is given by $u_i = u_i^{\mathrm{inc}} + G_{\mathrm{o}} w_i$, the object residual can also be written as

$$r_{\mathrm{o};i} = \chi u_i - w_i, \tag{10}$$

for $i = 1, 2, ..., N_{\mathrm{ex}}$. The magnitude of these residuals is measured using the Euclidean norm $\|\cdot\|$ defined on the reconstruction domain $\mathbb{D}$.

In CSI-EPT, the contrast and contrast sources are updated in an iterative manner. In particular, at the nth iteration we assume that we have an approximate contrast $\chi^{[n-1]}$ and contrast sources $w_i^{[n-1]}$ available and the objective function

$$F^{[n]}(\chi, w) = F^{\mathrm{data}}(w) + F^{\mathrm{object}}(\chi, w|\chi^{[n-1]}) \tag{11}$$

is considered, where

$$F^{\mathrm{data}}(w) = \eta_{\mathrm{d}} \sum_{i=1}^{N_{\mathrm{ex}}} \|r_{\mathrm{d};i}\|^2 \tag{12}$$

with $\eta_{\mathrm{d}} = 1/\sum_{i=1}^{N_{\mathrm{ex}}} \|d_i\|^2$ measures the magnitude of the data mismatch. Note that $F^{\mathrm{data}}(w)$ is shorthand notation for $F^{\mathrm{data}}(w_1, w_2, ..., w_{N_{\mathrm{ex}}})$.

Furthermore, the object objective function is defined as

$$F^{\mathrm{object}}(\chi, w|\chi^{[n-1]}) = \eta_{\mathrm{o}}^{[n-1]} \sum_{i=1}^{N_{\mathrm{ex}}} \|r_{\mathrm{o};i}\|^2 \tag{13}$$

with $\eta_{\mathrm{o}}^{[n-1]} = 1/\sum_{i=1}^{N_{\mathrm{ex}}} \|\chi^{[n-1]} u_i^{\mathrm{inc}}\|^2$ and measures the magnitude of the object equation mismatch.

The contrast and contrast source are now updated in a two step procedure. In particular, at the nth iteration, first the contrast is fixed to the current estimate $\chi = \chi^{[n-1]}$ and the contrast sources are updated using the update formula

$$w_i^{[n]} = w_i^{[n-1]} + \alpha_i^{[n]} p_i^{[n]}, \quad \text{for } i = 1, 2, ..., N_{\mathrm{ex}}, \tag{14}$$

where $p_i^{[n]}$ are the Polak-Ribière update directions. These directions are determined in terms of the gradients of $F^{[n]}(\chi^{[n-1]}, w)$ with respect to w. Explicit expressions for the update coefficients and update directions can be found in [16], for example.

Second, the contrast is updated by minimizing $F^{[n]}(\chi, w^{[n]})$ with respect to χ. Using the alternate expression for $r_{\mathrm{o};i}$ as given by (10), this minimum is easily found as

$$\chi^{[n]} = \frac{\sum_{i=1}^{N_{\mathrm{ex}}} w_i^{[n]} u_i^{[n]*}}{\sum_{i=1}^{N_{\mathrm{ex}}} |u_i^{[n]}|^2}, \tag{15}$$

where $u_i^{[n]} = u_i^{\mathrm{inc}} + \mathcal{G}_{\mathrm{o}} w_i^{[n]}$, $i = 1, 2, ..., N_{\mathrm{ex}}$, and the asterisk denotes complex conjugation. The contrast and contrast source now have both been updated and the CSI-EPT algorithm continues with the next iteration.

A. Contrast Source Inversion with Multiplicative Regularization

In the original regularized CSI method, regularization is included in a multiplicative manner and the objective function

$$F_{\mathrm{MR}}^{[n]}(\chi, w) = F^{[n]}(\chi, w) F_{\mathrm{R}}(\chi|\chi^{[n-1]}), \tag{16}$$

is considered at the nth iteration instead of objective function (11). In the above expression, $F_{\mathrm{R}}(\chi|\chi^{[n-1]})$ is the multiplicative regularization function given by

$$F_{\mathrm{R}}(\chi|\chi^{[n-1]}) = \frac{1}{A}\int_{x\in\mathbb{D}} \frac{|\nabla\chi|^2 + \delta^{[n-1]}}{|\nabla\chi^{[n-1]}|^2 + \delta^{[n-1]}}\,\mathrm{d}V \tag{17}$$

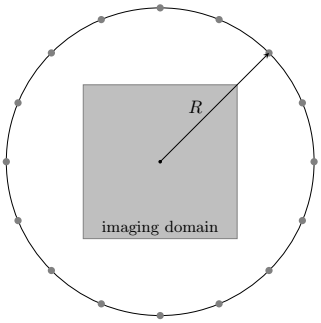

Fig. 1. Sixteen line sources (gray dots) representing the rungs of a birdcage coil. The line sources are equally distributed on a circle with a radius $R = 0.352$ m.

with A the area of the domain $\mathbb{D}$ and

$$\delta^{[n-1]} = (1/\Delta^2) F^{\text{object}}\left(\chi^{[n-1]}, w^{[n]} | \chi^{[n-1]}\right), \tag{18}$$

where Δ is the side length of a pixel used when discretizing the object domain $\mathbb{D}$.

Note that, by construction, $F_{\text{R}}(\chi^{[n-1]}|\chi^{[n-1]}) = 1$ and therefore the presence of F_{R} does not affect the updating procedure for the contrast sources w_i. The update procedure for the contrast does change, however. Explicitly, we update the contrast according to the formula

$$\chi^{[n]} = \chi_{\text{csi}}^{[n]} + \beta^{[n]} q^{[n]}, \tag{19}$$

where $\chi_{\text{csi}}^{[n]}$ is the contrast of (15) and $q^{[n]}$ is the Polak-Ribière update direction expressed in terms of the gradient of $F_{\text{MR}}^{[n]}(\chi, w^{[n]})$ with respect to χ. Explicit expressions for the update direction and the gradient can be found in [17], where it is also shown how to compute the update coefficient $\beta^{[n]}$. The performance of this type of regularization has been extensively demonstrated for CSI and CSI-EPT in [14] and [17], respectively.

IV. One-Step Jacobi Contrast Inversion

At the nth iteration of the improved multiplicative regularization approach followed in this paper, we first update the contrast sources w_i just as in standard CSI or the multiplicative CSI method of the previous section. In other words, updating the contrast sources is the same as in standard (multiplicative) CSI. Having updated these contrast sources, the corresponding total fields $u_i^{[n]}$ are determined and the contrast $\chi_{\text{csi}}^{[n]}$ estimate of (15) is computed. Subsequently, the objective function

$$F_{\text{MR}}^{[n]}(\chi, w^{[n]}) = \left[F^{\text{data}}(w^{[n]}) + \frac{\int_{x\in\mathbb{D}} |\chi - \chi_{\text{csi}}^{[n]}|^2 \, \text{d}V}{\int_{x\in\mathbb{D}} |\chi_{\text{csi}}^{[n]}|^2 \, \text{d}V}\right] F_{\text{R}}(\chi|\chi_{\text{csi}}^{[n]}), \tag{20}$$

is considered with

$$F_{\text{R}}(\chi|\chi_{\text{csi}}^{[n]}) = \frac{1}{A}\int_{x\in\mathbb{D}} \frac{|\nabla\chi|^2 + \delta^{[n]}}{|\nabla\chi_{\text{csi}}^{[n]}|^2 + \delta^{[n]}} \, \text{d}V \tag{21}$$

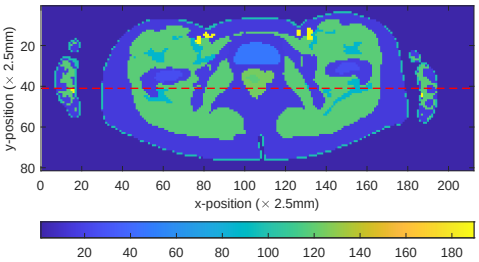

Fig. 2. Magnitude plot of the contrast χ at 128 MHz of a slice through the pelvis region of the Ella model of the ITIS foundation. The dashed line indicates the position of the line profiles shown in Figures 4 and 6.

and

$$\delta^{[n]} = (1/\Delta^2) F^{\text{object}}\left(\chi_{\text{csi}}^{[n]}, w^{[n]} | \chi_{\text{csi}}^{[n]}\right). \tag{22}$$

Finally, the updated contrast is obtained as

$$\chi^{[n]} = \underset{\chi}{\text{argmin}}\, F_{\text{MR}}(\chi, w^{[n]}). \tag{23}$$

Minimization of F_{MR} is carried out by calculating the first variation of this function with respect to $\chi^*(\mathbf{x})$ with $\mathbf{x} \in \mathbb{D}$ (see [16]). We then arrive at the Euler-Lagrange equation that corresponds to this minimization problem. This is a nonlinear equation in χ, but to find a regularized contrast it is sufficient to only consider the linearized Euler-Lagrange equation, which is given by [16]

$$\chi(\mathbf{x}) - \left[F^{\text{data}}(w^{[n]}) M\left(\chi_{\text{csi}}^{[n]}\right)\right] \boldsymbol{\nabla} \cdot \left[b^{[n]} \boldsymbol{\nabla}\chi(\mathbf{x})\right] = \chi_{\text{csi}}^{[n]}(\mathbf{x}) \tag{24}$$

with $\mathbf{x} \in \mathbb{D}$. In the above equation

$$b^{[n]} = \left(\left|\boldsymbol{\nabla}\chi_{\text{csi}}^{[n]}\right|^2 + \delta^{[n]}\right)^{-1} \tag{25}$$

and $M\left(\chi_{\text{csi}}^{[n]}\right)$ is the mean of $\left|\chi_{\text{csi}}^{[n]}\right|^2$ over the domain $\mathbb{D}$ given by

$$M\left(\chi_{\text{csi}}^{[n]}\right) = \frac{1}{A}\int_{\mathbf{x}\in\mathbb{D}} \left|\chi_{\text{csi}}^{[n]}\right|^2 \, \text{d}V \tag{26}$$

with $A = \int_{\mathbf{x}\in\mathbb{D}} \text{d}A$ the area of the domain $\mathbb{D}$.

In practice, equation (24) is discretized on a uniform grid with pixels having a side length Δ and using two-point finite-difference formulas for the gradient and divergence operators. After this discretization procedure (for details, see [16]), we arrive at a system of equations $\mathsf{A}\mathsf{c} = \mathsf{c}_{\text{csi}}^{[n]}$, where c and $\mathsf{c}_{\text{csi}}^{[n]}$ are the discretized and vectorized counterparts of χ and $\chi_{\text{csi}}^{[n]}$, respectively. Moreover, it can be shown that matrix A is diagonally dominant and therefore a new contrast is computed by carrying out a single Jacobi iteration with $\mathsf{c}_{\text{csi}}^{[n]}$ as initial guess. Explicitly, the new contrast is computed from $\mathsf{c}_{\text{csi}}^{[n]}$ as

$$\mathsf{c}^{[n]} = \mathsf{D}^{-1}(\mathsf{I} - \mathsf{R})\mathsf{c}_{\text{csi}}^{[n]}, \tag{27}$$

where D is the diagonal of matrix A and $\mathsf{R} = \mathsf{A} - \mathsf{D}$ the remainder. The new contrast has now been determined and CSI proceeds to the next iteration.

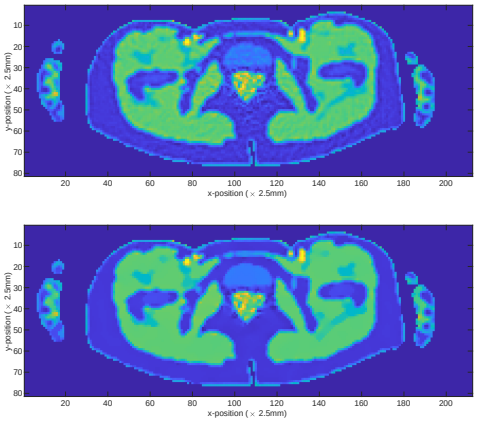

Fig. 3. Magnitude of the reconstructed contrast after 1000 iterations of the standard multiplicative CSI-EPT method (top) and Jacobi multiplicative CSI-EPT method (bottom) for B_1^+- amplitude and phase data with an SNR of 50 dB.

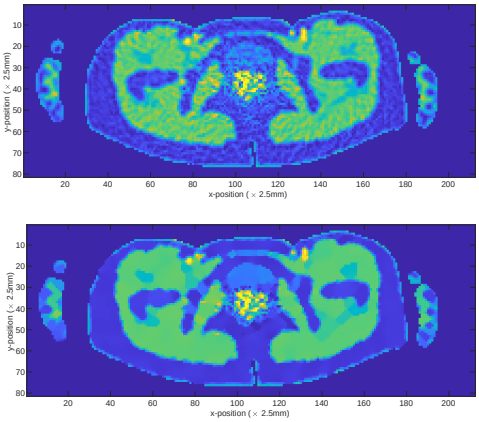

Fig. 5. Magnitude of the reconstructed contrast after 1000 iterations of the standard multiplicative CSI-EPT method (top) and Jacobi multiplicative CSI-EPT method (bottom) for B_1^+- amplitude and phase data with an SNR of 40 dB.

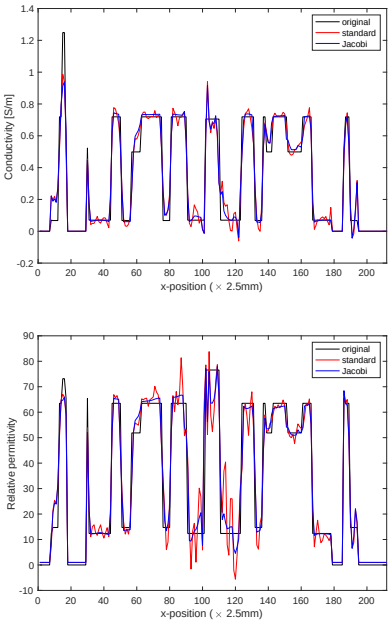

Fig. 4. The conductivity and relative permittivity profiles on the line illustrated in Fig. 2. The exact conductivity and permittivity profiles are shown (black lines) along with the reconstructed profiles for standard CSI-EPT (red line) and Jacobi CSI-EPT (blue line). Reconstructions were obtained for 50 dB noisy B_1^+-data.

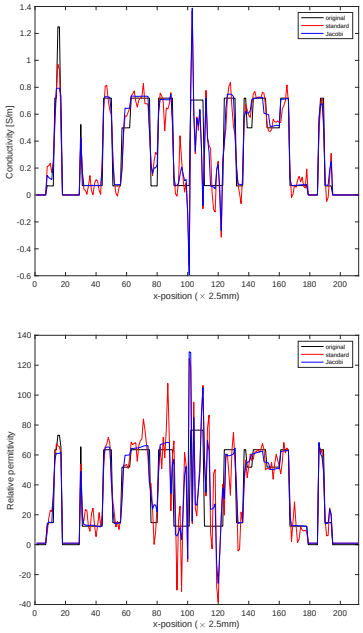

Fig. 6. The conductivity and relative permittivity profiles on the line illustrated in Fig. 2. The exact conductivity and permittivity profiles are shown (black lines) along with the reconstructed profiles for standard CSI-EPT (red line) and Jacobi CSI-EPT (blue line). Reconstructions were obtained for 40 dB noisy B_1^+-data.

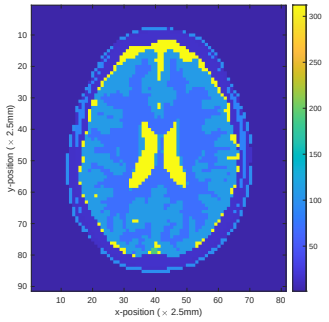

Fig. 7. Magnitude of the contrast tissue model of the head of the Ella body model at 128 MHz.

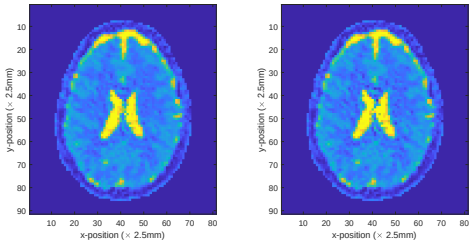

Fig. 8. Magnitude of the reconstructed contrast after 1000 iterations of the standard multiplicative CSI-EPT method (left) and Jacobi multiplicative CSI-EPT method (right) for B_1^+- amplitude and phase data with an SNR of 40 dB.

V. NUMERICAL EXPERIMENTS

We demonstrate the performance of the proposed regularization approach by considering tissue profiles through the pelvis region and head of the Ella body model of the ITIS foundation [18]. The profiles are located within the imaging domain, which is surrounded by 16 line sources representing the rungs of an RF coil,see Fig. 1. The line sources are uniformly distributed on a circle with a radius of 0.352 m. Its center coincides with the center of the imaging domain. The line sources operate at a Larmor frequency of 128 MHz, which corresponds to an MR background field of 3T. The conductivity and permittivity values of the various tissue types within the slice through the pelvis region at 128 MHz are taken from the ITIS database. A magnitude plot of the corresponding contrast profile is shown in Fig. 2. Finally, the same three coil excitations (one quadrature and two linear excitations) as in [15] are used to illuminate the pelvis region of the body.

Subsequently, for the given coil excitations, the B_1^+ field inside the pelvis region is computed and the magnitudes and phases of these fields are contaminated by random Gaussian noise such that the resulting B_1^+ amplitudes and phases have a signal to noise ratio of 40 or 50 dB [19]. These noisy data sets now serve as input for the multiplicative CSI-EPT algorithms. The magnitude of the reconstructed contrast profile after 1000 iterations is shown in Fig. 3 (top) and Fig. 3 (bottom) for the standard and one-step Jacobi multiplicative CSI-EPT method and 50 dB noisy B_1^+-data, respectively. The Structural Similarity Index Measure (SSIM) for the reconstructed magnitude of the contrast is 0.3587 for standard multiplicative CSI-EPT and 0.3742 for the proposed Jacobi variant.

We observe that noise is much better suppressed by Jacobi CSI-EPT than standard CSI-EPT. Also note that for both approaches, the reconstructions in the middle of the profile are the least accurate. This is due to a small electric field that is present around the center of the profile (see also [15]). Furthermore, in Fig. 4 the reconstructed conductivity (top) and permittivity (bottom) profiles on the dashed line of Fig. 2 are shown. Reconstruction results for standard (red line) and one-step Jacobi (blue line) are shown. Clearly, improved reconstructions are obtained with one-step Jacobi CSI-EPT. The large jumps in the conductivity and permittivity profiles are also essentially captured by the CSI-EPT reconstructions.

In Fig. 5 reconstruction results after 1000 iterations of standard (top, SSIM = 0.3172) and Jacobi CSI-EPT (bottom, SSIM = 0.3452) are shown for 40 dB B_1^+-data. Again, noise is much better suppressed by the Jacobi CSI-EPT method and the difference between the original multiplicative approach and the Jacobi approach is even more dramatic. The line profiles of Fig. 6 also illustrate this, where in the top figure the reconstructed conductivity on the dashed line of Fig. 2 is shown, while the reconstructed permittivity is shown in the bottom figure. Also note that since the magnitude of the electric field is small at the center of the slice, the effects due to noise are much more severe at this location for 40 dB data than for 50 dB data. Finally, we mention that the computational complexity of a single iteration of each method is of approximately the same order and one-step Jacobi regularization therefore provides improved reconstructions of noisy data for the pelvis region at approximately the same computational costs. Specifically, for the pelvis region the reconstruction time of standard and Jacobi regularization is approximately four minutes on a standard laptop with a 2 GHz Intel Core i7-8565U CPU, 8 GB RAM, and running Matlab 2022b.

As a last example, we consider the contrast profile of a slice through the head of the Ella body model as illustrated in Fig. 7. Such a profile is also considered in [20] and [21]. The reconstructions obtained for noisy 40 dB B_1^+ data with standard and Jacobi multiplicative regularization are shown in Fig. 8 (left) and Fig. 8 (right), respectively. In this case, magnitude reconstructions using standard and Jacobi regularization take about one minute on the same computer as mentioned above and both reconstructions have an SSIM of about 0.45. Visual inspection of the reconstructions shown in Fig. 8 also confirms that both reconstructions are indeed very similar. In this case, Jacobi regularization provides a reconstruction of a similar quality as standard regularization. Further experiments indicate that for the EPT problem considered here, Jacobi regularization generally provides reconstructions that are of at least the same quality as standard multiplicative regularization.

VI. Conclusions

In this paper, we have presented a multiplicative CSI-EPT method to suppress the effects of noise on CSI-EPT reconstructions. The method considers the contrast source and contrast as fundamental unknowns and updates these quantities in an alternating manner. Specifically, at each iteration, first the contrast is fixed and the contrast source is updated (step 1) and subsequently the contrast source is fixed and the contrast is updated (step 2). In the first step, the contrast source is updated in the same manner as in standard CSI-EPT and this updated contrast source provides us with a least-squares reconstruction of the contrast. The second step, however, is different and filters the least-squares reconstruction of the first step by carrying out a single Jacobi iteration on an equation that follows from approximately minimizing a multiplicative objective function for the contrast. By construction, this objective function suppresses noise in the contrast (tissue) reconstructions.

For noisy 40 dB or 50 dB B_1^+ data, we have illustrated the performance of the one-step Jacobi approach and compared the reconstruction results with reconstructions obtained with standard multiplicative CSI-EPT. A strongly inhomogeneous slice through the pelvis region and the head of a female body model were used for the comparison. Reconstruction results were presented that show that one-step Jacobi generally provides improved noise compression compared with standard CSI-EPT. Furthermore, the action of the discretized integral operators in CSI-EPT can be computed using FFTs, since the spatial grid is uniform. Moreover, differentiation in the regularization operator is implemented using two-point finite differences and consequently the computational costs of a CSI-EPT iteration is dominated by FFTs. For the head and pelvis region it typically takes around 500 (head) to 1000 (pelvis) iterations to match the data to noise level and computation times in Matlab are in the order of minutes on a standard laptop. Finally, no regularization parameters need to be determined (computed) in multiplicative CSI-EPT, but its performance does depend on the noise level, the choice for $\delta^{[n]}$, and how the finite-differences are implemented. Different implementations may also require a different number of CSI-EPT iterations to reach a satisfactory reconstruction.

Nevertheless, given the promising reconstruction results for 2D tissue profiles, we intend to extend Jacobi regularization to 3D CSI-EPT [22]. Moreover, the presence of the RF shield in the background should be taken into account. Finally, we have assumed that the phase of the B_1^+ field is known. In practice, however, this phase is not directly measurable and only approximately known [23]. Using the technique presented in [23], it may be possible to reconstruct the phase during the iteration process and it is our objective to incorporate one-step Jacobi noise suppression in this technique as well.

References

[1] U. Katscher, C. A. T. van den Berg, "Electric properties tomography: biochemical, physical and technical background, evaluation and clinical applications, *NMR Biomed.*," vol. 30, no. 8, pp. 1–15, 2017.

[2] J. Liu, Y. Wang, U. Katscher, B. He, "Electrical Properties Tomography Based on B_1 Maps in MRI: Principles, Applications, and Challenges", *IEEE Trans. Biomed. Eng.*, vol 64, no. 11, pp. 2515-2530, 2017.

[3] J. Chen, Z. Feng, J. M. Jin, "Numerical simulation of SAR and B1-field inhomogeneity of shielded RF coils loaded with the human head," *IEEE Trans. Biomed. Eng.*, vol. 45, no. 5, pp. 650 – 659, 1998.

[4] U. Katscher, T. Voigt, C. Findeklee, P. Vernickel, K. Nehrke, O. Dössel, "Determination of electrical conductivity and local SAR via B1 mapping, *IEEE Trans. Med. Imag.*," vol. 28, no. 9, pp. 1365 – 1374, 2009.

[5] C. M. Collins, W. Liu, J. Wang, R. Gruetter, J. T. Vaughan, K. Ugurbil, M. B. Smith, "Temperature and SAR calculations for a human head within volume and surface coils at 64 and 300 MHz," *J. Magn. Reson. Imaging*, vol. 19 no. 5, pp. 650 – 656, 2004.

[6] E. Balidemaj, C. A. T. van den Berg, A. L. H. M. W. van Lier, A. J. Nederveen, L. J. A. Stalpers, H. Crezee, R. F. Remis, "B1-based SAR reconstruction using contrast source inversion - electric properties tomography (CSI-EPT)," *Med. Biol. Eng. Comput.*, vol. 55, no. 2, pp. 225 – 233, 2017.

[7] L. X. Liu, W. W. Dong, X. M. Ji, L. H. Chen, L. Chen, W. He, J. P. Jia, "A new method of non-invasive brain-edema monitoring in stroke: cerebral electrical impedance measurement," *Neurol Res*, vol. 28, no. 1, pp. 31 – 37, 2006.

[8] R. Leijsen, W. Brink, C. van den Berg, A. Webb, and R. Remis, "Electrical properties tomography: a methodological review," *Diagnostics*, vol. 11, no. 2, pp. 176, 2021.

[9] A. J. G. Inda, S. Y. Huang, N. İmamoğlu, R. Qin, T. Yang, T. Chen, Z. Yuan, and W. Yu, "Physics informed neural networks (PINN) for low snr magnetic resonance electrical properties tomography (MREPT)," *Diagnostics*, vol. 12, no. 11, p. 2627, 2022.

[10] R. Leijsen, C. van den Berg, A. Webb, R. Remis, and S. Mandija, "Combining deep learning and 3D contrast source inversion in MR-based electrical properties tomography ," *NMR Biomed.*," vol. 35, no. 4, pp. e4211, 2022.

[11] P. M. van den Berg and R. E. Kleinman, "A contrast source inversion method," *Inverse Probl.*, vol. 13, no. 6, pp. 1607 – 1620, 1997.

[12] P. M. van den Berg, A. Abubakar, and J. T. Fokkema, "Multiplicative regularization for contrast profile inversion," *Radio Sci.*, vol. 38, no. 2, pp. VIC 23-1 – 23-10, 2003.

[13] A. Abubakar, P. M. van den Berg, and J. J. Mallorqui, "Imaging of biomedical data using a multiplicative reularized contrast source inversion method," *IEEE Trans. Micro. Th. Tech.*, vol. 50, no. 7, pp. 1761 – 1771, 2002.

[14] A. Abubakar, P. M. van den Berg, and T. M. Habashy, "Application of the multiplicative regularized contrast source inversion method on TM- and TE-polarized experimental Fresnel data," *Inverse Probl.*, vol. 21, no. 6, pp. S5 – S13, 2005.

[15] E. Balidemaj, C. A. T. van den Berg, J. Trinks, A. L. H. M. W. van Lier, A. J. Nederveen, L. J. A. Stalpers, H. Crezee, R. F. Remis, "CSI-EPT: A contrast source inversion approach for improved MRI-based electrical properties tomography," *IEEE Trans. Med. Imag.*, vol. 34, no. 9, pp. 1788 – 1796, 2015.

[16] P. M. van den Berg, *Forward and Inverse Scattering Algorithms Based on Contrast Source Integral Equations*, Hoboken, Wiley, 2021.

[17] R. L. Leijsen, W. M. Brink, A. G. Webb, and R. F. Remis, "Effects of Simulated Error Sources on Different 3-D CSI-EPT Strategies," *IEEE Trans. Comput. Imaging.*, vol. 7, no. 9, pp. 713 – 723, 2021.

[18] A. Christ, W. Kainz, E. G. Hahn, K. Honegger, M. Zefferer, E. Neufeld, W. Rascher, R. Janka, W. Bautz, J. Chen, "The virtual family development of surface based anatomical models of two adults and two children for dosimetric simulations," *Phys. Med. Biol.*, vol. 55, no. 2, pp. 23 – 38, 2010.

[19] C. Collins and M. Smith, "Signal-to-noise ratio and absorbed power as functions of main magnetic field strength, and definition of "90°" RF pulse for the head in the birdcage coil," *Magn. Reson. Med.*, vol. 45, no. 4, pp. 684 – 691, 2001.

[20] P. S. Fuchs, S. Mandija, P. R. S. Stijnman, W. M. Brink, C. A. T. van den Berg, and R. F. Remis, "First-order induced current density imaging and electrical properties tomography in MRI," *IEEE Trans. Comput. Imaging.*, vol. 4, no. 4, pp. 624 – 631, 2018.

[21] R. Leijsen, W. Brink, X. An, A. Webb, and R. Remis, "Transverse-EPT: A local first order electrical properties tomography approach not requiring estimation of the incident fields," *Prog. Electromagn. Res. M*, vol. 102, pp. 137 – 148, 2021.

[22] R. Leijsen, W. Brink, C. van den Berg, A. Webb, and R. Remis, "3-D contrast source inversion-electrical properties tomography," *IEEE Trans. Med. Imag.*, vol. 37, no. 9, pp. 2080 – 2089, 2018.

[23] P. R. S. Stijnman, S. Mandija, P. S. Fuchs, C. A. T. van den Berg, and R. F. Remis, "Transceive phase corrected 2D contrast source inversion-electrical properties tomography," *Magn. Reson. Med.*, vol. 85, no. 5, pp. 2856 – 2868, 2021.

C